

**Realization of ion mass and energy selected
hyperthermal ion-beam assisted deposition of
thin, epitaxial nitride films: characterization and
application**

Von der Fakultät für Physik und Geowissenschaften
der Universität Leipzig
genehmigte

DISSERTATION

zur Erlangung des akademischen Grades

Doctor rerum naturalium

Dr. rer. nat.

vorgelegt

von M. Sc. Philipp Schumacher

geboren am 15.08.1989 in Münster (Westf.)

Gutachter: Prof. Dr. Dr. h.c. Bernd Rauschenbach

Prof. Dr. Wolfgang Ensinger

Tag der Verleihung: 20.05.2019

Bibliographische Beschreibung

Schumacher, Philipp

Realization of ion mass and energy selected hyperthermal ion-beam assisted deposition of thin, epitaxial nitride films: characterization and application

Universität Leipzig, Dissertation

122 S., 159 Lit., 56 Abb., 5. Tab., 62 Gl., 4 Anh.

Referat

Um Einschränkungen, die es bei der Verwendung von konventionellen Aufbauten für die Ionenstrahl-gestützte Abscheidung gibt, zu umgehen und Ionenstrahlparameter möglichst genau einstellen zu können, wurde ein Quadrupolmassenfiltersystem in einen experimentellen Aufbau für die Ionenstrahl-gestützte Molekularstrahlepitaxie, bei dem hyperthermische Stickstoffionen verwendet werden, integriert. Diese Arbeit besteht aus zwei Teilen. Im ersten Teil wird das Quadrupolmassenfiltersystem in der Kombination mit zwei verschiedenen Ionenquellen bewertet, indem die Eigenschaften der erzeugten Ionenstrahlen ermittelt werden. Es kann gezeigt werden, dass hyperthermische Ionenstrahlen mit gut definierter und variabler Ionenmasse und Ionenenergie erzeugt werden können. Obwohl Raumladungseffekte und das Auskoppeln der Ionen aus dem RF-Potential des Quadrupols den erreichbaren Ionenstrom begrenzen, sind die Bedingungen für Dünnschichtherstellung mit einem solchen Ionenstrahl in ausreichendem Maße erfüllt. Im zweiten Teil der Arbeit wird der experimentelle Aufbau in Betrieb genommen und wurztitisches, $(11\bar{2}0)$ -orientiertes GaN wird auf Al_2O_3 $(1\bar{1}02)$ abgeschieden. Es kann gezeigt werden, dass nicht nur räumlich voneinander getrennte, epitaktische GaN-Nanokristalle, sondern auch epitaktische und zusammengewachsene GaN-Schichten mit homogener Schichtdicke von bis zu 13 nm gewachsen werden können. Sowohl die Nanokristalle als auch die Dünnschichten können unter N^+ und unter N_2^+ -Bestrahlung in einem kinetischen Energiebereich von $60 \text{ eV} < E_{\text{kin}} < 120 \text{ eV}$ hergestellt werden.

Abstract

In order to overcome limitations of conventional setups in ion-beam assisted deposition and to render the ion beam parameters more precisely definable, a quadrupole mass filter system was integrated into a setup for ion-beam assisted molecular beam epitaxy of nitride thin films, where hyperthermal nitrogen ions are employed. This thesis basically consists of two parts. In the first part the performance of the quadrupole mass filter in combination with two different ion sources is evaluated by determining the properties of the generated ion beams. It can be shown that ion beams with well-defined and variable ion mass and ion kinetic energy in the range of hyperthermal energies can be generated. Although space charge effects and coupling ions out of the RF potential of the quadrupole limit the achievable ion current, the setup is shown to sufficiently fulfill requirements for thin film synthesis. In a second part of this thesis the setup is put into operation and $(11\bar{2}0)$ oriented, wurztitic GaN is deposited on Al_2O_3 $(1\bar{1}02)$. It can be shown that well-separated, epitaxial GaN nanocrystals can be deposited as well as epitaxial, coalesced GaN films with homogeneous film thicknesses of up to 13 nm. Both the deposited nanocrystals and thin films can be deposited under N^+ as well as under N_2^+ irradiation in a range of kinetic energies of $60 \text{ eV} < E_{\text{kin}} < 120 \text{ eV}$.

Table of Contents

1. Introduction.....	1
2. Ion-beam assisted deposition (IBAD).....	5
2.1 Thin film growth without additional ion irradiation.....	6
2.1.1 Nucleation	6
2.1.2 Early stages of film growth.....	9
2.1.3 Modes of growth	11
2.2 Low-energy ion bombardment during film growth	12
2.2.1 The role of the kinetic ion energy	12
2.2.2 Ion-to-atom ratio.....	16
2.2.3 Interaction of molecular ions with surfaces in IBAD.....	18
2.2.4 Limitations of IBAD and consequences	20
3. The quadrupole mass filter system.....	23
3.1 The working principle of a quadrupole mass filter.....	24
3.2 Mass filter setup	26
3.3 Ion mass selection	30
3.4 Ion energy selection	32
3.5 Ion beam characteristics	35
3.5.1 Ion currents.....	36
3.5.2 Ion beam profile	38
3.6 Considerations about space charge	41
3.6.1 Comparison of trapping potential and space charge potential	42
3.6.2 Perveance and beam spread	44
3.7 Summary	46
4. Experimental Methods	49
4.1 System for ion-beam assisted molecular beam epitaxy	49
4.1.1 Ultra-high vacuum (UHV) system.....	49
4.1.2 Effusion cell	51

4.1.3 Constricted glow-discharge plasma source.....	52
4.1.4 Kaufman ion source	53
4.2 Crystalline structure and texture.....	55
4.2.1 X-ray based methods	55
4.2.2 Reflection high-energy electron diffraction (RHEED)	59
4.2.3 Transmission electron microscopy	61
4.3 Chemical composition.....	64
4.4 Surface topography	65
4.5 Model system: GaN growth on sapphire	67
5. Application of energy and mass selected ion-beam assisted deposition.....	71
5.1 Growth of GaN nanocrystals	71
5.1.1 The influence of substrate temperature and Ga flux	72
5.1.2 The role of the kinetic energy	78
5.1.3 Crystal structure of GaN nanocrystals	82
5.1.4 Deposition of GaN using molecular N ions	85
5.1.5 Summary	86
5.2 Growth of GaN thin films	87
5.2.1 Film thickness and deposition rates	87
5.2.2 Characterization of crystal structure by X-ray diffraction	92
5.2.3 Surface topography and microstructure	97
5.2.4 Summary	105
6. Conclusion and Outlook	107
References	111
Appendix	120
Publications of the author	126
Curriculum Vitae of the author	128

1. Introduction

With nanotechnology advancing for decades, nowadays thin solid films with tailored properties are indispensable constituents of a multitude of every-day life and high-technology products. Considerable examples, where functionalized thin films or thin films with specifically designed properties are made use of, are microelectronics, solar cells or optical coatings [Mar10]. In microelectronics, there is a significant and ongoing development towards improving device performance and reducing costs which is closely related to optimizing thin film properties on a nanometer scale. Exploiting ion-solid interactions is a key concept in doing so [Nas96, Col86]. In the semiconductor industry, most industrial facilities contain ion implantation systems. Therefore, semiconductor ion implantation is a world-wide multi-billion dollar activity [Bro04]. Apart from manufacturing microelectronic devices, solar cells and optical coatings, ion-solid interactions are also exploited for shaping the properties of a variety of materials in terms of e.g. mass density, crystal structure, tribological behavior, corrosion-resistance and adhesion [Gon03]. Exposing thin solid films to ion beam irradiation is beneficial in many, very diverse fields in research and industry. One of the many possibilities to exploit ion-solid interactions for tailoring material properties is ion-beam assisted deposition (IBAD) [Smi90]. As with ion implantation or other ion-beam related technologies, the area of application and the purpose of the ion-solid interaction in IBAD differ widely. The field of application and the purpose of the ion-solid interaction impose conditions on the properties of the ion beam, particularly on the kinetic energy. If a high-quality crystal structure characterized by a small lattice defect density is to be obtained, the order of magnitude of the relevant kinetic energies usually is $E_{kin} \sim 1 \text{ eV} \dots 1 \text{ keV}$ [Ma99]. Ion kinetic energies in this order of magnitude are called hyperthermal energies [Lif90]. Depending on the material system and on the applied ion species, a specific interval of hyperthermal kinetic ion energies can be expected, for which diffusion processes on the surface during thin film growth are enhanced, while no significant amount of lattice defects is induced [Koc97]. Correspondingly, it was shown experimentally that applying IBAD within this energy interval (or kinetic energy window) yields better results in terms of crystal tilt distribution and lattice defect density compared to a conventional technique like molecular beam epitaxy (MBE) [Tun00, Sie04].

In order to fully exploit the possibilities of IBAD, it is necessary to understand the details of the ion-solid interaction, the growth process and to find experimental evidence. However, the controllability of the ion beam properties represents a limitation to the process of obtaining appropriate experimental data. Typical ion source devices lack either the precise selectability of the ion mass and the ion energy or cannot be operated for hyperthermal ions. There exists experimental data for example on the influence of the kinetic energy on crystal tilt distributions of thin films grown by IBAD [Ger00a]. Though, if the ion beam is composed of a blend of different ion species or the composition of the ion beam is not even known, it is not

straightforward to correlate the experimental data to the kinetic ion energy exclusively. Nitrogen or oxygen ion beams are frequently composed of ions consisting of single atoms and of the respective diatomic molecule. Upon collision of such molecular projectiles with solid surfaces, dissociation of the ion and a subsequent division of the kinetic energy may occur [Mab85]. The ion mass can therefore be expected to have a significant impact on the growth process, as well. An appropriate ion source would in principle allow for experimental access to quantities like e.g the dissociation energy or the dissociation probability of ions consisting of more than one atom.

Considering the above reasoning, it becomes apparent that ion sources have to fulfill certain conditions, if they are to be employed in gaining experimental data about the influence of ion beam parameters on IBAD growth processes and the quality of the resulting crystal structure. Among those are of most importance the separate selectability of ion mass and ion energy. Simultaneously, the ion source device must be operable in an environment, where the final kinetic ion energy is within hyperthermal energies, and emit a sufficient number of ions for synthesizing thin films in reasonable durations of time. For this thesis, a quadrupole mass filter system was designed, which if combined with an appropriate ion source, is expected to fulfill such requirements. A quadrupole mass filter was chosen, because in contrast to other ion mass filters, it does not rely on the use of apertures, which might impede a large transmitted ion current on a relatively large cross-sectional area. Furthermore, the potential of the quadrupole is expected to trap ions inside the device and counteract space charge repulsion, which may be beneficial particularly for hyperthermal ion beams with high ion currents as they are required here.

Mass selected ion beams with hyperthermal kinetic energies were applied in different contexts. For doping graphene for example, energy and mass selected hyperthermal ion beams were generated using Wien-filters by Cress *et al.* [Cre16] as well as by Willke *et al.* [Wil15]. Kim *et al.* also used a Wien-filter to generate an energy and mass selected hyperthermal ion beam for irradiating silicon and synthesizing carbide and oxide layers with a thickness of a few Å [Kim95]. Further, Deng *et al.* investigated the decomposition of molecules induced by a mass- and energy selected hyperthermal ion beam, where the mass selection was executed by a 90° magnetic mass analyzer [Den07]. An example, where quadrupole mass filters were used in the context of hyperthermal mass selected ion beams, is if heavy molecules from electrosprays are to be brought on surfaces non-destructively [Rau06]. However, in all these examples, thin film deposition was not carried out, as it will be presented in the frame of this thesis. The application of a mass filter relying on magnetic fields may be feasible in this context, too. However, the specific requirements motivate a different approach.

In order to obtain appropriate experimental data for investigating the processes involved in IBAD and the role of crucial parameters of hyperthermal ion beams such

as the ion mass and the ion kinetic energy, a material system has to be chosen as model system. Here, it is beneficial to select a material system, which is already extensively investigated. Consequently, the focus of this work can be put on the instrumentation and the ion-solid interaction, instead of possibly encountering novel material properties. GaN is such a material. Since the first realization of a blue light-emitting diode was reported in 1993 [Nak93], there was a huge activity in research about GaN related materials. As a substrate material $\text{Al}_2\text{O}_3(1\bar{1}02)$ is chosen, here.

This work aims at establishing a precisely controllable thin film deposition, realized by a setup combining different nitrogen ion sources with a custom-built quadrupole mass filter system. This means, that in the frame of this work, this setup is to be characterized with regard to the following issues:

- 1) Is the generation of an energy and mass selected hyperthermal nitrogen ion beam feasible?
- 2) Does this ion beam fulfill requirements for thin film deposition?
- 3) To what extent is the deposition of epitaxial GaN nanocrystals and epitaxial GaN thin films feasible when applying such an ion beam?

The first issue is to include an investigation of ion kinetic energy distributions as well as a comparison of the setup's behavior with the theory of quadrupole mass filtering. As part of the second issue, different requirements for the feasibility of thin film deposition have to be taken into account. Among those are sufficiently high ion beam currents transmitted by the quadrupole and a sufficiently broad ion beam to facilitate laterally homogeneous deposition. The limitations of maximizing the ion current density and the physical reason for this limitation are to be evaluated, too. Finally, as part of the third issue, the setup has to be put into operation, i.e. GaN is to be deposited on $\text{Al}_2\text{O}_3(1\bar{1}02)$ using different ion species and different hyperthermal ion energies. Since the synthesis of well-separated GaN nanocrystals is still of interest [Dau08] and can be understood as the starting point of a thin film growth process, first such nanocrystals are to be deposited. Second coalesced thin films are to be synthesized, in order to demonstrate the feasibility of epitaxial thin GaN film deposition. For both cases, special emphasis is to be put on the epitaxial nature, the yield of the deposited crystalline GaN, the growth mode (i.e. the surface topography and the coverage of the Al_2O_3 substrate) and possible imperfections of the crystal structure.

2. Ion-beam assisted deposition (IBAD)

Ion-beam assisted deposition (IBAD) is a hybrid thin film deposition technique, which combines thermal thin film growth with non-thermal ion irradiation. As illustrated in Fig. 2.1, IBAD in general is characterized by the simultaneous exposure of a surface to different material fluxes, at least one of which is provided by an energetic ion beam. The energy of the ion beam is chosen with respect to the purpose of the ion irradiation and the aim of the IBAD process. In the case that the material flux provided by the ion beam is a component of the compound, which is to be deposited, the IBAD process is called reactive. In non-reactive IBAD processes the typical noble gas ion irradiation is exclusively applied to exploit its influence on specific properties of the synthesized material. There is a broad variety regarding the fields of application for IBAD, as well as regarding the experimental details and the purpose of assisting a deposition process with ion irradiation. Particularly for the synthesis of nitrides, there is a large number of examples for the application of reactive IBAD, among which are the synthesis of superconducting NbN, insulating AlN, semiconducting GaN and ferromagnetic GdN [Kid10, Men15, Rau17, Ger07a]. In these examples the material flux, which is assisted by ion irradiation is provided by pulsed laser deposition, ion-beam sputtering and thermal evaporation, respectively. Comprehensive reviews of IBAD are given by Smidt [Smi90], Hirvonen [Hir91] and González-Elipé [Gon03].

This section is to give some theory about thin film growth in general. Subsequently, two of the parameters, which render IBAD a very versatile method are introduced: the kinetic ion energy and the ion-to-atom ratio. Since part of the aim of this work is applying an ion beam with well-defined ion mass, it is necessary to shortly discuss the interaction of molecular ions with surfaces as opposed to the more commonly considered single atom ions.

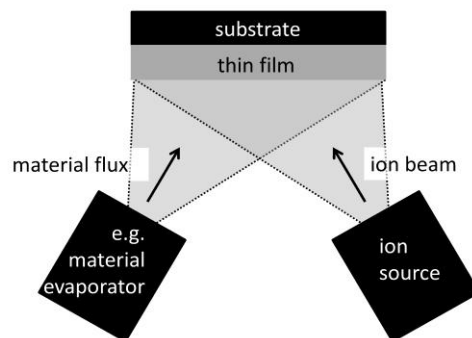


FIG. 2.1: General principle of IBAD: There are at least two material fluxes simultaneously playing a role in thin film growth, among which is at least one energetic ion beam. For a neutral material flux as sketched here, different experimental realizations are available. In several cases the material flux is provided by thermal evaporation. In this case the kinetic energy of the arriving particles is thermal and significantly smaller than the kinetic energy of the ions.

Further, the drawbacks of typical IBAD setups are specified.

2.1 Thin film growth without additional ion irradiation

The formation of thin films can be considered in different stages. The first stage is characterized by the formation of small nuclei, which are statistically distributed over the substrate surface (see subsection 2.1.1). Thereafter, the size of these nuclei increases. Consequently, islands that form from the initial nuclei coalesce and eventually a continuous and very thin film is formed (see subsection 2.1.2). In the last stage, a thicker film is formed (see subsection 2.1.3). Extensive overviews about thin film formation are known [Fre03, Ven03, Mar03].

2.1.1 Nucleation

In the simple case of homogeneous nucleation, a substrate surface of temperature T_s is assumed in a vapor with a pressure p and a temperature T_v . In order to assess homogeneous nucleation, a solid nucleus is assumed to form in the vapor phase. The nucleus as an isotropic solid contains n atoms and has the surface $A(n)$. The change in the Gibbs free energy by forming such a nucleus can be expressed as

$$\Delta G(T_v, p) = -n \cdot \Delta\mu + A(n)\gamma_{nv}, \quad (2.1)$$

where $\Delta\mu$ is the change of the chemical potential when an atom is transferred from the vapor phase to the solid phase and γ_{nv} the interface energy of the solid nucleus and the vapor phase. The surface of the nucleus depends on its shape. Defining a shape factor β , the surface of the nucleus can be formulated as

$$A(n) = \beta n^{2/3}. \quad (2.2)$$

The nucleus can e.g. be assumed to develop a cubic shape. If the edge length of such a cube is a and the atomic volume is Ω_A , the volume of the nucleus is $V = n\Omega_A = a^3$ and the surface of the nucleus $A = 6a^2$. This way the shape factor for a cubic nucleus can be deduced as $\beta_{cubic} = 6\Omega_A^{2/3}$. Correspondingly, the shape factor can be determined for a spherical nucleus with the radius r as $\beta_{sphere} = (36\pi)^{1/3}\Omega_A^{2/3}$. By setting $d(\Delta G)/dn = 0$, an expression for the critical size of the nucleus can be obtained from eq. (2.1)

$$n^* = \left(\frac{2\beta\gamma_{nv}}{3\Delta\mu} \right)^3. \quad (2.3)$$

If the nucleus contains more atoms than n^* , the Gibbs free energy is reduced by attaching additional atoms. Therefore the growth of the nucleus is energetically favored. However, an aggregate consisting of a number of atoms smaller than n^* tends to disappear, because in this case the Gibbs free energy is reduced by detaching atoms.

This implies that the energy barrier ΔG^* has to be overcome for the aggregate to survive and to grow. In order to illustrate these considerations, for simplification a spherical nucleus is assumed in the following. The critical radius r^* , above which the growth of the nucleus is energetically favorable, consequently is

$$r^* = \frac{2\gamma_{nv}\Omega_A}{\Delta\mu}, \quad (2.4)$$

and the difference of the Gibbs free energy by forming a spherical nucleus with the radius r^* is

$$\Delta G^* = \frac{16\pi\gamma_{nv}^3\Omega_A^2}{3(\Delta\mu)^2}. \quad (2.5)$$

For the case of a spherical nucleus, Fig. 2.2 (a) depicts the Gibbs free energy as a function of the sphere radius r . Since a volume and a surface term contribute to the Gibbs free energy with opposite sign, a maximum evolves. This maximum marks the energy barrier ΔG^* for the growth of nuclei and the critical radius r^* , above which the nuclei are stable.

It can be concluded that in homogeneous nucleation the energy barrier ΔG^* is to be overcome in order to promote growth of aggregates and enable the transition from such aggregates to crystallites. According to eq. (2.5), ΔG^* can more easily be overcome, if the chemical potential $\Delta\mu$ is large or the interface energy γ_{nv} small.

In reality, nucleation mostly involves more than one homogeneous material system. Typically, nucleation takes place on surfaces, which consist of a second material and have specific properties that play a very important role in supporting nucleation. In the following, a few aspects regarding such heterogeneous nucleation processes are given. In this context, for simplicity a flat substrate and a seed with the shape of a spherical cap defined by the radius r_{cap} and the contact angle θ are assumed (as shown in Fig. 2.2 (b)). The volume V_n , the surface A_{nv} of the cap and the interface A_{ns} of the cap and the flat substrate can be expressed in terms of r_{cap} and θ in the following way

$$\begin{aligned} V_n &= \frac{\pi r_{cap}^3}{3} [2 + \cos(\theta)][1 - \cos(\theta)]^2 \\ A_{nv} &= 2\pi r_{cap}^2 [1 - \cos(\theta)] \\ A_{ns} &= \pi r_{cap}^2 [1 - \cos^2(\theta)] \end{aligned} \quad (2.6)$$

Apart from the interface of the nucleus and the vapor possessing the interface energy γ_{nv} , there are two further interface energies to be taken into account. Those are the energy of the interface of the substrate and the vapor γ_{sv} as well as the energy of the interface of the nucleus and the substrate γ_{ns} .

2.1 Thin film growth without additional ion irradiation

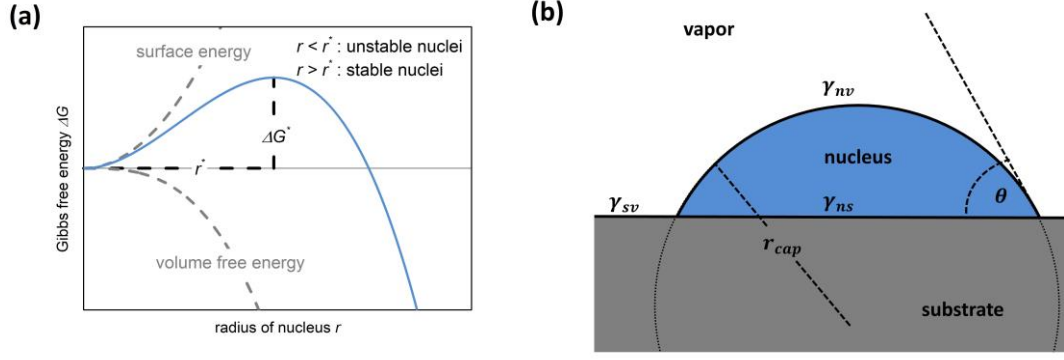


FIG. 2.2: (a) The Gibbs free energy change associated with the formation of nuclei assuming homogenous nucleation. The maximum of this graph reveals the critical size and the energy barrier for the existence of stable nuclei (b) A schematic representation of a spherical, cap-shaped seed on a surface, where γ is an interface energy and the subscripts s, n and v symbolize the substrate, the nucleus and the vapor phase, respectively.

In a similar way as it was done previously, the Gibbs free energy difference for heterogeneous nucleation can be expressed in dependence of the above mentioned quantities

$$\Delta G(r_{cap}) = -\frac{V_n}{\Omega_A} \Delta\mu + A_{nv}\gamma_{nv} + A_{ns}(\gamma_{ns} - \gamma_{sv}) \quad (2.7)$$

The first term is negative, representing the reduction of free energy due to the incorporation of atoms in the nucleus. The remaining terms are added in order to take into account the contribution of the interface energies to the free energy. Again, by deriving the Gibbs free energy and setting $\frac{d(\Delta G(r))}{dr} = 0$, the critical size of the nuclei can be deduced to

$$r_{het}^* = \frac{2\gamma_{nv}\Omega_A}{\Delta\mu} = r^* \quad (2.8)$$

This is the same value, which was also obtained for the homogeneous nucleation (see eq. (2.4)). The size of the nuclei, above which stable nuclei exist, does not depend on whether the nucleation is assumed to be homogeneous or heterogeneous. By combining eq. (2.7) and eq. (2.8), an expression for the energy barrier for heterogeneous nucleation can be found

$$\Delta G_{het}^* = \frac{16\pi\gamma_{nv}^3\Omega_A^2}{3(\Delta\mu)^2} \frac{(2+\cos(\theta))(1-\cos(\theta))^2}{4} \quad (2.9)$$

By comparing eq. (2.9) and eq. (2.5) it is found that the energy barrier for the growth of nuclei differs in homogeneous and in heterogeneous nucleation only by a factor of

$$\frac{\Delta G_{het}^*}{\Delta G^*} = f(\theta) = \frac{(2+\cos(\theta))(1-\cos(\theta))^2}{4}. \quad (2.10)$$

Two limiting scenarios can be regarded here:

- 1) If $\cos(\theta) = -1$, i.e. $\theta = 180^\circ$, the nuclei are spherical and touch the substrate in only one point. The interaction between the substrate and the nucleus vanishes. Since $f(\theta = 180^\circ) = 1$, in this scenario the energy barrier is $\Delta G_{het}^* = \Delta G^*$. Essentially, this limiting scenario corresponds to the case of homogeneous nucleation.
- 2) If $\cos(\theta) = 1$, i.e. $\theta = 0$, the substrate is completely wetted by the nucleus. The factor between the energy barriers in the case of homogeneous and heterogeneous nucleation becomes $f(\theta = 0) = 0$. Consequently, the energy barrier for the growth of nuclei is $\Delta G_{het}^* = 0$.

Most nucleation processes are realized with contact angles between $0^\circ < \theta < 180^\circ$, suggesting, that $0 < \Delta G_{het}^* < \Delta G^*$. Concluding, it is noted that the interaction of a surface with an agglomerate of atoms mostly reduces the energy barriers for the growth of such.

2.1.2 Early stages of film growth

For investigating and understanding the kinetics of thin film growth phenomenologically, rate equations for example formulated and elaborated by Venables [Ven73, Ven03] are frequently regarded. The processes that contribute to the monolayer growth, and that are included in the three following rate equations are illustrated by Fig. 2.3. In the beginning, the temporal change of the number of adatoms or monomers on the surface n_1 is expressed as follows:

$$\frac{dn_1}{dt} = R(1 - Z) - n_1 \left[\frac{1}{\tau_{des}} + D(\sigma_x n_x + 2\sigma_1 n_1) \right]. \quad (2.11)$$

The first term refers to the increase of surface adatoms due to the incoming rate R of atoms from the vapor. If the substrate already possesses a coverage Z , a certain fraction of the incoming particle flux does not contribute to an increase of the number of adatoms, because it arrives on an already existing cluster of atoms. Thus, it does not take part in the growth of the first monolayer, which is accounted for by the second term. The third term considers desorption from the surface. τ_{des} represents the mean time for this desorption to take place. For thin film growth, the formation of clusters is necessary. If adatoms show diffusional behavior on the surface, which is characterized by the diffusion coefficient D , two surface adatoms may collide and form a stable cluster with a probability that depends on the cross-section for such a process σ_1 . Surface adatoms can also collide with an already existing stable cluster, of which there is a number n_x on the surface. For this process, there is a cross-section σ_x . Both the formation of clusters and the growth of clusters due to collision of adatoms with existing clusters, reduce the number of surface adatoms. These effects are also included in this equation by adding the last two terms. For eq. (2.11) it is assumed that clusters consisting of two or more adatoms are already stable and do not decay.

2.1 Thin film growth without additional ion irradiation

The change of the number of stable clusters on the surface is given by a similar rate equation:

$$\frac{dn_x}{dt} = D\sigma_1 n_1^2 - n_x \frac{dZ}{dt}. \quad (2.12)$$

Here two processes play a role: First, the number of clusters increases by collisions of two adatoms as mentioned before. Second, the number of clusters is assumed to decrease only, if coalescence occurs and thereby larger uniform areas of one-monolayer coverage are formed.

A third differential equation to describe the monolayer growth process characterizes the temporal evolution of the coverage. For the 2-dimensional growth of a monolayer this can be expressed as

$$\frac{dZ}{dt} = \Omega_A^{3/2} D\sigma_x n_1 n_x, \quad (2.13)$$

with Ω_A being the atomic volume again. Here, the coverage is assumed to grow by attachment of adatoms to existing stable clusters.

Considering that in the beginning of the monolayer growth process n_1 , n_x , Z and $\frac{dZ}{dt}$ are small, n_1 is expected to grow relatively fast (see eq. (2.11)). For infinite times, however, the coverage can be expected to be unity, i.e. the adatom density n_1 vanishes. Therefore, during the monolayer growth process, n_1 assumes a maximum value. Based on the above rate equations this maximum number of adatoms can be approximated as [Nie89]

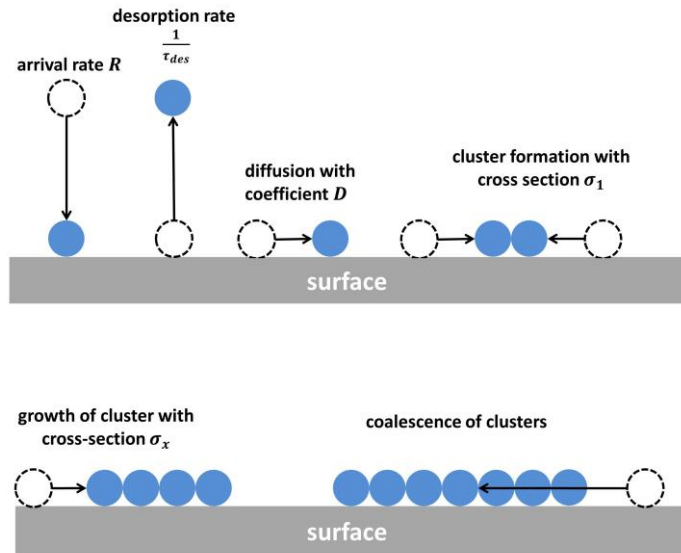


FIG. 2.3: Processes on the surface contributing to the growth of a monolayer as formulated in the rate equations by [Nie89].

$$n_{1,max} = \frac{\sqrt{1+8\sigma_1 DR\tau_{des}}-1}{4\sigma_1 D\tau_{des}}. \quad (2.14)$$

With the increase of n_1 , the number of stable clusters is expected to grow simultaneously (see eq. (2.12)). After the number of both adatoms and stable clusters has increased, the increase of the coverage becomes larger (see eq. (2.14)) and consequently after a certain time coalescence sets in. Thus, the number of both single adatoms and stable clusters starts to decrease at some point, so that in the end, the coverage will reach unity.

2.1.3 Modes of growth

The contact angle of a spherically assumed agglomeration of atoms in heterogeneous nucleation as it was introduced in subsection 2.1.1, has a significant impact on the thin film growth process, in general. Depending on what contact angle of the nucleus minimizes the Gibbs free energy, different growth modes might occur. The growth process of epitaxial thin films in different modes is distinguished by the coalescence behavior. Therefore, thin film properties like the surface topography and the structure of lattice defects significantly depend on the nucleus formation.

The free energy associated with the nucleus formation in dependence of the mentioned surface and interface energies is given by eq. (2.7). Regarding the Gibbs free energy two different cases can be distinguished as shown e.g. in [Fre03]:

- 1) If $\gamma_{sv} > \gamma_{nv} + \gamma_{ns}$, there is no activation barrier for the growth of nuclei and in general the minimum of the free energy is obtained for $\theta = 0$. In this case, the surface of the substrate is completely wetted and the film grows 2-dimensionally. This growth mode is called Frank-van der Merwe mode.
- 2) If $\gamma_{sv} < \gamma_{nv} + \gamma_{ns}$, an activation barrier for the growth of the nucleus might exist and depending e.g. on the exact interface energies and on the chemical potential, there might be a non-zero angle θ , which minimizes the free energy difference. In this case the growth takes places 3-dimensionally and the growth mode is called the Volmer-Weber mode.

Under certain circumstances a third growth may occur. This mode is called Stranski-Krastanov mode and is characterized by an initial 2-dimensional growth and a consequent (after the coverage of the substrate and a critical film thickness) 3-dimensional growth. It should also be mentioned, that this simple, thermodynamical consideration does not take into account effects that are related to the crystal lattice of the growing thin film such as the influence of lattice strain and its relief or the formation and influence of step structures.

2.2 Low-energy ion bombardment during film growth

Thin films deposited at low temperatures without additional ion irradiation show the tendency to grow with a columnar and underdense morphology [Mue86]. The low-energy ion irradiation during the film deposition is supposed to increase the film density and modify growth characteristics from columnar to 2-dimensional while maintaining the epitaxy. In the deposition processes carried out by IBAD, where typically one ion source and one evaporation source are aimed at a substrate (see Fig. 2.1), the two most important parameters are the kinetic ion energy and the ion-to-atom ratio. In the following subsections, these two parameters are discussed. After that, some specifics about the interaction of molecular ions with solid surfaces are given and finally the limitations of conventional IBAD systems are explained.

2.2.1 The role of the kinetic ion energy

The additional energy, which is brought to the surface in the form of the kinetic energy of ions, distinguishes IBAD from conventional thin film deposition techniques like molecular beam epitaxy and has a significant influence on specific properties of the growing thin films, particularly on the crystalline quality [Tun00, Sie04]. Thereby, processes on the surface of the growing thin film, which are different from those discussed before, are exploited. Such additional processes, which are considered in this and the following subsection, are summed up in Fig. 2.4. This subsection is to focus on the influence of the kinetic energy and discuss requirements for this quantity in a context, where crystalline quality plays an important role. The model elaborated by Brice *et al.* [Bri89] enables a prediction of a window of kinetic energies, in which the deposition has to be performed, if the crystalline quality is to be improved by the ion irradiation. Moreover, typical penetration depths and stopping powers for such an energy window are shown.

Brice *et al.* established an analytical way to estimate the number of atomic displacements induced by hyperthermal ion irradiation. Here, the energy deposited into atomic displacements per ion in the surface and in the bulk material is calculated by employing an expression derived by Ma *et al.* [Ma98, Ma99], who used the same approach as Brice *et al.* A few considerations have to be done, before exemplary results for the irradiation of GaN with N⁺ ions can be presented. Here, collisions between N ions and Ga atoms are regarded. The maximum transferable energy during an elastic collision is

$$\Delta E = \frac{4m_1m_2}{(m_1+m_2)^2} E_{kin} = \gamma E_{kin}, \quad (2.15)$$

where E_{kin} is the kinetic energy of the incident ion, m_1 and m_2 are the masses of the incident ion and the atom in the irradiated material, respectively.

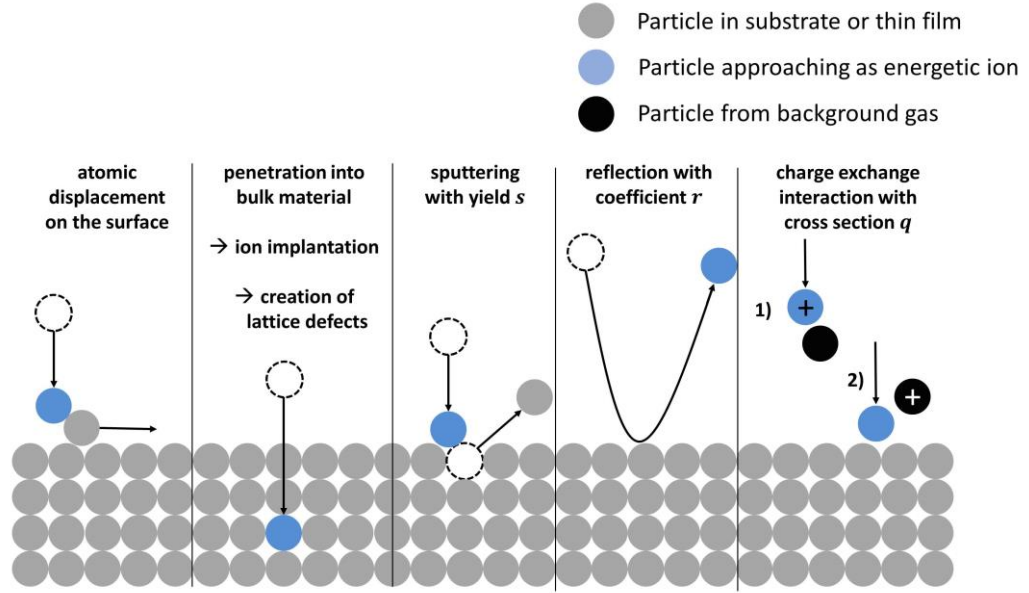


FIG. 2.4: Illustration of processes involving energetic ions in ion-beam assisted thin film growth.

For this example, an energy transfer factor $\gamma = 0.56$ is obtained. The Brice model further assumes a fixed average threshold displacement energy E_d , below which no atoms in the irradiated material can be displaced. The energy needed to displace atoms in crystalline material can be determined by molecular dynamics simulations and depends on the direction, in which the atom is displaced and, therefore, on the type of lattice defect that is created in the interaction with the incident ion [Xia09]. For the results shown in the following, a threshold displacement energy for Ga atoms in bulk GaN crystals $E_{d,bulk} = 22$ eV as determined by Nord *et al.* [Nor03], was assumed. Additionally, the threshold energy for displacements on the surface $E_{d,surface}$ is required to describe the influence of the kinetic energy on structural properties. Such a threshold energy can be calculated by the following empirical formula [Eck03]:

$$E_{d,surface} = \frac{E_s}{\gamma} \left[\left(0.3198 \frac{m_1}{m_2} \right)^{-0.5279} + 1 \right]. \quad (2.16)$$

E_s is the surface binding energy. It is common to calculate the surface binding energy of binary compound targets with a stoichiometry of 1:1 as the average value of the heat of sublimation ΔH_s of the constituents [Eck85]. Therefore

$$E_s = \frac{1}{2} [\Delta H_s(Ga) + \Delta H_s(N)] = \frac{1}{2} [2.82 \text{ eV} + 4.90 \text{ eV}] = 3.86 \text{ eV}, \quad (2.17)$$

where the heats of sublimation for Ga and for N were taken from the reference [Kud05]. The obtained value for E_s is close to an experimentally determined value for the activation energy for desorption of Ga adatoms on GaN surfaces (2.8 eV) [Hey00]. As a result, the threshold energy for displacements on the surface is determined as $E_{d,surface} = 12.35$ eV. Consequently, by using a value of 0.25 nm as the thickness of a GaN monolayer (ML) and a density of Ga atoms in GaN of $N_{Ga} = 4.41 \cdot 10^{28} \text{ m}^{-3}$,

the data plotted in Fig. 2.5 can be obtained. Three different regions of kinetic ion energy evolve in this diagram:

- I) $E_{kin} < E_{d,surface}/\gamma$: In this region, the kinetic energy of the incident ions is not sufficient to cause displacements of atoms on the surface (i.e. in the first ML). Consequently, the ion energy does not have any significant effect on the growth process.
- II) $E_{d,surface}/\gamma < E_{kin} < E_{d,bulk}/\gamma$: Here, the ions have sufficient kinetic energy to displace atoms on the surface. For inducing displacements in the bulk, however, the kinetic ion energy is too small. Regarding high-quality crystal growth, this is the region, in which the deposition process is ideally performed, because the ion irradiation ballistically enhances the diffusion of atoms on the surface. This way, the atoms can find and occupy energetically favorable positions more easily and the number of lattice defects is decreased in comparison to the previously described region. In this context it is important, that displacements in the bulk material below the surface cannot take place, so that additional creation of buried point defects is avoided. For the chosen example the Brice model predicts this region of ideal growth for kinetic energies of $20 \text{ eV} < E_{kin} < 40 \text{ eV}$.
- III) $E_{kin} > E_{d,bulk}/\gamma$. If the kinetic energy of the incident ions is larger than the threshold for atomic displacements in the bulk material, the ions penetrate into the material more deeply. Here, damage is caused to the crystal lattice below the first ML.

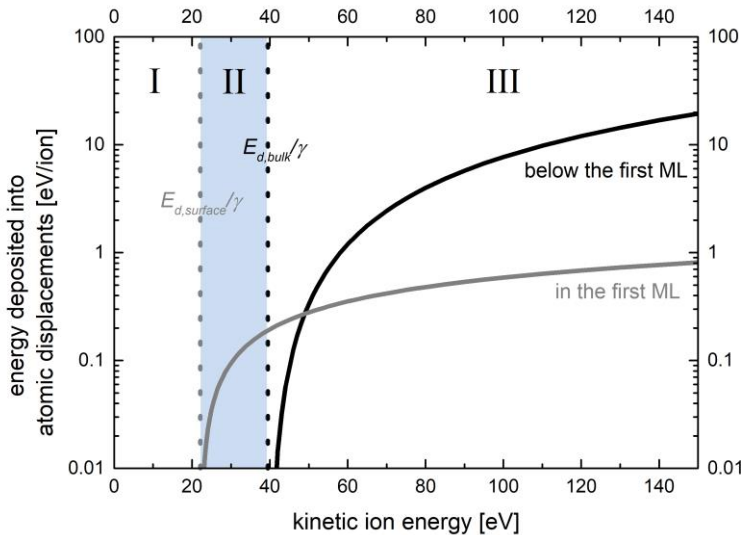


FIG. 2.5: The energy deposited into atomic displacements in dependence of the kinetic energy of the incident ions. The data shown was calculated according to the Brice model for the irradiation of GaN with N^+ ions. The grey curve refers to atomic displacements in the first ML, while the black curve refers to atomic displacements below the first ML. The dotted lines indicate the position of the threshold energies for the atomic displacements on the surface and in the bulk.

Fig. 2.5 only regards the displacements of Ga atoms in GaN by collisions with N^+ ions. For collisions of N atoms and N^+ ions, however, $\gamma = 1$. Thus, the window of ion energies for ideal growth conditions would be shifted to lower energies (assuming the threshold energies $E_{d,bulk}$ and $E_{d,surface}$ are not significantly changed). The critical assumption in the Brice model is related to the threshold displacement energies, because the literature disagrees on these values (25 eV ... 39 eV for N displacement in bulk GaN) [Xia09, Nor03]. Further, determining the value of the threshold displacement energy on the surface includes empirical calculations, which require the heat of sublimation, for which values in literature also differ. Moreover, the Brice model does not take into account the influence of the temperature on the diffusional behavior of atoms on the surface. The Brice model can, therefore, be used to obtain only approximate values for the lower and the upper limit of the ion kinetic energy in deposition processes, where high-quality crystalline growth is yielded. If reliable information about the optimum range of ion kinetic energies is required, experimental verification is inevitable.

The penetration depth of ions in materials depends on the properties of both the ion and the irradiated material. For hyperthermal ions, the penetration depth, typically, is in the range of a few ML. Fig. 2.6 (a) plots the penetration depth for the example of GaN irradiation with N^+ ions as calculated by the software SRIM [Zie85]. This software makes use of the Ziegler-Biersack-Littmark potential as interatomic potential. It is to be noted that this potential is not a suitable description of the interatomic potential for low energies as they are regarded here. In this low-energy regime, typically the ion-atom distance r during an ion-atom collision can obtain values $a_0 < r < r_0$, with a_0 being the Bohr radius and r_0 being the atom-atom distance in a crystal [Nas96].

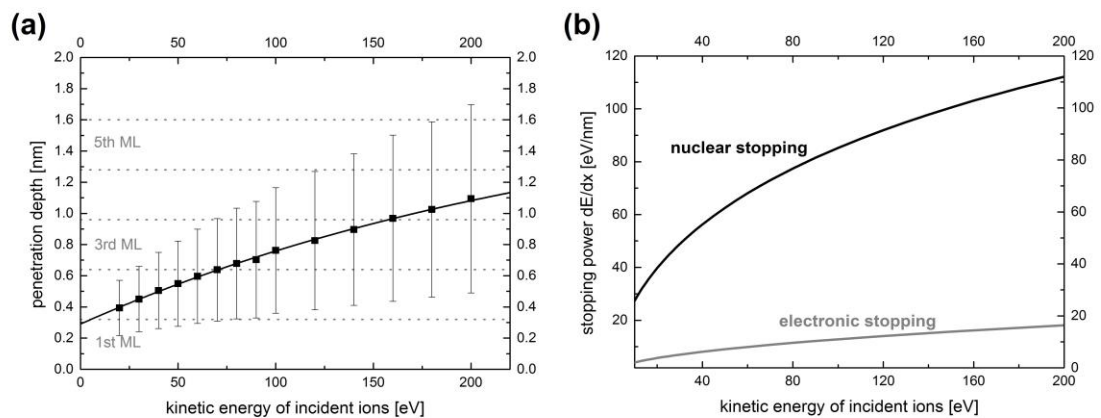


FIG. 2.6: Data obtained for the irradiation of GaN with hyperthermal N^+ ions using the computer code SRIM (a) the penetration depth in dependence of the kinetic energy of the incident ions. The error bars correspond to twice the standard deviation of the penetration depth, i.e. 68 % of the ions can be assumed to stop within the limits of this error. And (b) the stopping power in dependence of the kinetic energy of the incident ions. The two curves represent the two different mechanisms for the deceleration of the ions: nuclear stopping and electronic stopping.

In this case, it would be reasonable to apply a simple two-parameter Born-Mayer potential of the form $U(r) = Ae^{-Br}$ [Abr69]. Using such a potential however one relies on the appropriate choice for the constants A and B . Consequently, here the results of SRIM using the ZBL potential are assumed as estimation: If the N^+ ions possess a low, hyperthermal energy like $E_{kin} = 20$ eV, the majority of the ions stop within the first two MLs, while for higher energies like $E_{kin} = 100$ eV, a significant fraction of the ions stops within the 4th ML. There are two different kinds of energy loss, which lead to the deceleration of ions in a material. Those are nuclear stopping, where elastic collisions between ions and atoms in the irradiated material take place, and electronic stopping, where inelastic collisions with bound electrons in the material occur. As shown in Fig. 2.6 (b) for N^+ irradiation of GaN in the range of hyperthermal ion energies, typically, the nuclear stopping dominates. In this case, the nuclear stopping power is 6 – 7 times larger than the electronic stopping power.

2.2.2 Ion-to-atom ratio

IBAD is a highly flexible technique, because the different material fluxes can be controlled independently from each other. Consequently, the ratio of the flux of N ions ϕ_N^+ and the flux of Ga atoms ϕ_{Ga} (both in sample position) is an important parameter and has considerable impact on the properties of the produced thin films. This impact is not restricted to the stoichiometry, its nature can be much more complex. It was for example shown, that the ion-to-atom ratio $R_{I/A} = \phi_N^+ / \phi_{Ga}$ influences the crystalline orientation and quality of GaN thin films [Ger07].

As illustrated in Fig. 2.4, there are several processes taking place at the surface during thin film growth in IBAD. Due to these processes, it is necessary to distinguish the emitted, initial N ion flux ϕ_N^+ and Ga atom flux ϕ_{Ga} from the number of N and Ga atoms ϕ_N^f and ϕ_{Ga}^f that are incorporated in the growing thin film per time interval and area. Van Vechten *et al.* [Vec90] derived an expression for the final ratio of the number of N atoms and vapor atoms in the produced thin film $R_f = \phi_N^f / \phi_{Ga}^f$.

Starting with the current density of the N ion beam j , emitted by the ion source, the flux of nitrogen atoms can be calculated

$$\phi_N = \frac{j}{e} \sum_i n_i \epsilon_i, \quad (2.18)$$

where n_i is the fraction of a certain ion species in the initial ion beam (e.g. N^{2+} or N_2^+) and ϵ_i is the number of nitrogen atoms in an ion per elementary charge (e.g. $\epsilon = 0.5$ for N^{2+} and $\epsilon = 2$ for N_2^+). For a precise expression of the number of N atoms available for the GaN thin film, it is also important to take into account charge exchange interactions. In collisions between ions and gas particles, the energetic ions are neutralized by electron exchange. In such interactions, energetic and neutral

nitrogen particles, which are directed to the surface and charged gas particles with low, thermal energy, emerge. This means that, comparably to the Lambert-Beer law [Atk14], the ion current density decreases exponentially with increasing distance from the ion source. The number of nitrogen atoms that are available for the thin film growth, however, does not decrease. Therefore, the ion current density in the position of the sample (in a distance d from the ion source) j_{FC} , which could be measured e.g. by a Faraday cup, has to be distinguished from the ion current density j emitted by the ion source.

$$n_i j = j_{FC,i} e^{q_i p d / k_B T} = j_{FC,i} (1 + \beta_i), \quad (2.19)$$

where q_i is the cross-section for the charge exchange interactions of the ion species i , p and T are the pressure and the temperature of the gas, respectively, and $j_{FC,i}$ is the contribution of ion species i to the ion current density $j_{FC} = \sum_i j_{FC,i}$. The factor $(1 + \beta_i)$ is defined in eq. (2.19) to simplify this expression. Consequently, eq. (2.18) can be rewritten as

$$\phi_N = \frac{1}{e} \sum_i j_{FC,i} \epsilon_i (1 + \beta_i). \quad (2.20)$$

Reflection of energetic N atoms or N ions is an additional aspect, which has to be taken into account, to finally obtain

$$\phi_N^f = \frac{1}{e} \sum_i j_{FC,i} \epsilon_i (1 + \beta_i) (1 - r_i), \quad (2.21)$$

where r_i is the fraction of reflected particles of the species i . Subsequently, ϕ_{Ga}^f can be written as

$$\phi_{Ga}^f = \phi_{Ga} - \frac{1}{e} \sum_i j_{FC,i} \epsilon_i (1 + \beta_i) s_i. \quad (2.22)$$

Here, a term is subtracted from ϕ_{Ga} , in order to account for Ga atoms that are not incorporated in the growing film due to sputtering. s_i , therefore, is the sputtering yield of Ga for the N species i . The two expressions for ϕ_{Ga}^f and ϕ_N^f can be rewritten and simplified under the assumption, that β_i is independent of the ion species ($\beta_i = \beta$), which implies, that the fractions n_i remain constant between the ion source and the substrate surface. Additionally, the parameter $\delta = \sum_i n_i \epsilon_i$ is defined. Therefore

$$\phi_N^f = \frac{j_{FC}}{e} \delta (1 + \beta) (1 - \bar{r}), \quad (2.23)$$

and

$$\phi_{Ga}^f = \phi_{Ga} - \frac{j_{FC}}{e} \delta (1 + \beta) \bar{s}. \quad (2.24)$$

\bar{r} and \bar{s} are weighted average values of the fractions of reflected ions and of sputtering yields, respectively, according to

$$\bar{x} = \frac{\sum_i n_i \epsilon_i x_i}{\delta}. \quad (2.25)$$

In the following, the ratio of the initial material fluxes will be called $R = \phi_N / \phi_{Ga}$. In the end, the two derived final material fluxes can be divided by each other to obtain the ratio of the remaining N and Ga atoms in the thin film:

$$R_f = \frac{\phi_N^f}{\phi_{Ga}^f} = \frac{R(1-\bar{r})}{1-R\bar{s}}. \quad (2.26)$$

Note, that $R \neq R_{I/A}$. The so-called ion-to-atom ratio as it is defined in the beginning of the subsection is referring only to the number of ions and does neither take into account mass or charge of the ions nor the composition of the ion beam. Using the parameters as introduced in this subsection, the ion-to-atom ratio is $R_{I/A} = \frac{j_{FC}/e}{\phi_{Ga}}$. Therefore, a relation between the ion-to-atom ratio and the final ratio of incorporated N and Ga atoms in the thin film can be established:

$$R_f = \frac{R_{I/A}(1-\bar{r})}{\frac{1}{\delta(1+\beta)} - R_{I/A}\bar{s}}. \quad (2.27)$$

Concluding, it is to be noted, that the ion-to-atom ratio is different from the ratio of incorporated N and Ga atoms in the GaN film. Finding a relation between those two ratios requires a certain level of sophistication. Eq. (2.27) points out the general effect of the composition of the ion beam, surface sputtering, reflection of ions at the surface and charge exchange interactions in the gas on the ratio of Ga and N atoms in the final thin film. For more precise calculations, it is important to also consider e.g. the different cross-sections of different N ions for the charge exchange interactions and the dependence of temperature and film composition on the sputtering yield. Further, from this subsection it can be seen, that if an ion beam consisting of different ion species with possibly different reflection coefficients, sputtering yields and charge exchange cross-sections, analyzing dependencies in a growth process assisted by the irradiation with such an ion beam, becomes rather complicated. However, if there is the possibility to extract and employ only one particular ion species, the examination of such dependencies is facilitated.

2.2.3 Interaction of molecular ions with surfaces in IBAD

For the interaction of molecular ions with solid surfaces, depending on the kinetic energy of the ion, processes like sputtering, implantation and reflection as mentioned before might play a role in a similar way as for atomic ions. However, there are additional aspects that are to be mentioned for the application of molecular ions. For example Jacobs [Jac02] provides a general review about the interaction of molecular ions possessing hyperthermal energies with solid surfaces.

Whenever molecular ions are applied in IBAD or similar techniques, dissociation is a main process to be considered. In some contexts soft landing conditions [Joh16] are required, where molecular ions, which are typically larger and heavier in comparison to ions consisting of a single atom, are deposited on a surface without being fragmented. Though, in other contexts the dissociation of molecular ions is required. Vishnyakov *et al.* for example suggested that the stoichiometric formation of CrN by IBAD is promoted, if Ti atoms are introduced as a catalyst to dissociate N_2^+ ions [Vis06]. Furthermore, Park *et al.* [Par92] showed that for the nitridation of a Si surface the reaction probability of N_2^+ ions with the surface increases as a function of the kinetic energy for energies up to 20 eV. The reason is supposed to be that the molecular ions have to be dissociated for the reaction with the Si surface and the dissociation probability increases with increasing kinetic energy.

For the dissociation of molecular ions the distribution of the energy on the different degrees of freedom that the molecule possesses, plays a major role. It was for example shown that the O^- yield from NO^+ ions incident on GaAs is 10 times larger, if vibrational energy of the NO^+ molecule is increased instead of translational energy [Qui95]. Fig. 2.7 is a schematical depiction of the interaction of a surface consisting of the atoms A and an incident molecule consisting of the two atoms B and C. In the collision process vibrational states of the molecule are excited. If the energy of the vibration is sufficiently large the molecule can dissociate. Consequently, the remaining energy of the molecule is divided between two atoms, which are required e.g. for the incorporation in a thin layer. The dissociation probability, in this context, depends on the amount of energy that can be transferred from the kinetic energy of the incident molecule to the vibration and on the dissociation threshold energy. For the example of the N_2 molecule, the dissociation energy is 9.8 eV [Fro56].

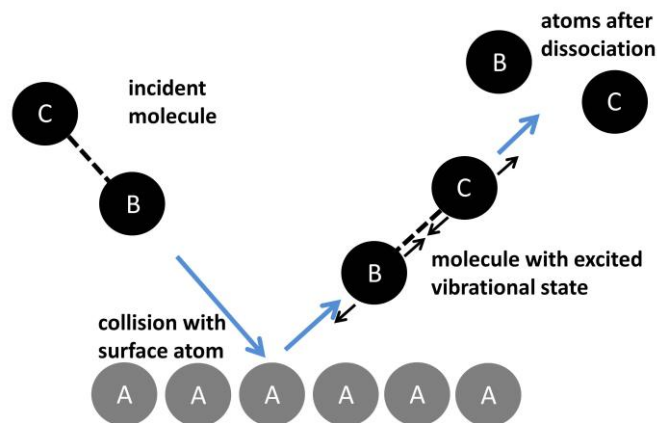


FIG. 2.7: Schematical depiction of the dissociation of an incident molecule consisting of the atoms B and C after a collision with a surface atom A. A vibrational excitation of the molecule precedes the dissociation.

The energy transferred to the vibration of the molecule in a head-on-collision can be estimated by assuming a certain interaction potential for the molecule and a surface atom [Aka90, Rap68]. According to such estimations a kinetic energy of 12 eV is required for a N_2 molecule to transfer 10 eV to the molecular vibration in a collision with e.g. an Al atom in a Al_2O_3 substrate.

2.2.4 Limitations of IBAD and consequences

The properties of the films produced by IBAD like e.g. texture, orientation, grain size, residual stresses and the quality and quantity of lattice defects significantly depend on the parameters of the ion beam irradiation [Nas96]. One of these ion beam parameters certainly is the kinetic energy of the ions, but also the ion current density, the mass and the charge play important roles. Therefore, the ion source is the essential device in IBAD. The ion source has to meet the requirements of the application, and the more degrees of freedom the ion source possesses, the higher is the control over the properties of the deposited material. Moreover, for assessing details about the processes on the surface during the growth of the material and obtain a deeper understanding of the IBAD growth process, an ion source with a high number of degrees of freedom is inevitable.

The drawbacks of IBAD as deposition technique are based on the limitations of the ion source applied in each case. Those limitations are in general the following:

- 1) Like in other plasma-based deposition techniques e.g. in magnetron sputtering [Pok13], also in IBAD several different ion species that differ from each other in mass and in charge, are generated. As will be shown later, one of the ion sources applied in the frame of this work produces N_2^+ and N^+ ions with a ratio of about 4:1. These two ion species differ in mass significantly (by a factor of 2). A second example is a broad-beam nitrogen ion source of the Kaufman-type [Kau90]. A typical mass spectrum generated by such an ion source, in addition to N^+ and N_2^+ , contains also small amounts of N^{2+} and N_3^+ [Zeu96]. Moreover, contaminations in the ion source and the process gas provide e.g. carbon, oxygen, water, argon and hydrocarbon ions. In ion sources like these two, there is no decisive control over the ratio of the different ion species that contribute to the growth process, which is a crucial limitation in precisely defining the conditions for an IBAD growth process.
- 2) In several ion sources the kinetic energy of the ions can be controlled in a certain range for example by applying an acceleration voltage. However, considering, that the ion beam typically consists of a blend of different ion species, it has to be assumed, that the relevant distribution of kinetic energy is a superposition of the energy distributions of all the different ion species. Thus, the relevant energy distribution is relatively broad and possibly

possesses multiple maxima. For a well-defined kinetic energy distribution, again control over the ion species is necessary.

- 3) For producing high-quality, epitaxial thin films, relatively low, hyperthermal ion energies are required (see subsection 2.2.1). For ion sources with grided ion extraction systems like in the case of the Kaufman-type ion source, due to space charge effects, the maximum ion current that can be emitted is $I \propto U^{3/2}$, where U is the acceleration voltage [Chi11]. Hence, the smaller the required kinetic energy, the smaller is also the achievable ion beam current, which is a limitation in precisely defining the conditions for the growth process, and which also leads to problems in providing sufficient ion current and simultaneously disseminating the ion energy to particles on the surface of the growing film in a suitable and non-destructive way.

Establishing these limitations motivates improving ion sources and increasing the number of accessible ion beam parameters. As a consequence of especially the first two listed limitations, a possibility to control the ion mass has to be introduced, while the control over the kinetic energy of the ions has to be maintained. Mass filter systems, if implemented in combination with an ion source, might achieve the control of the ion mass and be an appropriate component of an experimental setup for energy and mass selected IBAD. In general, the requirements for the applicability of a mass filter system in IBAD would be the following

- 1) Appropriate size of the device
- 2) High ion transmission
- 3) Possibility to generate hyperthermal ion beams
- 4) Sufficient resolution in ion mass
- 5) Adequate homogeneity of the generated ion beam

After taking into account these requirements, a quadrupole mass filter system is chosen for being coupled with a nitrogen ion source. A quadrupole mass filter basically consists of four rods with circular or hyperbolic cross-sections. A combination of applied RF and DC potentials causes specific ions to have stable oscillating trajectories between the rods and others to have unstable trajectories. For a general and more detailed explanation of the working principle of quadrupole mass filters see section 3.

If a quadrupole mass filter system is designed such that the above listed requirements are met and it is successfully brought into operation, the ions contributing to the growth process are expected to not only have a narrow distribution of kinetic energy, but also of mass, momentum and velocity, which facilitates the process of understanding thin film growth in IBAD. Finally, it opens up the possibility to improve the thin film properties by an enhanced control over the IBAD process.

3. The quadrupole mass filter system

As explained previously, an accurate investigation of thin film growth processes in IBAD requires the possibility to select ions with respect to their mass. Quadrupole mass filters are a possibility to realize such a mass selection. They are extensively used, especially in analytical contexts and their working principle is well known [Daw76]. In the frame of this work a quadrupole mass filter system is to be implemented into an experimental setup for ion-beam assisted molecular beam epitaxy (IBA-MBE) of nitride thin films. Considering that the ion mass filter, which is to be applied here, is to be used in a non-analytical and therefore unconventional way, the mass filter has to meet the requirements listed in subsection 2.2.4, which are stated more precisely in the following:

- 1) The spatial dimensions of the mass filter should be small to ensure that it can be implemented in an existing experimental setup with an appropriate amount of effort.
- 2) In thin film deposition the deposition rate is a quantity of high relevance. If only one particular out of many present ion species is chosen from an ion beam, the ion current apparently drops. Moreover, it can be expected, that the mass filter has a transmission of less than one for a particular ion species. The requirement for a mass filter applied in this context is that the ion current that is transmitted by the mass filter is sufficiently high for ensuring reasonable deposition rates.
- 3) As explained earlier, the kinetic energies that should be applied, if a high crystalline quality is aimed at, are in the order of hyperthermal energies. The kinetic energy of the ions must be selectable within the range of such energies. Simultaneously, its distribution must remain well-defined, i.e. the width of these distributions should be significantly smaller than the selected average kinetic energy in the region of hyperthermal energies. Moreover, the properties of an ion beam with hyperthermal energies are in many cases dominated by space charge repulsion. Considering this, the mass filter that is to be applied here has to generate an ion beam with hyperthermal energies and simultaneously fulfill the other requirements, particularly requirement 2). This implies that either it must be possible to operate the mass filter at such hyperthermal energies from the outset or the ions have to be decelerated between the mass filter and the target in order to obtain appropriate ion beam currents for higher and for lower energies within this range.
- 4) Using typical nitrogen ion sources it can be assumed that the relevant ions are N^+ and N_2^+ ions. The mass selection must work according to the theory of quadrupole mass filtering. In that context, the mass resolution must be high enough so that it is possible to generate an ion beam consisting only of the latter or the former ion species. Additionally, the requirements 2) and 3) must be fulfilled for both ion species.

- 5) In the frame of this work deposition processes are to be carried out on substrate areas of $1 \times 1 \text{ cm}^2$. Obviously, the shape of the ion beam should match this condition and the ion beam current should be as homogeneous as possible on a scale of a few mm.

Taking into account the above list, it becomes clear that finding an instrumentation, which fulfills all these requirements, comprises a certain level of sophistication. There are a few examples for the application of quadrupoles and different ion mass filters in comparable contexts [Gri01]. Though, the quadrupole mass filters, which are available commercially, are typically built for different purposes. Hence, in order to pave the ground for accurate investigations of IBAD processes in dependence of ion beam parameters, a custom quadrupole mass filter was designed and built for this work. This prototype of a quadrupole mass filter suitable for the implementation in IBA-MBE setups was put into operation for the first time as part of this work [Ger17].

This section starts by concisely summarizing the general working principle of quadrupole mass filters. Consequently, it describes the quadrupole mass filter system applied in this context. After that, details about the mass and energy selection as well as the properties of the resulting ion beam are presented and regarded with respect to the listed requirements. Finally, the influence of space charge effects on the limitation for the achievable ion current is discussed.

3.1 The working principle of a quadrupole mass filter

Detailed reviews about quadrupole mass spectrometry and the behavior of ions in quadrupole fields are given e.g. by the references [Mar89], [Pau58] and [Ger92], while references [Lea96] and [Mil86] are examples for short semi-quantitative and intuitive introductions to quadrupole mass filtering. In quadrupole systems there are four rod-like electrodes, which ideally have a hyperbolic cross-section. For practical reasons, typically circular cross-sections are employed. The radius of each of the four electrodes is r . As depicted in Fig. 3.1 (a) the four electrodes are arranged parallel to each other such that in the cross-section there is a circular region of free space (radius r_0) between the electrodes. A radio frequency (RF) voltage with an amplitude $2 U_{RF}$ and a frequency $f = \omega/2\pi$ is applied between neighboring quadrupole electrodes, while the same potential is applied to opposite rods at any time. In addition to the RF voltage there is also DC potentials U_{DC} applied to the electrodes. The potential applied to neighboring electrodes alternates in sign. Therefore, the DC voltage between neighboring electrodes is $2U_{DC}$ and the total voltage between those sums up to

$$V(t) = 2[U_{DC} + U_{RF} \cos(\omega t)] . \quad (3.1)$$

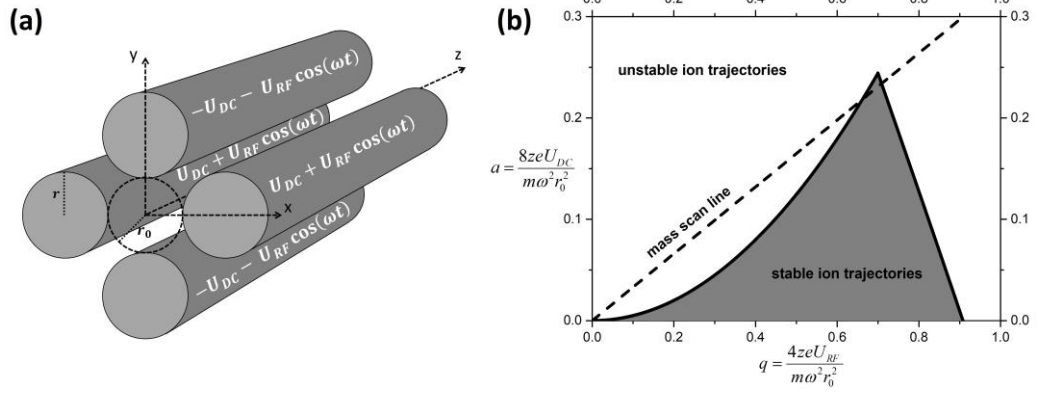


FIG. 3.1: (a) A schematic cross-section through the quadrupole (b) The diagram of stable ion motion in the q - a parameter space as it results from the solution of the equations of motion for ions inside of a quadrupole mass filter.

If the ratio of the above mentioned radii is $r/r_0 = 1.145$, the parasitic 12-pole term of the electric field of four circular electrodes vanishes and the electric field can be approximated by a hyperbolic field. The potential as a function of the position on the cross-section consequently is

$$\phi(x, y, t) = V(t) \frac{x^2 - y^2}{2r_0^2}, \quad (3.2)$$

where the quadrupole electrodes are aligned in z -direction. From the electric potential the electric force and finally the equations of motion for ions with mass m and charge ze in x - and in y -direction can be derived:

$$\ddot{x} = -2[U_{DC} + U_{RF} \cos(\omega t)] \frac{zex}{mr_0^2}, \quad (3.3)$$

$$\ddot{y} = 2[U_{DC} + U_{RF} \cos(\omega t)] \frac{zey}{mr_0^2}. \quad (3.4)$$

For rewriting these differential equations the parameter $\xi = \omega t/2$ is defined. The second derivative of a coordinate u (x or y) with respect to the time, then becomes

$\ddot{u} = \frac{\omega^2}{4} \frac{d^2u}{d\xi^2}$. Furthermore the stability parameters a and q are defined:

$$a = \frac{8ze}{m\omega^2 r_0^2} U_{DC}, \quad (3.5)$$

$$q = \frac{4ze}{m\omega^2 r_0^2} U_{RF}. \quad (3.6)$$

This way eq. (3.3) and eq. (3.4) can be reduced to

$$\frac{d^2u}{d\xi^2} = [a + q \cos(2\xi)]u, \quad (3.7)$$

where a and q have a positive sign for $u = y$ and a negative one for $u = x$. Eq. (3.7) is the Mathieu's differential equation. A solution of this equation is

$$u = \alpha_1 e^{\mu\xi} \sum_{n=-\infty}^{\infty} C_{2n} e^{2in\xi} + \alpha_2 e^{-\mu\xi} \sum_{n=-\infty}^{\infty} C_{2n} e^{-2in\xi}. \quad (3.8)$$

Here, α_1 and α_2 depend on the initial conditions only, while the constants μ and C_{2n} only depend on the stability parameters a and q . The ion motion inside a quadrupole is stable, if u remains finite for $\xi \rightarrow \infty$. Physically this means that the ion motion is confined within the quadrupole rods. However if this is not fulfilled the ion motion inside the quadrupole is unstable, which means that the ions leave the space between the rods e.g. by colliding with one of the rods. For $\mu = i\beta$ and $0 < \beta < 1$ the criteria for stable ion motion is fulfilled. Then the solution of Mathieu's equation and therefore the ion motion inside of the quadrupole is an infinite series of harmonic oscillations. The frequency of the slowest oscillation is $\Omega = 0.5\beta\omega$. β is a number depending only on the stability parameters a and q . An approximate formula for β as a function of a and q is given by [Daw76]

$$\beta \cong \sqrt{a - \frac{(a-1)q^2}{2(a-1)^2 - q^2} - \frac{(5a+7)q^4}{32(a-1)^3(a-4)} - \frac{(9a^2+58a+29)q^6}{64(a-1)^5(a-4)(a-9)} + \dots}. \quad (3.9)$$

It can be shown, that ion motion is stable, i.e. $0 < \beta < 1$, if the stability parameters a and q are within a region limited by the following polynomials [Wue59]:

$$a = \frac{1}{2}q^2 - \frac{1}{128}q^4 + \frac{29}{2304}q^6 - \frac{68687}{18874368}q^8 + \dots, \text{ and} \quad (3.10)$$

$$a = 1 - q - \frac{1}{8}q^2 + \frac{1}{64}q^3 - \frac{1}{1536}q^4 - \frac{11}{35864}q^5 + \dots. \quad (3.11)$$

This region is called stability diagram and is depicted in Fig. 3.1 (b). Typically, a quadrupole mass filter is operated along mass scan lines, where U_{DC} and U_{RF} are varied while keeping their ratio constant. If the mass scan line is chosen as in Fig. 3.1 (b), there is only a small region, for which the mass scan line overlaps with the stability diagram. This means that for a given mass-to-charge ratio of the ions only a narrow range of U_{RF} allows for transmission. Ions that have a larger or a smaller mass-to-charge ratio are transmitted for a narrow range of U_{RF} which is situated at larger or smaller U_{RF} , respectively. Hence, the mass-to-charge ratio of ions to be transmitted by the quadrupole can be selected by choosing the values U_{DC} and U_{RF} .

3.2 Mass filter setup

The custom quadrupole mass filter system, as it is employed in the frame of this work, is depicted in Fig. 3.2 including a schematics and a photograph. It consists of first a source region, where ions are generated and focused, second the quadrupole segments, where the mass selection takes place and third ion optics for a high controllability of the ion beam. The components of the quadrupole and their purposes are explained in this subsection in the same order as the ions pass them.

The ions are generated either by a constricted DC glow-discharge plasma source (hollow-anode source) or a Kaufman-type broad-beam ion source. The former device delivers a streaming nitrogen plasma predominantly containing atomic (N^+) and molecular (N_2^+) nitrogen ions with kinetic energies of less than 25 eV. The latter delivers a nitrogen ion beam containing also different ion species with selectable kinetic energy. The hollow-anode source is typically operated with a nitrogen mass flow of 2.5 sccm, which leads to a pressure of 4×10^{-2} Pa close to the center of the quadrupole system. The pressure in the region between the quadrupole system and the sample position is approx. 3×10^{-3} Pa. The Kaufman ion source is operated with a mass flow, which is even smaller, yielding smaller pressures, correspondingly. Details on the ion sources will be given in section 4.

The distance between one of the two sources and the first electrode, which is a stainless steel grid with a transparency of 70%, is approximately 2 cm. In the case that the hollow-anode source is applied, the purpose of this grid is to shield the entry region of the quadrupole system from the nitrogen plasma. Then, typical potentials in the range between $30 \text{ V} < U_{grid} < 50 \text{ V}$ are applied to this grid. The measured current between this grid and ground for this range of potentials is negative and its absolute value is larger than 30 mA. This means, that a high number of electrons is removed from the plasma by this grid and the extraction of ions from the plasma into the quadrupole is initiated here. Subsequently, there is a stack of ring electrodes, which are labelled as entry electrodes (2-6). Here, the typically applied potentials are also positive, thus the extraction of ions from the plasma is continued. A second purpose of these electrodes is to focus the extracted ions close to the quadrupole axis. After these electrodes, there is a stack of three quadrupole segments, which are used for mass filtering. Subsequently, there is a set of ion optics including a deflector, which is used to direct the ions towards the sample. A second purpose of these electrodes is to focus the extracted ions close to the quadrupole axis.

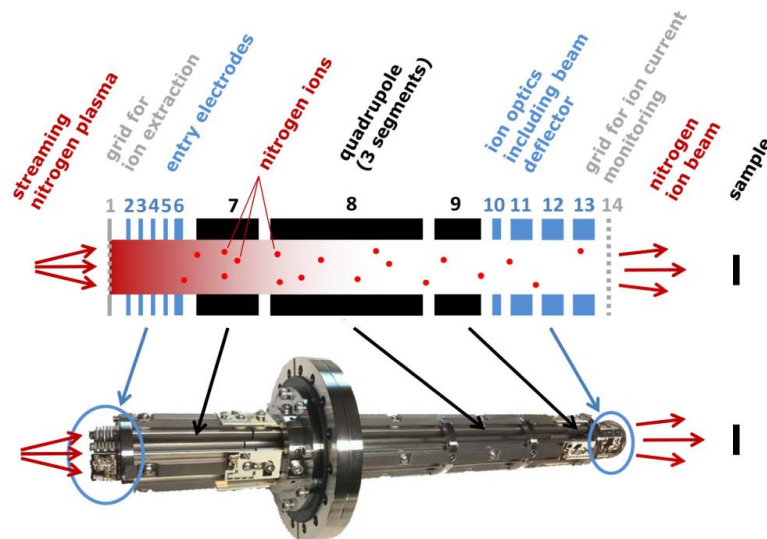


FIG. 3.2: Schematics and a photograph of the quadrupole mass filter setup (from left to right): ion extraction grid, set of entry electrodes, three separate quadrupole segments, set of ion optics as well as beam current monitoring grid as used e.g. in combination with a constricted DC glow-discharge plasma source.

For the application of the Kaufman ion source, the extraction of the ions from the plasma already takes place in the two-grid ion extraction system of the ion source. Therefore, the entry electrodes are used for focusing purposes only.

The following set of quadrupole rods is divided into three segments (7-9) each being characterized by a field radius of $r_0 = 8.75$ mm and a rod radius $r = 10$ mm. The ratio of these two radii is close to the value, for which the assumption of a hyperbolic electric field is most suitable (see previous subsection), so that the behavior of the quadrupole is expected to be close to the ideal, theoretical behavior. In all three segments an RF voltage of constant frequency $f = 3$ MHz, but variable amplitude of up to 1.2 kV is applied to the rods at opposite polarity for neighboring rods (see also Fig. 3.1 (a)). For a given ion species, the frequency f and the amplitude of the RF voltage U_{RF} are related to each other by eq. (3.6), since stable ion motion is achieved only for certain values of the stability parameter q . If the frequency f is increased by a factor of n , the amplitude of the RF voltage U_{RF} has to be increased by n^2 . This on the one hand is beneficial, because it leads to a better ion confinement, but on the other hand the electrical supply becomes increasingly challenging [Cer05]. Therefore, the above given values for f and U_{RF} were found as compromise between the electric losses and the depth of the effective potential confining the ions in the quadrupole field. In addition to the RF potential, DC potentials can be applied to each of the three segments. For the first quadrupole segment (7), U_{entry} is applied to all four rods, the same potential is also applied to the last of the entry electrodes (6). In a similar way, for the last quadrupole segment (9), U_{exit} is applied to all four rods and simultaneously to the first of the exit electrodes (10). For these two quadrupole segments, there is no DC voltage between quadrupole rods, thus these segments are operated in RF-only mode. This means, that in these cases the quadrupole solely acts as an ion guide. The central quadrupole segment (8) is the part of the setup, where the selection of ions with respect to their mass-to-charge ratio takes place. Therefore, here a DC voltage of $2U_{DC}$ as shown in Fig. 3.1 (a) is applied between neighboring quadrupole electrodes. In addition to this voltage the axis potential U_{axis} can be applied to all four quadrupole electrodes in this segment. The implementation of three separate quadrupole segments with their respective function was suggested by Dawson [Daw71] to decrease the loss of ions when coupling into and out of the mass filtering quadrupole by reducing the influence of fringing fields.

After passing all three quadrupole segments the ions enter another stack of ring electrodes (10-13). These electrodes act as ion optics and their purpose is to control the shape of the beam as well as to focus the ion beam. Voltages that can be applied between two halves of electrode 12 and electrode 13 additionally enable x-y-deflection of the ion beam. Finally, the ion beam passes a high-transparency (96%) stainless steel grid (14), which is grounded. This grid not only shields the region between the quadrupole system and the sample from potentials applied to any electrode, but also monitors the ion beam current leaving the quadrupole system. Due

to the potentials applied to the above mentioned electrodes the ions are subjected to a potential sequence, for which one example is given in Fig. 3.3 for each source device. Both exemplary potential sequences were applied to obtain ion beams consisting of N^+ ions with the maximum of the kinetic energy distribution at 80 eV. For the application of the hollow-anode source, it is discernable, that relatively high, positive potentials are necessary in the entry region in order to achieve the extraction of ions from the plasma. For both cases the applied potentials for the quadrupole segments and the ion optics were optimized in order to obtain maximal ion beam current a few cm behind the quadrupole. The result of this maximization process as it is shown in Fig. 3.3 can be identified to be typical for an Einzel lens (see e.g. [Mal88]).

The total length of the quadrupole system from the ion extraction grid (1) to the ion current monitoring grid (14) is approximately 55 cm, where the center quadrupole segment (8) is the longest component of the system with a length of 34.6 cm. Phelps [Phe91] provided a list of cross-sections for collisions of nitrogen ions in nitrogen gas. For the region between the exit of the quadrupole system and the sample the mean free paths are larger than the dimensions of the setup, so that collisions can be neglected. However, inside of the quadrupole a pressure of 4×10^{-2} Pa using the hollow-anode source and a pressure of 1.5×10^{-2} Pa using the Kaufman ion source lead to mean free paths of approx. 15 cm and 40 cm, respectively, for collisions of N_2^+ ions with a kinetic energy of 40 eV and nitrogen molecules with transfer of momentum. For collisions with N^+ ions and collisions, where charge transfer plays a role, the cross-sections are significantly smaller, so that they can be neglected.

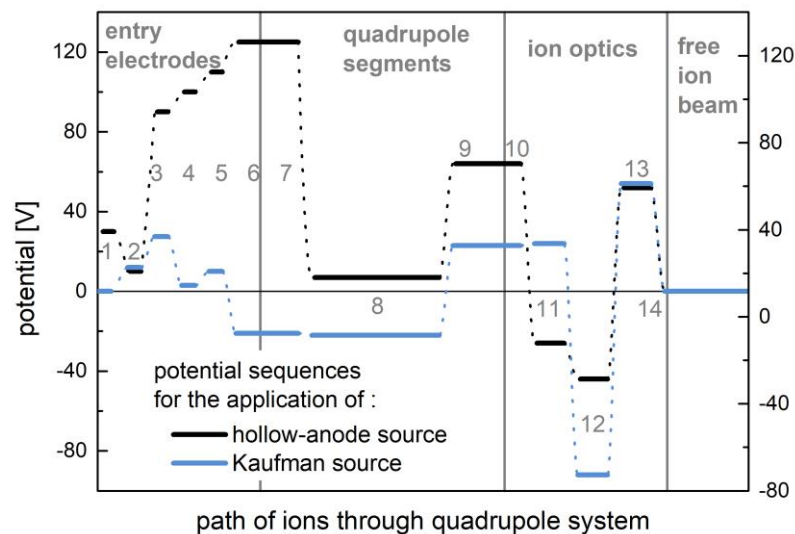


FIG. 3.3: Two examples for a potential sequence inside the mass filter system. These configurations of potentials were both used to generate ion beams with N^+ ions with the maximum of the kinetic energy distribution at 80 eV. The depicted potentials are for the application of the hollow-anode source (in black) and of the Kaufman ion source (in blue).

Nevertheless the pressure in the regions near the ion source is presumably larger than 4×10^{-2} Pa, so here collisions with charge as well as momentum transfer might be more prominent.

3.3 Ion mass selection

In order to characterize the performance of the previously described quadrupole system, the ion beam current was measured with a retarding field analyzer (RFA) in the position of the sample. This RFA consists of a Faraday cup and a Cu grid with a transparency of 35 %, which enables measurements of ion kinetic energy. The orifice of this device has a diameter of 5 mm. With the aim to verify the feasibility of mass separation with this mass filter system, ion current measurements were conducted in dependence of the DC potential U_{DC} and the RF amplitude U_{RF} . An exemplary result of such measurements is depicted in Fig. 3.4. In this parameter space, for every mass-to-charge ratio a region of stable ion motion, comparable to the diagram shown in Fig. 3.1 (b), appears.

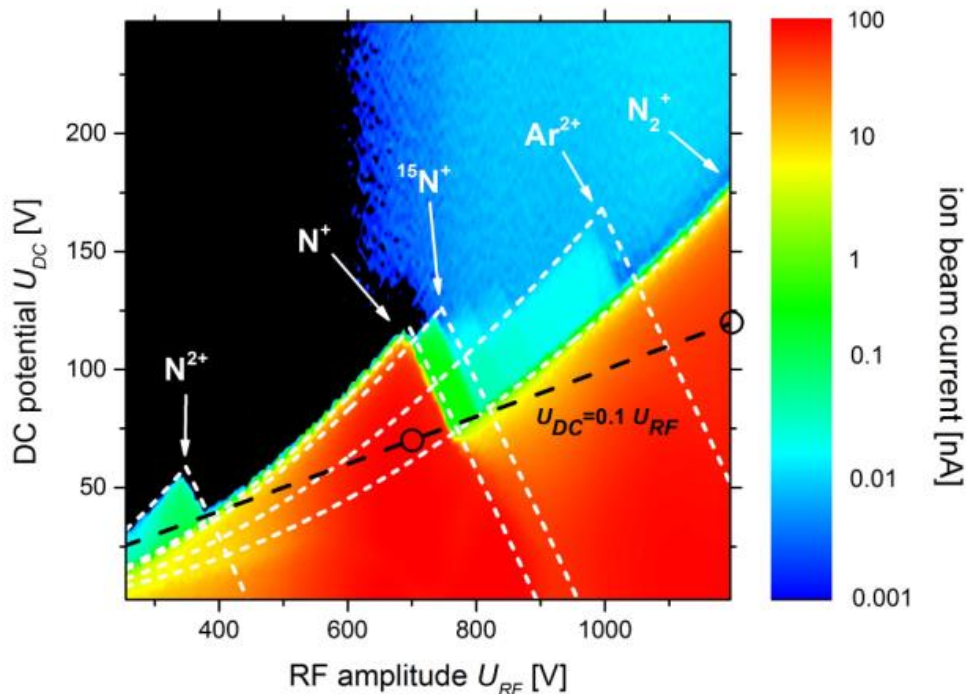


FIG. 3.4: Ion beam current measured with the RFA at the sample position, plotted in dependence of the DC potential U_{DC} and the RF amplitude U_{RF} applied to the quadrupole rods. In this measured stability diagram, the triangularly shaped stability regions of the most prominent ion species the ion beam consists of are denoted. The dashed white lines correspond to the calculated border lines of the regions of stable ion motion. The dashed black line indicates a typical mass scan line, on that particular ion species are selected. The black circles indicate practically chosen operating conditions.

According to eq. (3.5) and (3.6), the tip of the region of stable ion motion is shifted to larger U_{RF} and to larger U_{DC} for increasing mass-to-charge ratio. The white, dashed lines correspond to the boundaries of the region of stable ion motion as calculated from eq. (3.10) and (3.11) for different ion species. From this measurement different ion species that are generated by the hollow-anode source can be identified. There are atomic nitrogen ions present. These are either charged twice (N^{2+}) or once. For the latter, two different isotopes are distinguishable ($^{14}N^+$ and $^{15}N^+$). Due to a low content of argon in the working gas that the plasma source is operated with, in this mass spectrum a contribution of twice charged argon ions (Ar^{2+}) is visible. Finally, for high U_{RF} a region of stable ion motion for molecular nitrogen ions (N_2^+) emerges. The two main contributions to this mass spectrum originate from the N^+ and the N_2^+ ions. There is agreement between the measured ion currents and the calculated boundaries of the stability diagram. Hence, it is demonstrated that the presented setup is capable of separating different ion species, particularly N^+ and N_2^+ ions, by choosing suitable values for U_{DC} and U_{RF} . In order to obtain optimal mass resolution the quadrupole is to be operated on a mass scan line, that passes through the tips of the regions of stable ion motion (similar as in Fig. 3.1 (b)). Here, for N^+ the two different isotopes can be separated. The optimal mass resolution therefore is at least $M/\Delta M = 14$. In the frame of this thesis, however, the mass resolution only needs to be high enough to accomplish separation of N^+ and N_2^+ ions. Since mass resolution and transmission counteract each other [Daw90], the quadrupole is operated under the chosen condition $U_{DC} = 0.1U_{RF}$ in order to allow for reasonable ion currents while still separating N_2^+ and N^+ ions. The corresponding mass scan line and the position of two typical points for the operation of the quadrupole are included in black in Fig. 3.4.

In order to illustrate the working principle of the quadrupole mass filter, ion trajectory simulations using the program package SIMION [Dah11] were performed with a workbench program written in lua. The workbench program for this case is added to the appendix. Fig. 3.5 shows results that were obtained by such trajectory simulations. For this case, 100 N^{2+} ions, 400 $^{14}N^+$ ions, 100 $^{15}N^+$ ions and 400 N_2^+ ions were assumed to enter the three quadrupole segments and the total number of ions, which leave the third quadrupole segment, was determined in dependence of U_{RF} and U_{DC} . This way, the regions of stable trajectories, as they were measured before (Fig. 3.4) can be reproduced by trajectory simulations. Three specific points inside of this parameter space are to be mentioned here. For the point (b), N^+ ions (depicted in black) are transmitted and N_2^+ ions (depicted in red) collide with the rod electrodes and are lost, consequently. This is illustrated by the projection of the ion trajectories on the cross-section of the quadrupole. The N^+ trajectories are confined within a well-defined distance from the quadrupole axis, which is smaller than r_0 . The N_2^+ ions being significantly heavier cannot react sufficiently fast on the time-dependent RF potential. Therefore, the attraction by the time-independently and negatively biased quadrupole rods governs the behavior of the N_2^+ trajectories.

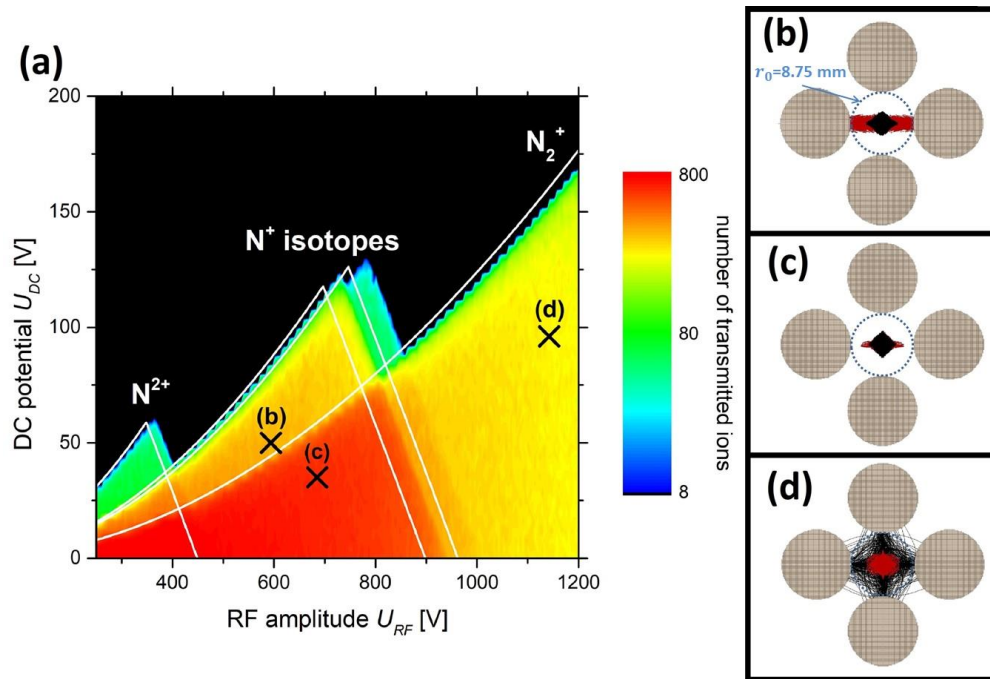


FIG. 3.5: For the plot (a) the trajectories of 100 N_2^+ ions, 400 $^{14}N^+$ ions, 100 $^{15}N^+$ ions and 400 N_2^+ ions were simulated inside of the three quadrupole segments for different combinations of U_{RF} and U_{DC} . The total ion transmission was determined by this simulation and plotted. The calculated borders of the regions of stable trajectories are illustrated as white lines. For the marked spots in this parameter space (b)-(d), the trajectories of N_2^+ ions (in red) and for N^+ ions (in black) are depicted on a cross-sectional projection of the quadrupole.

Moving to the bottom right in the U_{RF}/U_{DC} parameter space, the point (c) represents the situation, where the ion trajectories of both $^{14}N^+$ and N_2^+ ions are confined within the quadrupole field. At point (d), N_2^+ ions are again trapped inside the quadrupole potential. U_{RF} is sufficiently large for dominating the influence on the trajectories of light N^+ ions, i.e. these trajectories are oscillating with amplitudes that reach r_0 after a certain time. Therefore N^+ ions are not transmitted by the quadrupole mass filter in this case.

3.4 Ion energy selection

The kinetic energy of the ions generated by the hollow-anode source and transmitted by the quadrupole system was measured using the RFA in the position of the sample. It was found that, depending on the operation condition of the plasma source, the potential sequence inside the quadrupole and the ion species, the DC potential applied to the last entry electrode (6) and the first quadrupole segment (7) U_{entry} and the DC potential applied to the center quadrupole segment (8) U_{axis} may be the most prominent parameters to influence the kinetic energy distribution. Two exemplary cases are presented in Fig. 3.6 (a) and (b). Three distributions of kinetic energies were measured here. First for N^+ ions changing only U_{entry} and second for N_2^+ ions

changing some of the potentials applied to the entry electrodes, but mainly U_{axis} . It is obvious from these examples, that the position of the peak in the distribution of the kinetic energy can be shifted to a required value within the depicted interval of up to 120 eV. The shape of the measured distributions of kinetic energy is reproduced by Gaussian fits. In some cases, the energy distribution seems to be composed of two Gaussian functions, where one of those two functions is significantly narrower than the other. For a few energy distributions, there are distinct deviations from the Gaussian behavior on the high-energy side. Such a 'high-energy tail' for hyperthermal ions transmitted by a quadrupole was already observed in different contexts (see e.g. [Bod13]). However, the extent of these high-energy tails here is small enough to allow for investigating the basic influences of the ion kinetic energy on film growth processes. The fact that the average kinetic energy can be shifted as described above can be explained by regarding the described experimental setup. In the beginning the plasma is generated in the hollow-anode source. When the plasma leaves this source through a nozzle, the particles in the plasma are gas-dynamically accelerated, due to the pressure gradient. The resulting kinetic energy of the ions after leaving the plasma source is smaller than 25 eV.

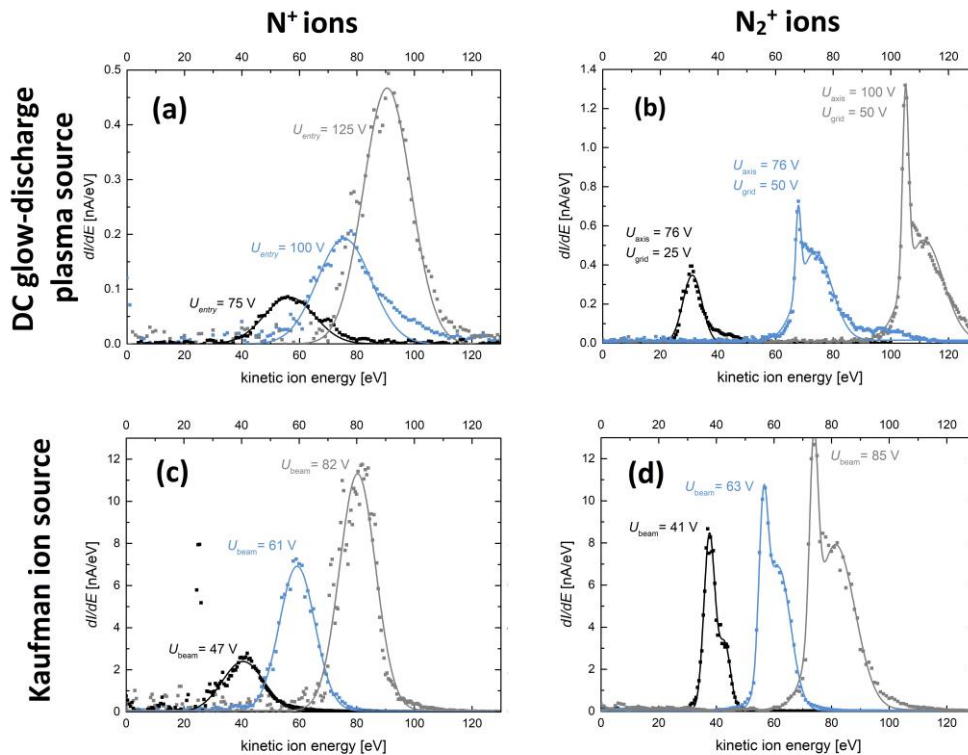


FIG. 3.6: Distributions of kinetic energy for (a) N^+ ions generated by the hollow-anode source varying U_{entry} and (b) N_2^+ ions generated by the same source varying U_{axis} , as determined at the sample position by using the RFA. For the measurement plotted in black in (b) the potentials of the entry electrodes were also changed, in particular that of the ion extraction grid (1). (c) and (d) depict three exemplary energy distributions, where the Kaufman ion source was used, regarding N^+ ions and N_2^+ ions, respectively. The quadrupole system electrodes were optimized for each case. Nonetheless, U_{beam} defines the peak position of the distribution.

Consequently, the ions arrive in the region of the entry electrodes, where they are extracted from the plasma while also leaving a region of high pressure. Here, the behavior of N^+ and N_2^+ ions might differ significantly, due to the different mass and the different particle size that leads to different cross-sections for collisions between the ions and the particles in the background gas. Additionally, the potential sequence that is chosen for the operation of the quadrupole might influence the location, where the ions are extracted from the plasma. In principle, the ion energy selection works as follows: When the ions enter a region of the quadrupole system with a positive potential, they are not decelerated, because of screening effects related to the plasma or because of collisions with other particles from the gas. In the respective region of the quadrupole the ions are extracted from the plasma and leave the region of high pressure. Therefore, the ions are accelerated when they leave this region. When they arrive at the surface of the sample, which is on ground potential, they have a kinetic energy, which is related to the positive potential applied to the respective region of the quadrupole.

Kinetic energy distributions were also measured by the RFA for the case, that the ions are generated by the Kaufman ion source. Such exemplary measurements can be seen in Fig. 3.6 (c) and (d). Here, the ions are extracted from the plasma already in the two-grid ion extraction system of the ion source and it can be assumed, that the energy distribution of the ions entering and leaving the quadrupole mass filter system is the same. Additionally, the ions arrive with the same energy distribution on the grounded sample surface.

As can easily be discerned from Fig 3.6 (c) and (d), the kinetic energy is determined by the potential of the Kaufman ion source U_{beam} with respect to the grounded sample surface. Also in this case the shape of the energy distributions can be reproduced well by Gaussian functions.

The widths of the Gaussian fits shown in Fig. 3.6 are plotted in Fig. 3.7. Note that these are exemplary, but representative energy distributions. The width of the energy distributions may deviate in experiments as they will be presented in section 5, because the potentials applied to the quadrupole and the operation condition of the ion source might be chosen differently. Here, the FWHM of the energy distributions is below 25 eV. For the energy distribution of N_2^+ ions, it can be observed that the FWHM tends to decrease with decreasing average kinetic energy. For small energies ($E_{kin} < 80$ eV), the FWHM is even smaller than 15 eV. Comparing the two ion sources, it is conspicuous that particularly for the generation of N^+ ions, applying the Kaufman ion source yields a FWHM, which is smaller by approx. 5 eV. This is because the extraction of the ions is well defined within the Kaufman source. In comparison, the extraction of the ions within the entry electrodes of the quadrupole like in the case of the hollow-anode source is a less precise method to control the kinetic ion energy. For both ion sources, if the kinetic energy distribution of N_2^+ ions is measured, a narrow peak can be observed.

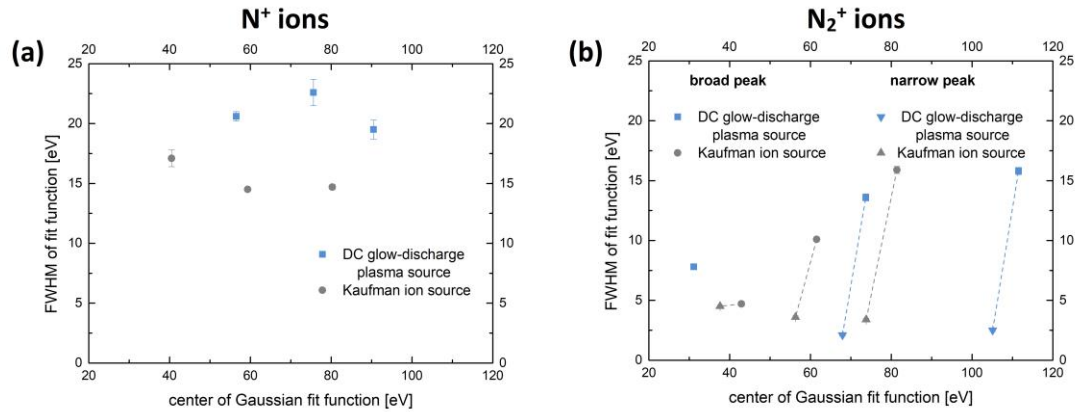


FIG. 3.7: The fit parameters of the exemplarily shown kinetic ion energy distributions in Fig. 3.6. In (a) the obtained FWHM is plotted in dependence of the center position for the application of N^+ ions and in (b) for the application of N_2^+ ions. In the latter case both the contribution of the broad and the narrow component are included. The FWHM obtained for the same energy distribution are connected by dotted lined to facilitate the association.

This peak is situated a few eV below the maximum of the broad contribution to the energy distribution and its FWHM is below 5 eV. The occurrence of such a narrow peak might be related to thermalization processes [Mey81, Gra83]. In collisions with the background gas in or near the region of ion extraction, a certain fraction of the N_2^+ ions might lose kinetic energy and obtain the well-defined thermal energy. When leaving the region of ion extraction or its vicinity, these ions are accelerated, while maintaining the narrow width of the kinetic energy distribution. This thermalization peak is mainly observable in energy distributions of N_2^+ ions, since N^+ ions have a significantly smaller cross-section for collisions with any particles from the background gas.

In conclusion, it can be summarized, that the kinetic energy of the ions can be controlled and selected for both of the applied ion sources. The ion energy distributions exhibit FWHM of approx. 20 eV or less. Thus, the kinetic energy of the ions is also sufficiently well-defined.

3.5 Ion beam characteristics

The ion beam current and the ion current density are important parameters with respect to the duration of thin film deposition processes, while the ion beam profile is important for the homogeneity of the resulting thin film. In this context, ion beam current measurements and ion trajectory simulations are presented to characterize the these quantities for the present setup.

3.5.1 Ion currents

In Fig. 3.8 (a) the ratio of the ion current measured with a Faraday cup on an area of $1 \times 1 \text{ cm}^2$ and the total ion beam current that is measured by the beam monitoring grid is plotted in dependence of the distance from the quadrupole exit. Each measurement point here is an average value from several measurements using N^+ ions generated by the hollow-anode source. The fraction of the whole ion current arriving on this area decreases with increasing distance from the quadrupole. This is an indication for ion beam divergence. Furthermore, a disc with a diameter of 5 cm was also used to measure the ion current in dependence of the distance from the quadrupole exit. For such a large ion collecting area, it is expected that first the measured ion current remains constant until a certain distance from the quadrupole is reached. At this point, the width of the divergent beam exceeds the size of the measuring device and the measured ion current starts to decrease. This is indeed observed here (see Fig. 3.8 (a)):

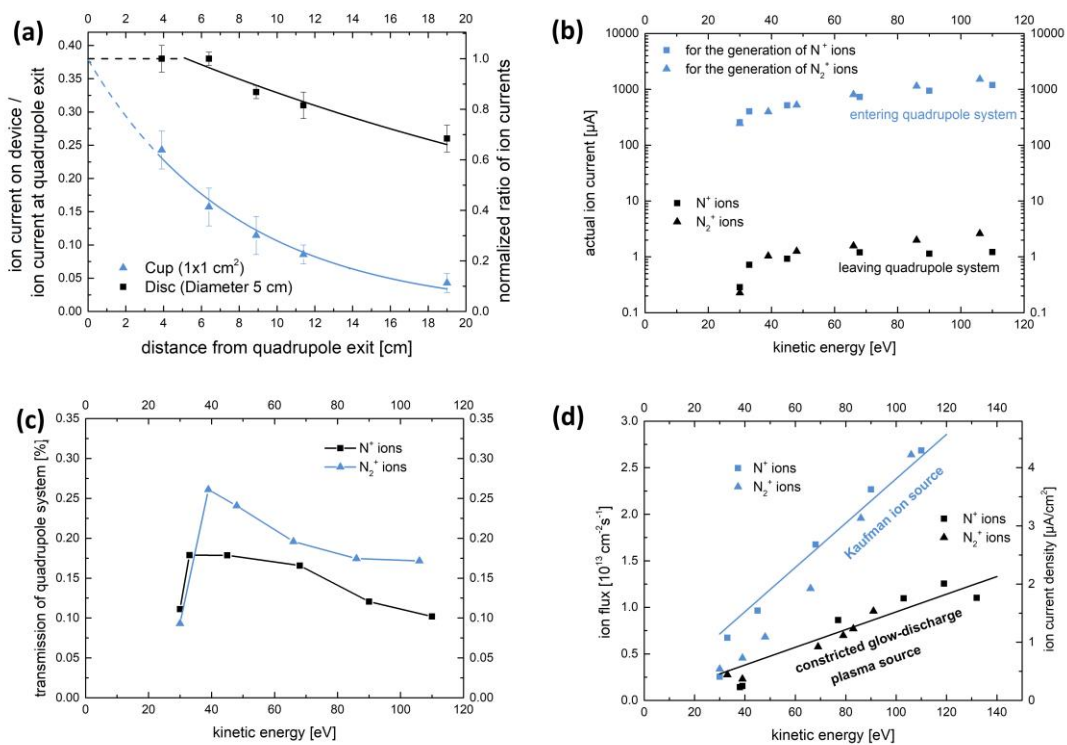


FIG. 3.8: (a) Ion current measured on a disc with a diameter of 5 cm (black) and on a Faraday cup with an area of $1 \cdot 1 \text{ cm}^2$ (blue) divided by the total ion beam current measured by the beam monitoring grid (14 in Fig. 3.2), plotted in dependence of the distance from the current monitoring grid (14). (b) The ion beam currents entering the quadrupole system measured by the entry grid (1) and both the N^+ and the N_2^+ ion currents leaving the quadrupole system measured by the current monitoring grid (14). These currents were measured with the Kaufman ion source in operation. (c) The transmission of the quadrupole as the fraction of the two ion currents depicted in (b). (d) Achievable ion current densities plotted in dependence of the ion kinetic energy for N^+ ions (squares) and for N_2^+ ions (triangles) at a distance of 7.5 cm from the ion current monitoring grid (14), which corresponds to the position of the sample.

The fraction of the ion current on the measuring device starts to decrease beginning from 5 cm from the quadrupole exit. Note, that for both devices the maximum measurable ion current is 38% of the current measured by the beam monitoring grid. The grid is mounted on a conducting ring, it is therefore assumed, that the ion current measured by the mounted grid is larger than the available ion beam current behind this grid. Taking this into account, it is observed, that in a distance of 7.5 cm approx. 90% of the total, available ion beam current is collected on a circular area with a diameter of 5 cm. From this it is concluded that the ion beam has a FWHM of 3.5 cm, if a Gaussian shape is assumed. In order to decrease the necessary deposition duration by increasing the ion current densities, it is beneficial to bring the sample as close to the quadrupole as possible. The chosen distance of 7.5 cm is a compromise between the requirement of large ion current densities and the necessity that also the Ga flux can arrive on the sample surface without being shadowed by the quadrupole exit.

If the Kaufman ion source is applied, it is possible to measure the current of the ions entering the quadrupole I_{in} . Note that in this position the mass separation has not taken place yet, and all ion species contribute to I_{in} . Moreover, assuming that 38 % of the current measured by the beam monitoring grid at the exit of the quadrupole system actually leaves the quadrupole system (as previously explained), currents of particular ion species leaving the quadrupole system I_{out} can also be measured. Consequently a transmission of the quadrupole for N^+ and N_2^+ ions can be defined as I_{out}/I_{in} . For the case, that the ion current density measured by the RFA in the sample position was maximized, those I_{out} and I_{in} are plotted in Fig. 3.8 (b) in dependence of the kinetic energy. In general, the current of entering ions is in the range of $200 \mu A < I_{in} < 1.5 \text{ mA}$, while the current of exiting ions lies in the range of $0.2 \mu A < I_{out} < 3 \mu A$ depending on the kinetic ion energy. The resulting transmission as I_{in}/I_{out} is plotted in Fig. 3.8 (c). Its value is of the order of 0.1%. For most of the relevant region of ion kinetic energies, the transmission is significantly larger for N_2^+ ions than for N^+ ions. The probable reason is that similar to the hollow-anode source, also the Kaufman ion source generates more N_2^+ ions than N^+ ions. For the chosen operation distance of 7.5 cm, Fig. 3.8 (d) illustrates the maximum achievable ion current densities which are measured by the RFA in dependence of the average kinetic ion energy. Clearly, the ion current density decreases with decreasing kinetic ion energy. The reason for this behavior can in principle be space charge effects. For more sophisticated considerations concerning space charge effects see subsection 3.6. Moreover, it is discernable, that the obtainable ion current density on the sample is generally larger, if the Kaufman ion source is applied. A reason might be that due to the early ion extraction from the plasma, the coupling of the ions into the RF potential is more efficient. This might increase the transmission of the whole quadrupole system. According to the Brice model as shown in subsection 2.2.1 the optimum kinetic energy is in the range of $20 \text{ eV} \leq E_{opt} \leq 40 \text{ eV}$, if GaN thin films of high crystalline quality are to be deposited using N^+ ions. Within this range of kinetic energies, the ion current density, which can be achieved here, is $j \sim 0.4 \mu A \text{ cm}^{-2}$, if the hollow-anode

source is applied. If the Kaufman ion source is put into operation, the obtainable ion current density is approximately twice as much. Assuming that all ions, which are detected here, contribute to the growth process, a GaN thin film with a film thickness of 10 nm can be produced within a few hours. Note, that for molecular ions twice as much N is provided compared to atomic ions, if the ion current density is the same. Moreover, as mentioned in subsection 2.2.3, for molecular ions, theoretically, a certain energy is necessary to dissociate the bond between the nitrogen atoms before they can contribute to the growth process. Consequently, the remaining energy is divided upon two particles. On this account, in the case of deposition using N_2^+ ions the kinetic energy as well as the ion current density can presumably be larger, so that the deposition is actually faster.

3.5.2 Ion beam profile

In order to measure the profile of the ion beam in the position of the sample, a Faraday cup with an orifice of 1 mm was employed. All profile measurements discussed here were measured after the quadrupole electrode potentials had been optimized and the maximum ion current density as shown in Fig. 3.8 (d) was obtained. In each case this cup was moved on a scale of ± 5 mm through the ion beam in two perpendicular, cross-sectional directions. The result of such a measurement for a beam of N^+ ions with an average kinetic energy of 40 eV is illustrated by Fig. 3.9 (a). Although the effective potential derived in the following subsection suggests an ellipticity of the ion beam when leaving the mass-filtering quadrupole segment, there is no significant ellipticity observed, when the ion beam arrives at the surface of the sample. Obviously, the shape of the ion beam is modified when it passes the last quadrupole segment, the ion optics and the region between the quadrupole exit and the sample. For the ion kinetic energy of $E_{kin} = 60$ eV, the measured FWHM of the beam profile in the two perpendicular directions are 12 mm and 11 mm, respectively. The ion beam profile was also measured for an increased ion kinetic energy of 120 eV as shown in Fig. 3.9 (c). In this case, the FWHM for the two cross-sectional directions are 9 mm and 12 mm. This measurement shows that increasing the kinetic energy does not significantly change the ion beam profile, if the quadrupole electrodes are optimized for a maximum ion current density. However, if N_2^+ ions are applied, the ion beam profile may become narrower as can be discerned in Fig. 3.9 (b). Here, the experimentally determined FWHM are 4 mm and 7 mm. For all measured ion beam profiles, it can be concluded, that a homogeneous irradiation of a sample with the maximum achievable ion current density is possible in the range of a few mm. The ion beam for N_2^+ ions can be focused to a larger extent than for N^+ ions. If sample homogeneity on a sample size as used in the frame of this work (1×1 cm²) is required, defocusing might be necessary in this case and a certain loss of ion current density has to be considered.

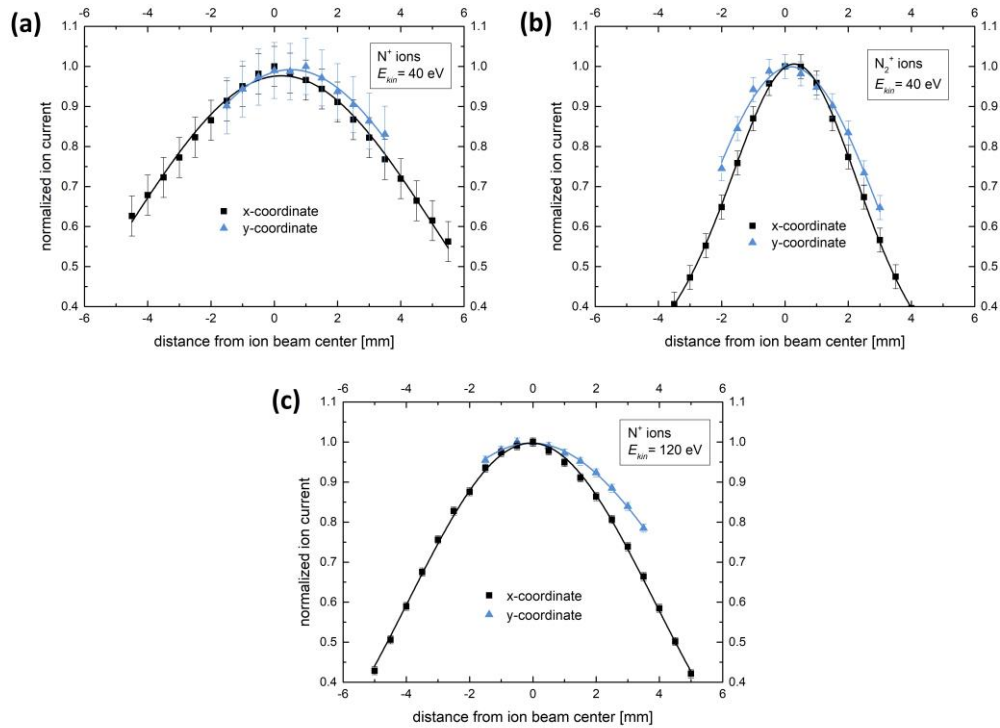


FIG. 3.9: Shapes of the ion beam at a distance of 7.5 cm from the current monitoring grid (14), measured by moving a Faraday cup across the ion beam in two perpendicular directions. Each profile measurement was performed after maximizing the ion current density. Three ion beam profiles are depicted here, each of which was generated under operation of the hollow-anode source. Those are (a) a profile of a N^+ beam with an average kinetic energy of 40 eV, (b) a profile of a N_2^+ beam with an average kinetic energy of 40 eV and (c) a profile of a N^+ beam with an average kinetic energy of 120 eV.

However, according to the previous considerations about the optimum energy window for N_2^+ ions, it can be expected, that a reduction of the ion current density might still yield results comparable to those obtained with N^+ ions. In order to obtain a more complete perception of the ion beam profile, SIMION trajectory simulations were performed. As a first step, the ion trajectories in the first three quadrupole segments (7-9) were simulated, so the conditions, under which the ions enter the ion optics behind the quadrupole segments, can be estimated. For the first simulation the following potentials were chosen: $U_{entry} = 50$ V, $U_{axis} = 0$ V, $U_{exit} = 30$ V and $U_{RF} = 642$ V. The distribution of kinetic energy for the N^+ ions that enter the quadrupole in this simulation was chosen to be Gaussian, centered at 40 eV with a FWHM of 10 eV. Since the background gas might still have an influence on the ion trajectories inside of the quadrupole segments, a hard-sphere model for collisions of ions and molecules from the background gas as offered by SIMION was applied with a mean free path increasing exponentially from 5 cm where the ions enter the first quadrupole segment up to 50 cm, where the ions leave the third quadrupole segment. A trajectory simulation with 10^4 N^+ ions was started, from which 520 reach the end of the third quadrupole segment. Both the lateral, spatial distribution and the angular

3.5 Ion beam characteristics

distribution of those 520 ions that have passed the three quadrupole segments are depicted in Fig. 3.10 as determined by this trajectory simulation. In general, the results from this trajectory simulation have to be treated with caution, because in some cases the properties of the plasma play a major role in the first quadrupole segment which is not included in this simulation. Moreover, the simulation does not take into account space charge effects. When the ions leave the quadrupole the lateral, spatial distribution can appropriately be reproduced by a sum of two Gaussian functions with FWHM of approx. 2.3 mm and 7.5 mm. The angular distribution exhibits a maximum at approx. 30° and ranges up to angles of almost 80° . It is evident from this simulation that when the ions are coupled out of the quadrupole and the RF potential, their angular spread can be large and a certain loss of ions or a spread of the ion beam may be related to the coupling out of the RF potential. A second simulation is conducted to retrace the experimental optimization process and to estimate the shape of the optimized ion beam.

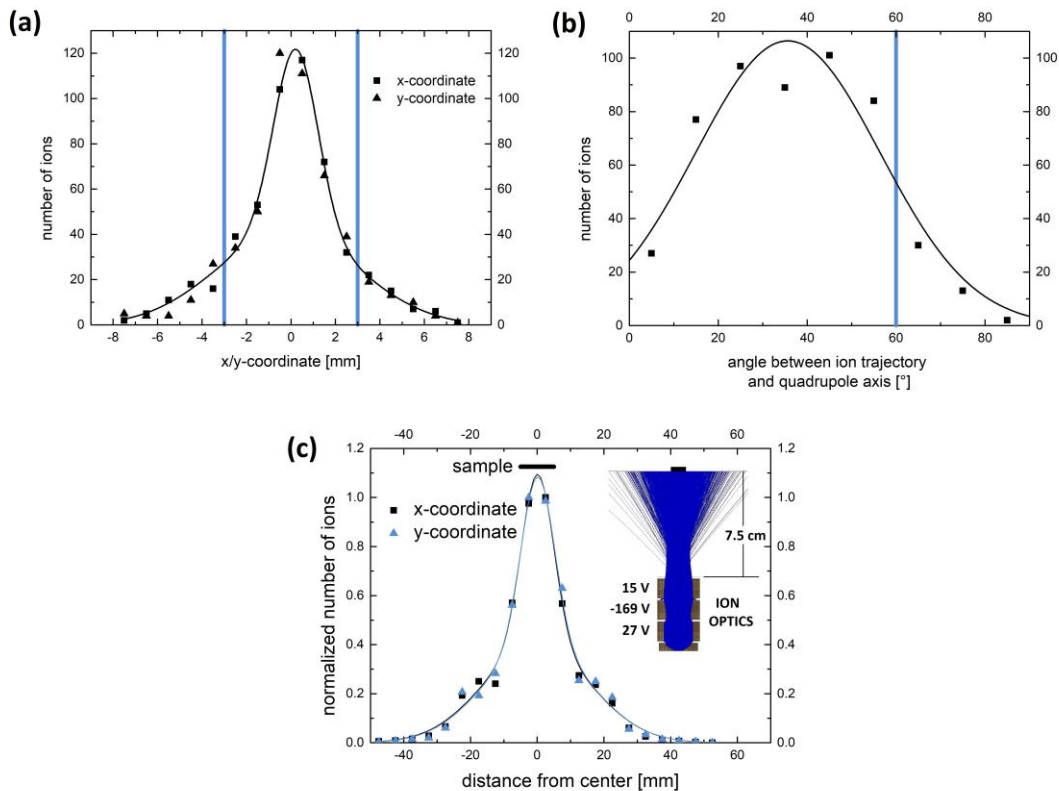


FIG. 3.10: Results with regard to N^+ ion trajectories as simulated with the program package SIMION. The average kinetic energy is 40 eV. First 10^4 trajectories are simulated inside of the three quadrupole segments and (a) the distribution of x- and y-coordinates of ions after passing the three quadrupole segments and (b) the angular distribution of the trajectories of these ions are plotted. The blue lines indicate the assumed starting conditions for a second trajectory simulation of the ion optics only. In this second trajectory simulation, the process of optimizing the potentials applied to the ion optics is simulated. The resulting optimized ion beam profile at the sample position is plotted in (c). The inset in (c) is an illustration of the focused ion beam with the potentials resulting from the optimization process.

For starting this simulation including only the four ring electrodes at the quadrupole exit the kinetic energy distribution of the ions was again chosen to be Gaussian centered at 40 eV with a FWHM of 10 eV. According to the results of the previous simulation the angular distribution was chosen to be uniform with angles up to 60° and the spatial distribution uniform with distances from the quadrupole axis of up to 3 mm. The potential applied to the first exit electrode (10) is $U_{exit} = 30$ V. The other three electrodes (11-13) were subjected to an optimization process. The simulation was run 10^4 times with 10^3 ions each and for each run the potentials for these three electrodes were randomly chosen in an interval between 200 V and -200 V. The optimization yields the combination of potentials, for which the number of ions arriving on a disc centered at the axis of the ion beam, 7.5 cm away from the quadrupole exit and possessing a radius of 2.5 mm, is maximal. This corresponds to the experimental optimization process, where the RFA is employed and the measured ion beam current maximized. The workbench program that was written for this optimization process is added to the appendix. For the potentials received by this optimization the simulation was subsequently executed with 10^4 ions and the x - and y -coordinate of the transmitted ions 7.5 cm away from the quadrupole exit was output. The result of this simulation is presented in Fig. 3.10 (c). The inset shows an image of the resulting, optimized ion beam with the potentials applied to each of the exit electrodes. The resulting potentials are, similar to the potential sequence of the ion optics shown in Fig. 3.2, typical for an Einzel lens. However, due to the broad angular distribution of the ions, when they are coupled out of the RF potential, obtaining an ion beam without divergence is not possible. The main plot in Fig. 3.10 (c) illustrates the shape of the ion beam as it is optimized. There is a narrow contribution with a FWHM of 11 mm and 12 mm for the x - and the y -direction, respectively. These values are in agreement with the measured ion beam profiles on a scale of ± 5 mm (Fig. 3.9 (a)). Furthermore, there also is a broad contribution to the simulated ion beam profile, which can be reproduced by a FWHM of 37 mm and 38 mm, respectively. The occurrence of such a broad component is in agreement with the findings from the distant-dependent ion current measurements in subsection 3.5.1, where a FWHM of the profile of significantly more than 1 cm was determined. Since there is agreement between different measured data and the simulation, it can be concluded, that the simulated beam profile adequately represents the real one and that the divergence, as it is observed, can already be explained by coupling out the ions from the RF potential.

3.6 Considerations about space charge

Since an aim of the modified IBAD setup is to obtain high current densities of ions with relatively low, hyperthermal kinetic energies, space charge effects have to be discussed. It was already observed in the previous subsection, that there is a beam divergence and that the current density decreases when the kinetic energy of the ions

decreases. Both observations might suggest that the ion current density is limited by space charge repulsion [Lan13]. In this subsection the relevance of space charge effects is to be estimated, so that finally it can be concluded, if the ion current density can in principle be increased further and it is to be discussed, what the reasons for the observed limitation of the ion current density are.

3.6.1 Comparison of trapping potential and space charge potential

In subsection 3.1 it was already demonstrated, that the solution of the Mathieu's differential equation can be expressed as harmonic oscillations with the secular frequency $\Omega = 0.5\beta\omega$ as the dominant frequency. Assuming the model of a harmonic oscillation of a mass m , an equivalent spring constant D can be defined as

$$\Omega = \sqrt{\frac{D}{m}}. \quad (3.12)$$

The ion with the mass m oscillates around the axis of the quadrupole, where r is the distance of the ion from the quadrupole axis. Consequently, the effective force on the ion can be expressed as

$$F(r) = -Dr = -\Omega^2 mr = -\frac{1}{4}\beta^2\omega^2 mr. \quad (3.13)$$

The effective trapping potential ϕ_{eff} of the ion inside of the quadrupole segments can be calculated as line integral of the electric field $\frac{F(r)}{ze}$ to

$$\phi_{eff}(r) = -\int_0^r \frac{F(\tilde{r})}{ze} d\tilde{r} = \frac{m\beta^2\omega^2 r^2}{8ze}. \quad (3.14)$$

Depending on the direction (x - or y -direction) the stability parameter a can have a different sign. Therefore, for different directions the values for β and for ϕ_{eff} differ, causing the effective trapping potential to be larger in one and smaller in the other direction. Applying the approximate formula of β (eq. (3.9)) the effective trapping potential can be calculated. For N^+ ions in the center segment of the quadrupole ($U_{DC} = 0.1U_{RF} = 70$ V, see subsection 3.3) the lowest effective trapping potential is approx. $\phi_{eff,1} \cong 50$ V assuming a radial distance of $r = 0.9r_0 \cong 7.9$ mm. For the same ions in the other two quadrupole segments operated in RF only mode the effective trapping potential is $\phi_{eff,2} \cong 130$ V.

The relevance of space charge in the quadrupole segments can be estimated by comparing the above calculated effective trapping potential to the space charge potential of the ion beam. For deriving an expression for the latter [Cha14] a uniform ion beam is presumed, meaning that outside of the ion beam ($r > r_{beam}$) the charge density is $\rho = 0$ and inside of the ion beam ($r \leq r_{beam}$) the charge density is

$$\rho = \frac{I}{v\pi r_{beam}^2}, \quad (3.15)$$

where v is the velocity of the ions and I the total ion beam current. According to the first Maxwell equation the electric field can be obtained by integrating the charge density using cylinder coordinates:

$$E(r) = \frac{1}{\varepsilon_0 r} \int_0^r \rho(\tilde{r}) \tilde{r} d\tilde{r}. \quad (3.16)$$

Executing this integral for inside and outside of the ion beam reveals

$$E(r) = \frac{Ir}{2\pi\varepsilon_0 v r_{beam}^2}, \quad \text{if } r \leq r_{beam}, \quad \text{and} \quad (3.17)$$

$$E(r) = \frac{I}{2\pi\varepsilon_0 v r}, \quad \text{if } r \geq r_{beam}. \quad (3.18)$$

For calculating the resulting space charge potential ϕ_{sp} the line integral of the electric field has to be calculated. For performing this integral, the beam is considered to be within a concentric pipe with a radius $r_p \geq r_{beam}$. Imposing $\phi_{sp}(r_p) = 0$ as boundary condition the result is given by

$$\phi_{sp}(r) = - \int_{r_p}^r E(\tilde{r}) d\tilde{r} = \frac{I}{2\pi\varepsilon_0 v} \ln\left(\frac{r_p}{r}\right) \quad \text{for } r_{beam} \leq r \leq r_p. \quad (3.19)$$

For the space charge potential ϕ_{sp} inside of the ion beam the condition, that ϕ_{sp} is continuous at $r = r_{beam}$, has to be imposed. Then the integral turns into:

$$\phi_{sp}(r) = - \int_0^r E(\tilde{r}) d\tilde{r} = \frac{I}{4\pi\varepsilon_0 v} \left[1 + 2 \ln\left(\frac{r_p}{r_{beam}}\right) - \frac{r^2}{r_{beam}^2} \right] \quad \text{for } r \leq r_{beam}. \quad (3.20)$$

Eq. (3.20) provides an expression, from which the space charge potential can be calculated. Fig. 3.11 depicts the dependence of the total ion current I and the ion kinetic energy E_{kin} on the space charge potential.

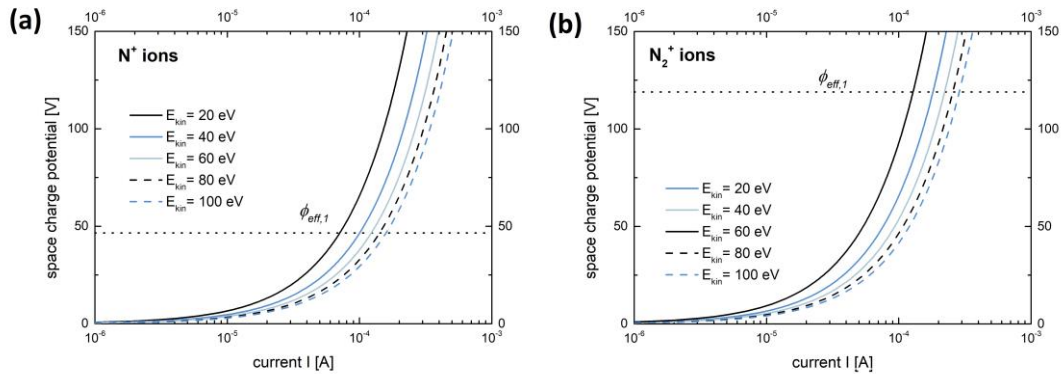


Fig. 3.11: The space charge potential calculated according to eq. (3.20) for (a) N^+ ions and (b) N_2^+ ions. The space charge potential is depicted in dependence of the ion kinetic energy and the ion current. The respective minimum effective trapping potential as calculated according to eq. (3.14) is included in the plots as dotted line.

It is shown that for ion currents $I \sim 100 \mu\text{A}$, the space charge potential reaches the same value as the effective trapping potential. This means that $I \sim 100 \mu\text{A}$ is the maximum ion current which can be trapped inside the quadrupole potential. However the ion currents that were measured here exiting the quadrupole mass filter system are $I \sim 1 \mu\text{A}$, thus significantly smaller (see Fig. 3.8). The comparison of the measured ion currents and the maximum ion current that can be trapped inside the quadrupole potential therefore demonstrates that space charge repulsion is compensated inside of the quadrupole and does not play a role in limiting the achievable ion current density.

3.6.2 Perveance and beam spread

For estimating the relevance of space charge effects in the region between the quadrupole exit and the sample, where space charge is not compensated by a trapping potential, the equation of motion for the ions within an ion beam is formulated [Cha14]. By solving this equation numerically the beam spread can be assessed.

Assuming ions inside of a uniform ion beam, the electric field $E(r)$, as it is expressed in eq. (3.17), can be used. Then, Newton's second law can be written in the following form

$$m \frac{d^2 r}{dt^2} = zeE(r) = \frac{zeI r}{2\pi\epsilon_0 v r_{beam}^2}. \quad (3.21)$$

Since the interest here lies in the beam spread, the derivative in this equation is to be written with respect to the distance along the axis of the beam z , instead of the time t . If the radial velocity $\frac{dr}{dt}$ is small compared to the velocity of the ions v , the velocity component along the beam axis is the most prominent and the beam is called paraxial. Then the derivative in eq. (3.21) can be rewritten

$$\frac{d^2 r}{dt^2} = v^2 \frac{d^2 r}{dz^2}. \quad (3.22)$$

Furthermore, it is common to define the perveance K

$$K = \frac{zeI}{2\pi\epsilon_0 m v^3}. \quad (3.23)$$

With these two modifications the equation of motion becomes

$$\frac{d^2 r}{dz^2} = K \frac{r}{r_{beam}^2}. \quad (3.24)$$

Now, the case of ions on the rim of the ion beam is regarded ($r = r_{beam}$). This way a final equation is deduced, from which the behavior of the radius of the beam in dependence of the distance of travel can be calculated:

$$\frac{d^2 r_{beam}}{dz^2} = K \frac{1}{r_{beam}} \quad (3.25)$$

With the boundary conditions $r_{beam}(0) = 8.75$ mm and $\frac{dr_{beam}}{dz}(0) = 0$ this equation is numerically solved by the Euler method [Neu01]. Under the assumption that the radial position of the charge carriers is equally distributed the current density at the sample position is

$$j = \frac{I}{\pi r_{beam}^2(z=7.5 \text{ cm})}. \quad (3.26)$$

The ion current density j depends on the total ion beam current I . If it is plotted for a certain ion species and kinetic energy in dependence of the total ion beam current as shown in Fig. 3.12 (a), initially the ion current density increases due to the increase of ion current. Eventually, the ion current density decreases, because broadening of the ion beam due to space charge repulsion becomes significant. This illustrates, that for each ion kinetic energy there exists a total ion beam current, for which the ion current density at the sample position is maximal. If the kinetic energy is increased, this maximum shifts to the top right of the graph. This means, that the maximum achievable ion current density increases and if the current density is maximal, the total ion beam current is larger, too. The total ion currents for these maximum ion current densities are calculated to be of the order of 1...10 μA , which is in agreement with the measured exiting ion currents as depicted in Fig. 3.8 (b). The maximal ion current density as is plotted in dependence of the kinetic energy in Fig. 3.12 (b). The python code used to obtain these curves is added to the appendix. For N_2^+ ions the maximum achievable ion current density is smaller by a factor of $\sqrt{2}$, since the perveance is proportional to \sqrt{m} for constant kinetic energy. The calculated and the measured curves (Fig. 3.8 (d)) are in agreement with respect to the general trend, i.e. maximum ion current density increases with increasing kinetic energy. For a kinetic energy of 100 eV the calculated maximum ion current densities are on the order of 1 $\mu\text{A cm}^{-2}$.

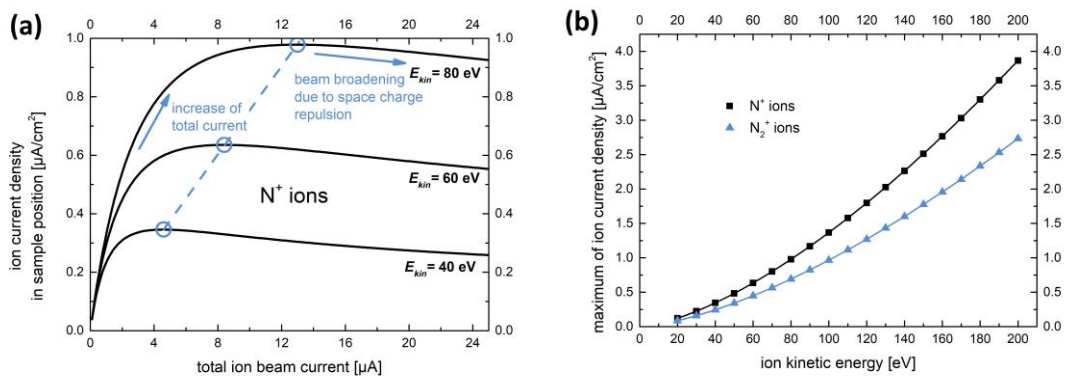


FIG. 3.12: (a) The ion current density calculated as described in the text in dependence of the total ion beam current for N^+ ions with a kinetic energy of 40 eV, 60 eV and 80 eV. (b) The maximum of the calculated ion current density that can be obtained for nitrogen ions with a certain energy varying the total beam current is plotted in dependence of the kinetic energy.

For the same kinetic energy the measured maximum ion current densities are approx. $1 \mu\text{A cm}^{-2}$ and twice as much if the Kaufman ion source is applied. The measured and calculated maximum ion current densities are on the same order of magnitude. Using the Kaufman ion source, even larger values than those calculated could be measured. In conclusion, it is suggested that space charge effects in the region between the quadrupole exit and the sample position might limit the achievable ion current density, since the calculated values for this quantity involving space charge repulsion and the measured data are in agreement. However, it has to be noted, that several assumptions were made for the calculations that are not necessarily fulfilled. Particularly, the present ion beam is not homogeneous which might cause inaccuracies.

3.7 Summary

A custom built quadrupole mass filter system was implemented in an experimental setup for IBA-MBE. Fig. 3.13 contains two photographs of this quadrupole mass filter attached to the IBA-MBE vacuum chamber. In the beginning of this section, five requirements for a proper operation of an ion mass filter in such a context were formulated. Here, the quadrupole mass filter and the generated ion beams were described and characterized with respect to these requirements. The summarized results are:

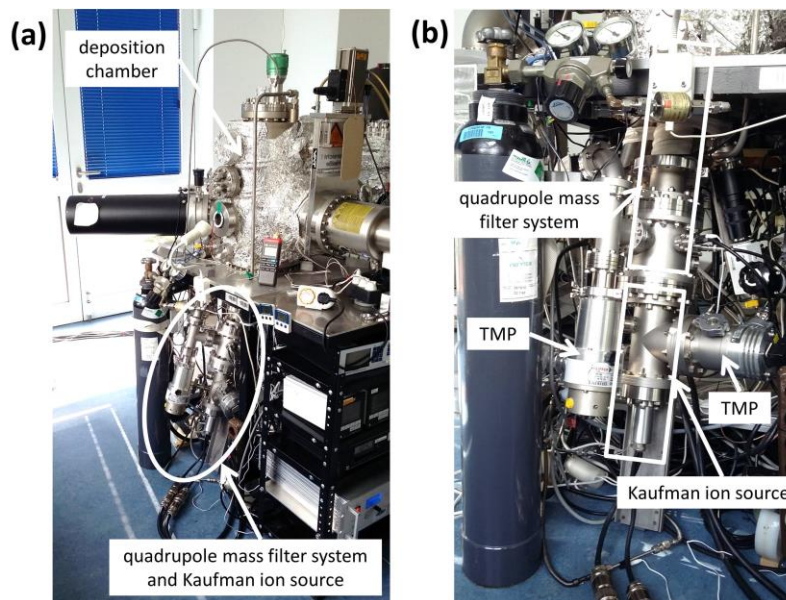


FIG. 3.13: Two photographs of the IBA-MBE vacuum system with the Kaufman ion source and the quadrupole mass filter system attached. In the photograph in (a), the deposition chamber is visible with the cryogenic pump protruding to the right and the RHEED screen to the left. The ions are generated below the deposition chamber. In (b) a photograph from below the deposition chamber is visible. The flanges of the Kaufman source and of the quadrupole mass filter system can be seen. Two turbomolecular pumps (TMP) are attached to these flanges.

- 1) The size of the quadrupole system and the Kaufman ion source together is less than 1 m in length. Therefore, the spatial limitation, which might occur in the laboratory, does not play any role. As opposed to typical beamline setups using an ion accelerator together with a deflection magnet for mass separation and an ion deceleration stage, the setup presented here is rather compact and lightweight.
- 2) The transmission of the quadrupole can be optimized using a stack of electrodes to couple the ions into the RF potential of the quadrupole. Simultaneously a second stack of electrodes couples the ions out of the RF potential. The transmissions are of the order of 0.1 %. There is a maximum achievable ion current density at the sample position, which increases with increasing kinetic ion energy. This ion current density in general is of the order of $j \sim 1 \mu\text{A cm}^{-2}$, which theoretically results in reasonable nitride film deposition rates.
- 3) It is also demonstrated, that the kinetic energy of the ions can be controlled within the relevant range of hyperthermal energies. The FWHM of the energy distributions is typically less than 20 eV, which shows that the kinetic energy is sufficiently well-defined. For small hyperthermal kinetic energies (e.g. 60 eV), the obtainable ion current densities are $I \approx 1 \mu\text{A cm}^{-2}$ or $I \approx 2 \mu\text{A cm}^{-2}$ depending on the applied ion source. The reason for the limitation of the ion current densities is assumed to be space charge repulsion as indicated by respective calculations. However, the efficiency of coupling ions out of the RF potential might also play a major role in the limitation of the ion current density as suggested by ion trajectory simulations.
- 4) The experimental behavior of the quadrupole system in terms of mass filtering is in agreement with the theory. It is shown that ion beams consisting of only N^+ ions or of only N_2^+ ions can be generated by choosing an appropriate combination of RF amplitude and DC potential. The obtainable ion current density is similar for both ion species. Also the requirements with respect to the kinetic ion energy are fulfilled for both ion species.
- 5) The shape of ion beams with maximized ion current densities is found to have two contributions. The narrower contribution has a FWHM, which is as large as the substrates to be used. A homogeneous deposition is achievable on length scales of several mm.

Table 3.1 compares the obtained results with different ion source devices or beamline particle accelerators that were reported about in literature to generate hyperthermal ion beams. In terms of kinetic ion energy distribution the implemented setup exhibits a slightly larger energy width compared to different other devices. However, particularly with regard to the obtainable ion current density, the quadrupole mass filter system in combination with e.g. the Kaufman ion source, yields comparably good results.

3.7 Summary

Table 3.1: Comparison of obtained energy resolution, ion current densities and beam widths in four different facilities. Apart from the results presented in this work, the results from Mach *et al.* [Mac11, Mac14] (this source does not generate a mass selected ion beam) and from Cooper and coworkers [Adl88, Pom02] are listed. Furthermore, results that were obtained using instruments located in Göttingen, Germany [Uhr05, Hab98] and Pohang, South Korea [Cho90] are included.

Facility	Energy resolution	Ion current density	Typical width of ion beam
this work (IOM Leipzig)	≤ 20 eV for N^+ and N_2^+ ions	$2 \mu A cm^{-2}$ for $E_{kin} = 60$ eV	1 cm
Brno University, Czech Republic	6 eV for N ions with $E_{kin} \approx 100$ eV	$1 \mu A cm^{-2}$	2 cm
Cornell University, USA	< 0.5 eV for Ar^+ ions with $E_{kin} = 25$ eV	$< 0.1 \mu A cm^{-2}$ for Ar^+ ions	< 1 cm
	10 eV for ions with $E_{kin} = 100$ eV	$6 \mu A cm^{-2}$ for Cu ions	5 mm
Universität Göttingen, Germany	2 eV	up to $50 \mu A cm^{-2}$	1 cm
Pohang Institute of Science and Technology, South Korea	2 eV for N ions with $E_{kin} \approx 100$ eV	$\sim 2 \mu A cm^{-2}$ for Ar^+ with $E_{kin} = 60$ eV	< 1 cm

At Universität Göttingen as well as at Cornell University ion mass filters are operated at high energies (e.g. 2 keV) and the ions are decelerated in the immediate vicinity of the substrate (e.g. in a distance of 1 cm). Obviously, this way even larger ion current densities can be obtained. Note that such accelerators are mostly used for ion irradiation, ion implantation or ion beam deposition purposes. IBAD however requires at least a second material flux to arrive on the sample, which would be hindered by decelerating grids in the vicinity of the sample.

Concluding this chapter, it is found that the experimental setup fulfills the requirements for performing ion energy and mass selected deposition of nitride thin films to a satisfactory extent. Furthermore, if compared to earlier reported instrumentation, the performance particularly in terms of ion current density is appropriate. Therefore, in a next step, results from thin films that were deposited by means of this experimental setup will be presented.

4. Experimental Methods

After the characterization of the custom quadrupole mass filter system and the generated nitrogen ion beam demonstrated that thin film deposition is expected to be feasible, the next step is to verify the feasibility in real deposition experiments. For such deposition experiments, a vacuum system designed for ion-beam assisted molecular beam epitaxy (IBA-MBE) of nitride thin films is employed. In this section this vacuum chamber is described and relevant details about the two applied ion sources are provided. In order to evaluate the feasibility of ion energy and mass selected IBAD, several methods for thin film characterization are required. The basics and some experimental details of the used analysis techniques are subsequently given in this section.

4.1 System for ion-beam assisted molecular beam epitaxy

4.1.1 Ultra-high vacuum (UHV) system

In the frame of this work, IBA-MBE is carried out using an ultra-high vacuum (UHV) system as it is described by Neumann *et al.* [Neu12]. Fig. 4.1 is a sketch of this system. For introducing samples into or exporting from the UHV system, there is a load-lock chamber. Mounting the samples on a magnetically coupled transfer rod enables the transfer of samples between the three different vacuum chambers.

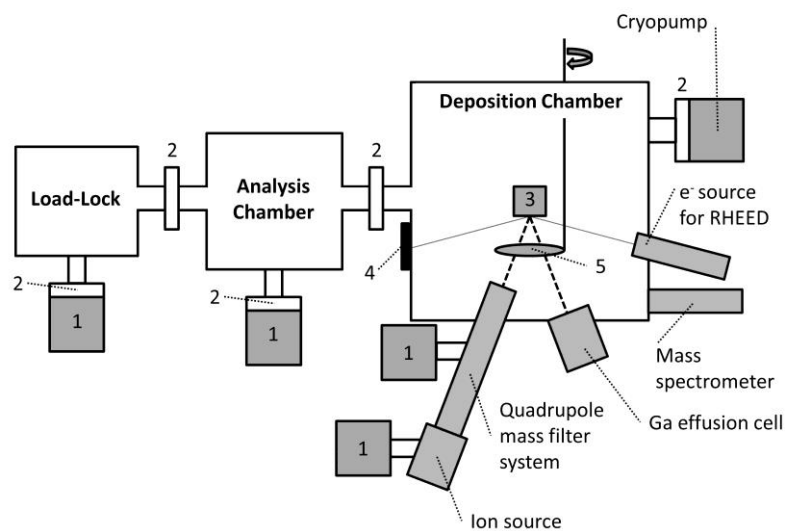


FIG. 4.1: A scheme of the UHV system for IBA-MBE. This system contains the load-lock, the analysis chamber and the deposition chamber. The objects labelled are: 1) turbomolecular pumps, 2) valves, 3) substrate manipulator, 4) fluorescent screen for observing RHEED patterns and 5) a rotatable shutter.

The second vacuum chamber is the analysis chamber. This chamber is equipped with a system for measuring Auger electron spectra (AES). Thus, information about the near-surface composition of the deposited material can be obtained *in vacuo*. The third vacuum chamber is the deposition chamber. On the one hand, a Ga effusion cell (see subsection 4.1.2) is connected to the deposition chamber. On the other hand, an ion source (see subsections 4.1.3 and 4.1.4) equipped with the custom quadrupole mass filter system (see section 3) is connected to the deposition chamber. Both the ion source and the quadrupole mass filter system are pumped by a turbo-molecular pump each, to maintain a pressure as low as possible during a film deposition process. All four turbo-molecular pumps labelled with 1 in Fig. 4.1 are connected to the same fore-vacuum. The pressure in this fore-vacuum is typically of the order of several Pa, when an ion source is operated. The ion beam leaving the quadrupole system and the beam of evaporated Ga are directed to a substrate manipulator. If mounted on this manipulator the substrate can not only be translated in two perpendicular directions, but also rotated around the substrate normal. A Ta wire, which is placed below the substrate, allows for heating the substrate, while a thermocouple close to the substrate and a proportional-integral-derivative controller facilitate the controllability of the substrate temperature. Moreover, the manipulator can be rotated, such that instead of the substrate, different devices to measure ion beam currents can be brought into the relevant position. Among those are the RFA enabling measurements of the kinetic energy, and four single Faraday cups with a small orifice each (diameter 1 mm), which are e.g. suitable for measurements of the ion beam profile. For interrupting the exposure of the substrate to the ion beam and the Ga flux, there is a shutter, which can be moved in front of the sample. The distance between the substrate and the ion source is approx. 63 cm. Assuming a point-like ion source and a substrate with the size of 1 cm, the opening angle can be determined to be 0.9° . Equivalently, the solid angle can be approximated to be $2 \cdot 10^{-4}$ steradian. It is known that neutral, excited N species may contribute to the growth of GaN [Kik06], which is not desired in the frame of this work. However, with the solid angle being that small, a possible contribution of such particles to the growth is assumed not to be significant. A cryogenic pump is employed to maintain a low base pressure, which is beneficial e.g. with respect to the cleanliness of the deposition process. For monitoring the cleanliness and the quality of the vacuum not only a hot-cathode ionization gauge, but also a quadrupole mass spectrometer is implemented in the deposition chamber. It is useful to observe the crystalline structure of the sample *in situ*. For this purpose, a high-energy electron beam is directed on the sample under a small angle of incidence and the reflected electron beam can be observed on a fluorescent screen. By this means reflection high-energy electron diffraction (RHEED) measurements can be performed. The electron source for the RHEED measurements is additionally pumped by a turbo-molecular pump with a separate fore-vacuum.

4.1.2 Effusion cell

The Ga effusion cell (Knudsen cell) mainly consists of a crucible made from boron nitride. This crucible is filled with Ga. The flux of Ga particles can be controlled by the temperature of the effusion cell. A shutter above the effusion cell is used to start or stop the exposure of the substrate to the evaporated Ga.

After the implementation of the quadrupole mass filter system in the UHV system, the required Ga flux for ion-to-atom ratios near unity were in a region of $\Phi_{Ga} < 5 \cdot 10^{13} \text{ cm}^{-2}\text{s}^{-1}$. The previously performed calibrations of the effusion cell (see e.g. [Ger00, Neu13]), however, were for larger ϕ_{Ga} . Therefore, new calibrations were necessary. The procedure for such calibrations is described by Schwertberger [Sch99]: Ni films of a certain film thickness (here: 20 nm) are deposited on a substrate (here: Al_2O_3). This can for example be done by magnetron sputtering. Thereafter, Ga is evaporated onto these films employing different durations and effusion cell temperatures. The evaporated Ga diffuses into the Ni film and is bound there, such that afterwards the amount of Ga which has arrived in certain periods of time on the substrate by employing different effusion cell temperatures can be determined by Rutherford backscattering spectroscopy. The reason for this rather complicated procedure is that the melting point of Ga is near room temperature and that liquid Ga forms tiny droplets on surfaces due to weak wetting. Thus, homogeneous films consisting of pure Ga are not very practicable, but Ga alloy formation, e.g. with Ni in order to form a homogeneous film is possible. Here, for the calibration of the effusion cell, seven different samples were produced. The determined Ga flux for these samples is depicted in Fig. 4.2 in dependence of the effusion cell temperature.

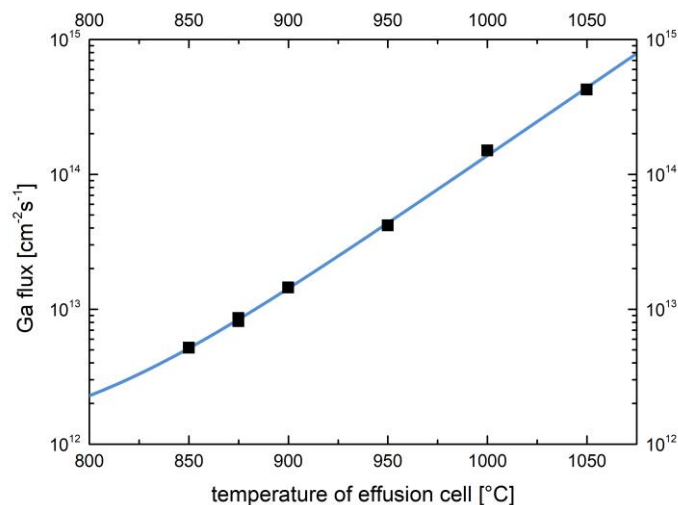


FIG. 4.2: The Ga flux at the sample position in dependence of the temperature of the Ga effusion cell as determined by measuring the number of Ga atoms deposited in a certain time interval by Rutherford Backscattering Spectroscopy. The blue line represents the fit function.

4.1 System for ion-beam assisted molecular beam epitaxy

The fit function here is:

$$\Phi_{Ga}(T_{ec}) = \Phi_0 + ae^{bT_{ec}}, \quad (4.1)$$

with $\phi_0 = (10.0 \pm 6.0) \cdot 10^{11} \text{ cm}^{-2}\text{s}^{-1}$, $a = (10.3 \pm 6.8) \cdot 10^3 \text{ cm}^{-2}\text{s}^{-1}$ and $b = (233 \pm 7) \cdot 10^{-4} (\text{°C})^{-1}$. In the following this fit function is used for determining the Ga flux ϕ_{Ga} for a given effusion cell temperature T_{ec} .

4.1.3 Constricted glow-discharge plasma source

One of the two available source devices for the generation of the nitrogen ion beam in the frame of this work is a constricted glow-discharge plasma beam source, which is also called hollow-anode source. Details about this device were presented by Anders *et al.* [And96]. Fig. 4.3 (a) schematically depicts the way, in which this plasma source is constructed. Nitrogen gas is introduced into a hollow cylinder, which has an inner diameter of 2.8 cm and is made from metal, e.g. stainless steel. A DC potential in the range of $-800 \text{ V} < U_{source} < -600 \text{ V}$ is applied to the source. Taking into account a load resistor put in series with the source, approximately $0.5 \cdot U_{source}$ is the voltage, which is effectively applied to this cylinder, representing the cathode.

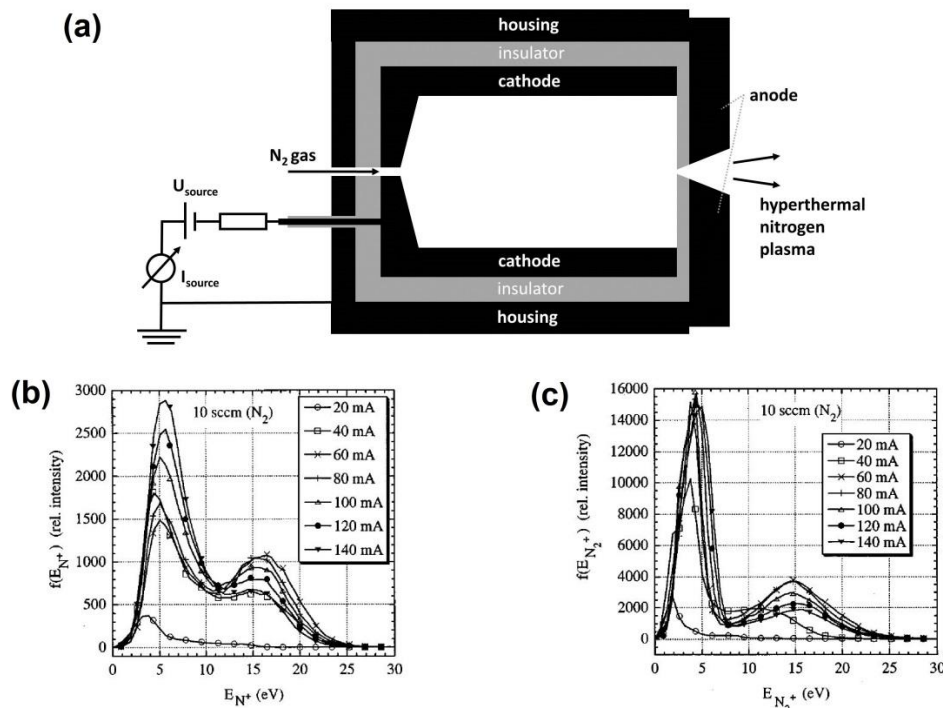


FIG. 4.3: (a) A sketch of the constricted glow-discharge plasma beam source. (b) and (c) are plots of the distribution of kinetic energy of N^+ and N_2^+ ions for different discharge currents I_{source} and a nitrogen mass flow into the plasma source of 10 sccm, respectively ($1 \text{ sccm} \triangleq 2.27 \cdot 10^3 \text{ molecules/s}$) [And98].

When nitrogen gas flows into the cathode and the voltage is applied, a nitrogen gas discharge takes place within the cathode and a discharge current of typically $I_{source} = 50$ mA is measured. The inside of the cathode is covered by a Ta sheet to avoid sputtering of the steel cathode and thereby contamination of the plasma and coating of the AlN ceramic between anode and cathode. The cathode is electrically insulated with respect to the water-cooled housing of the plasma source and the anode. A pressure gradient forms near a small orifice in the anode and the ceramic separating anode and cathode. This gradient accelerates the plasma and by this a directed plasma beam is produced. In Fig. 4.3 (b) and (c) it becomes evident, that N^+ ions as well as N_2^+ ions are generated. The ratio of the ion current of atomic ions N^+ and molecular ions N_2^+ has a value of approximately 1/4, for the used operating conditions. The distributions of the kinetic energy for N^+ and N_2^+ ions, as measured with an energy dispersive mass spectrometer (plasma monitor), are similar. Both reveal two maxima each at approximately 5 eV and 15 eV and for both ion species the kinetic energy does not exceed 25 eV.

4.1.4 Kaufman ion source

For the purpose of IBAD, broad-beam ion sources of the Kaufman-type are frequently applied, when kinetic ion energies smaller than some keV are required [Ens92]. Therefore, as an alternative to the previously described hollow-anode source, a commercially available Kaufman ion source is applicable also in the presented setup. In this case the 'KDC 10' distributed by Kaufman & Robinson Inc. is appropriate due to its simplicity and extremely compact size. The schematic setup of this type of ion source is depicted in Fig. 4.4. The N_2 gas is introduced into a hollow cylinder through a mass flow controller. This hollow cylinder is the anode, while the cathode is a W wire with a diameter of 0.25 mm. This wire is subjected to an alternating current $I_{cathode} \sim 7$ A. Due to this current, electrons are emitted thermionically from the cathode. The discharge voltage between the cathode and the anode, which is typically $U_{discharge} = 50$ V, accelerates the emitted electrons. Simultaneously, the field of a permanent magnet confines the emitted electrons inside of a region within the discharge chamber. Thus, the N_2 molecules in this region can efficiently be ionized by electron impact. For the extraction of the ions from the generated plasma, a two-grid-system, both made of graphite, is mounted on top of the discharge chamber. The first grid is the 'screen grid'. This is conductively connected with the discharge chamber. In each hole of this screen grid, a plasma meniscus forms. The second grid is the 'acceleration grid', which is on a negative potential in order to prevent electron backstreaming and to accelerate the ions away from the plasma meniscus. Both the anode and the cathode are on a positive potential with respect to ground. This potential U_{beam} defines the kinetic energy that the ions have, when they hit a grounded target. In a typical operation mode I_{beam} , which is the current flowing from the ground to the discharge chamber, is automatically kept constant by varying

4.1 System for ion-beam assisted molecular beam epitaxy

$I_{cathode}$. This operation mode ensures a constant ion beam current. The value of I_{beam} is usually $2.5 \text{ mA} < I_{beam} < 4.5 \text{ mA}$.

In comparison to the hollow-anode source described in subsection 3.1.3 the following differences are to be noted:

- 1) The cause of the initial discharge is different: Inside of the cathode of the hollow-anode source particles are ionized as soon as the potential is applied. In the Kaufman ion source, however, electrons are emitted from the cathode and ionization is induced by electron-molecule collisions.
- 2) The Kaufman-type ion source emits an actual ion beam, instead of a plasma. This is beneficial, because the ion current entering the quadrupole can easily be measured and controlled by the source parameters (e.g. by U_{acc} and $I_{cathode}$). However, an ion beam also implies, that space charge effects already between the extraction grids of the ion source limit the achievable ion current density, particularly for small kinetic energies.
- 3) The kinetic energy of ions from a Kaufman ion source is easily controllable by the beam potential U_{beam} , while for the hollow-anode source the distribution of kinetic energy is rather fixed and defined by the properties of the plasma as well as the pressure gradient at the orifice.
- 4) The hollow-anode source does not contain any filaments. Even though certain ceramic parts of this source have to be cleaned on a regular basis, the maintenance is less time-consuming.
- 5) Since the Kaufman ion source automatically keeps the beam current constant, an ion beam with a stable current can be obtained without long warm-up times.

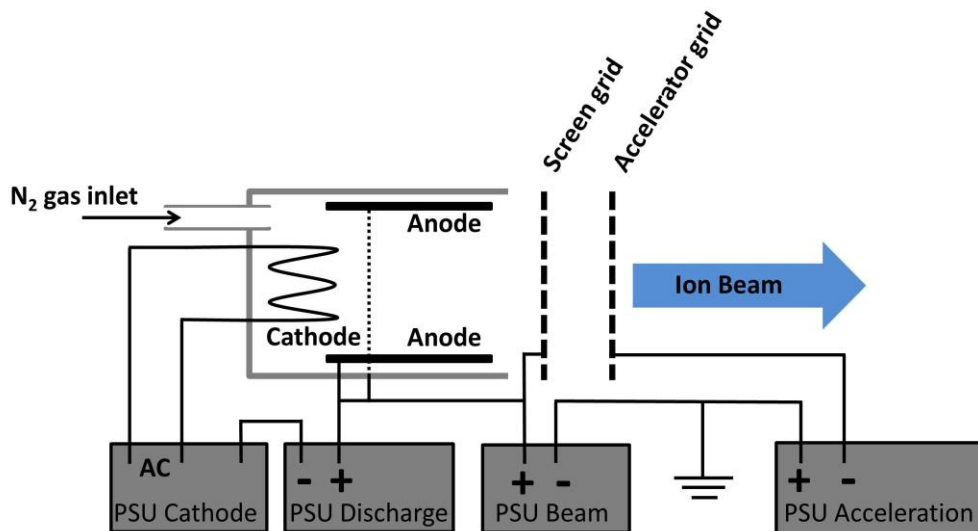


FIG. 4.4: A sketch of the Kaufman ion source including the cathode for the electron emission, the grid system for the extraction of the ions from the plasma inside of the discharge chamber and all the power supply units (PSU) that are necessary for the operation of this source.

4.2 Crystalline structure and texture

4.2.1 X-ray based methods

X-rays are electromagnetic radiation with a wavelength of the order of $\lambda \sim 0.1 \text{ nm}$. The spacing d_{hkl} of planes in crystal lattices is on the same order of magnitude. Hence, from elastic x-ray diffraction spectra, which can be measured non-destructively, information about the crystal lattice can be obtained. Depending on the angle of incidence, XRD may yield information averaged over the whole thickness of a thin film (up to several μm , depending on the material) or only over a volume close to the surface. If structural properties of a solid material are to be investigated thoroughly, it is indispensable to consider experimental methods based on XRD. General information about x-ray radiation, the experimental methods based on its diffraction and the analytical possibilities that they offer can e.g. be found in text books like [Cul01] or [Bir06]. For understanding XRD, the Bragg condition is of importance. X-rays are reflected by different lattice planes characterized by the Miller indices h, k, l . As visible in Fig. 4.5, there is a path difference Δs for x-rays reflected from different lattice planes depending on the lattice spacing d_{hkl} . If this path difference is an integer multiple of the wavelength, there is constructive interference. This is specified by the Bragg condition: An intensity maximum of the n -th order in the diffraction pattern occurs, if the following for the angle θ between the incident x-ray and the respective lattice plane (correspondingly between the diffracted x-ray and the respective lattice plane) is fulfilled

$$2d_{hkl} \sin(\theta) = n\lambda \quad (4.2)$$

In this thesis, a Rigaku Ultima IV Type 3 diffractometer is employed. Here, the x-ray radiation is generated by means of an x-ray tube, which contains a W cathode and a Cu anode. Electrons are emitted by the cathode and accelerated up to a kinetic energy of 40 keV towards the Cu anode. While the electrons are decelerated within the anode, x-ray radiation with distinct wavelengths is emitted.

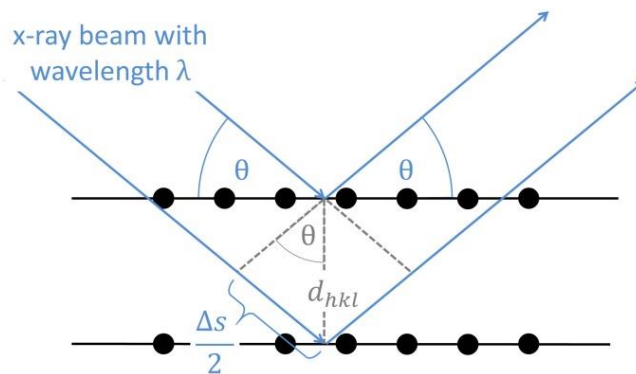


FIG. 4.5: Sketch of the reflection of x-rays of wavelength λ from lattice planes with the Miller indices h, k and l .

The characteristic wavelength, which is to be exploited for the measurements, is $\lambda = 0.15418 \text{ nm}$, which corresponds to a degenerate transition with $\text{Cu K}_{\alpha,1}$ and $\text{Cu K}_{\alpha,2}$ possessing wavelengths differing from each other by less than 1 pm. Further, x-rays with wavelengths corresponding to the Cu K_{β} transition as well as the W L_{α} transitions are emitted by the x-ray tube, where the W L_{α} contribution originates from W contaminations of the anode, which develop after a certain lifetime of the tube. Additionally, a broad background of Bremsstrahlung is generated by the x-ray tube.

Fig. 4.6 depicts the setup of the diffractometer. It possesses the following degrees of freedom:

- 1) The x-ray tube can be moved in a plane perpendicular to the sample.
- 2) The x-ray detector can independently be moved in a plane perpendicular to the sample surface.
- 3) The sample can be rotated around its surface normal. This rotation is characterized by the azimuthal angle φ .
- 4) The x-ray detector can additionally be moved in directions parallel to the sample surface. This movement is characterized by the in-plane angle $2\theta_{\chi}$.

All these movements are performed, while the distance between the x-ray tube and the sample surface as well as between the sample surface and the x-ray detector remains constant. Therefore, the intensities of different reflections in any spectrum are comparable to each other and reflect properties of the sample. In the following, some of the possible measurements are introduced, which can be executed using this diffractometer and which are relevant for this thesis:

In a $2\theta/\omega$ measurement, both ω and 2θ (as defined in Fig. 4.6 (a)) are varied, where the movement in 2θ is two times faster than the movement in ω . Here, only reflections from lattice planes being parallel to the sample surface contribute to the emerging intensity maxima in a corresponding XRD spectrum.

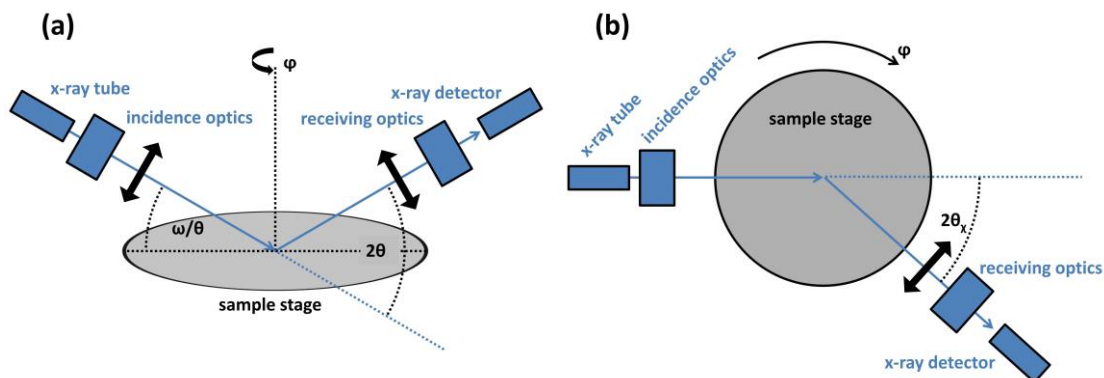


FIG. 4.6 Illustration of the geometry and the degrees of freedom of the x-ray diffractometer applied here. In (a) a side-view on the sample stage is depicted so that the relevant angles for out-of-plane measurements can be discerned, while in (b) a top-view is depicted so that the relevant angles for in-plane measurements can be discerned.

However, if the crystallites are randomly oriented as it is the case in polycrystalline films, reflections from different families of lattice planes are observable depending only on the respective structure factors. By regarding the position, the intensity and the width of Bragg reflections in a $2\theta/\omega$ measurement, information about the lattice parameters, the lattice structure, the (preferred) orientation and the size of crystallites can be obtained.

In particular for textured or epitaxial samples, rocking curves (ω scans) can be measured. In the beginning, ω and 2θ are adjusted for a specific reflection from lattice planes parallel to the sample surface. Subsequently, the angle ω is varied in a narrow angular region around the previously set value of ω , while the angle 2θ is kept constant. The width of rocking curves yields information about the tilt of crystallites with respect to a certain axis, which lies within the sample surface.

A more comprehensive knowledge about the distribution of orientations of crystallites in a textured or epitaxial sample can be gained by applying x-ray texture goniometry, i.e. by measuring pole figures of the samples. For an in-plane pole figure measurement (making use of the in-plane degree of freedom of the detector arm), a reflection from a certain family of lattice planes, quantified by d_{hkl} or 2θ , respectively, is chosen. By varying ω , 2θ and $2\theta_\chi$, the x-ray tube and the x-ray detector are moved, such that the Bragg condition would be fulfilled for the chosen lattice planes, if they were tilted by an angle α with respect to the surface normal. For each value of α , the sample is rotated by 360° (φ scan) and the diffracted intensity is recorded. The in-plane pole figure, therefore, consists of intensity values recorded for values $0^\circ \leq \alpha \leq 90^\circ$ and for values $0^\circ \leq \varphi < 360^\circ$. The results are typically depicted in a stereographic projection. For epitaxial or textured samples, an in-plane pole figure measurement reveals, in what directions the previously chosen Bragg reflection occurs. Hence, in-plane pole figure measurements are a tool to determine crystal orientations and epitaxial relationships.

A $2\theta_\chi/\varphi$ measurement belongs to the in-plane measurements, too. Here, ω is adjusted to grazing incidence, i.e. near the critical angle for total external reflection (usually $\omega < 1^\circ$). 2θ is adjusted accordingly (usually $2\theta < 2^\circ$). The grazing incidence condition and the in-plane arm ($2\theta_\chi$) of the diffractometer enable the investigation of Bragg reflections corresponding to lattice planes, which are perpendicular to the sample surface. In a $2\theta_\chi/\varphi$ measurement, both $2\theta_\chi$ and φ are varied. Hence, it is the in-plane analogue of the (out-of-plane) $2\theta/\omega$ measurement. Note, that the initial value of the angle φ is relevant, because it defines, the exact orientation, of the lattice planes perpendicular to the sample surface that can be investigated by such a measurement.

The in-plane φ measurement is the analogue of the (out-of-plane) rocking curve. First, ω and 2θ are adjusted for grazing incidence. Second, θ_χ and φ are adjusted for a Bragg reflection corresponding to lattice planes perpendicular to the sample surface.

Consequently, the width of a peak in a φ scan is a measure for the twist of crystallites with respect to the surface normal.

The diffractometer includes x-ray optics, which are adjusted for the respective kind of measurement, which is to be performed. The incident x-ray from the tube passes first a graded parabolic multilayer mirror, which reduces the vertical divergence of the beam so that a parallel beam results, second a parallel slit collimator, which reduces the horizontal divergence of the beam and finally a horizontal, incident slit and a height limiting slit, which adjust the spot size to the size of the sample. Typically, the parallel slit collimator reduces the horizontal divergence to 5° . For in-plane measurements (e.g. in-plane φ and $2\theta_\chi/\varphi$ measurements), it is beneficial to use a parallel slit collimator reducing the divergence to a smaller value of ideally 0.5° . After being diffracted by the sample, the x-ray passes the receiving optics. These consist of a scattering slit, a soller slit, a receiving slit, an optional graphite monochromator and an attenuator. For in-plane measurements, the soller slit is implemented vertically; therefore the horizontal angular resolution is improved. This soller slit typically reduces the divergence of the receiving beam to 0.5° . For out-of-plane measurements ($2\theta/\omega$ – and rocking curve measurements), the soller slit is usually demounted and the angular resolution in the vertical direction (typically below 0.1°) is determined by the scattering and the receiving slit. The graphite monochromator can be inserted, in order to reduce the contribution of the Cu K_β and the W L_α transitions to the XRD spectrum and finally the attenuator may reduce the intensity impinging on the detector, in order to avoid overexposure of the scintillation counter.

As an additional x-ray based tool to investigate thin films, independently of the crystalline structure or texture, X-ray reflectivity (XRR) is to be mentioned. The XRR measurement is in principle a $2\theta/\omega$ measurement, for which the sample surface is irradiated under grazing incidence, i.e. the angle of incidence θ is in the vicinity of the critical angle for total external reflection θ_c . Fig. 4.7 depicts an exemplary XRR curve, which was calculated for the reflection of Cu K_α radiation by a GaN thin film with a film thickness of 20 nm grown on Al_2O_3 . When the measurement starts with $\theta < \theta_c$, the x-rays do not penetrate the thin film. When θ exceeds θ_c , a fraction of the x-ray radiation penetrates the thin film and is reflected from subsequent interfaces, if the contrast in mass density is sufficiently large. Consequently, the reflected intensity decreases and the x-rays reflected at the film surface and subsequent interfaces interfere with each other. In the exemplary reflectivity curve, clearly an oscillation of the x-ray intensity occurs due to this interference. This was already observed in the 1930's and is referred to as Kiessig fringes [Kie31]. In the context of this work, the largest benefit from XRR measurements is that the film thickness can be determined from the period of this oscillation. Additionally, the mass density of the thin film can be deduced by determining θ_c and the roughnesses of both the interface and the surface can be deduced by the decay of the intensity and the amplitude of the Kiessig fringes [Yas10].

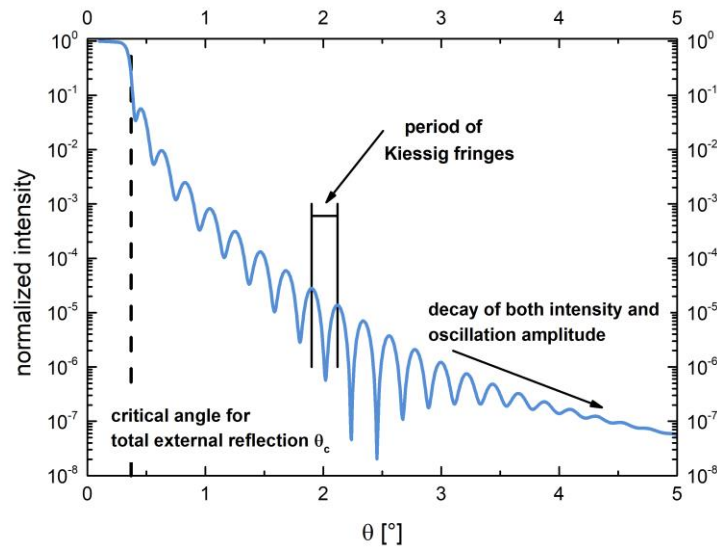


FIG. 4.7: An exemplary XRR curve calculated by the program IMD for a 20 nm thick GaN film grown on a Al_2O_3 substrate.

The XRR measurements were performed using a high-resolution diffractometer ('Seifert XRD 3003 PTS') with similar degrees of freedom compared to the previously described diffractometer, but equipped with a primary two-bounce Ge (220) monochromator. For analyzing XRR measurements with respect to the mentioned quantities both IMD [Win98] and Rayflex [Ray00] are utilized.

4.2.2 Reflection high-energy electron diffraction (RHEED)

Reflection high-energy electron diffraction (RHEED) can be performed to analyze *in situ* the growth mode as well as the surface structure of a thin film. During the growth process the sample is irradiated with electrons with energies in the range of 10 keV up to 30 keV under grazing incidence (The angle between the electron beam and the sample surface is $\sim 2^\circ$). Due to the grazing incidence the penetration depth of the electrons is small, just a few monolayers. Consequently, RHEED is a technique with a high surface sensitivity. The reflected and diffracted electrons from the sample surface are collected on a fluorescent screen. Taking into account relativistic terms, the de Broglie wavelength for electrons is

$$\lambda = \frac{h}{\sqrt{2m_0E + E^2/c^2}}, \quad (4.3)$$

with m_0 , E , h and c being the rest mass and the energy of the electron, the Planck constant and the speed of light, respectively [Bra99]. For electrons with an energy $E = 30$ keV, the de Broglie wavelength is $\lambda \approx 7$ pm. Due to the electrons behaving like a wave with a wavelength in the pm-range, the crystal lattice near the surface of the sample diffracts the electron beam. The condition for constructive interference, i.e.

the occurrence of an intensity maximum can be formulated as Bragg condition (see eq. (4.2)) or equivalently as Laue condition in the reciprocal space:

$$\vec{k}_1 - \vec{k}_0 = \vec{G}. \quad (4.4)$$

Here, \vec{k}_0 is the incident wave vector with $|\vec{k}_0| = 2\pi/\lambda$, \vec{k}_1 is the wave vector of the diffracted electron beam and \vec{G} is a vector between any reciprocal lattice points. If the scattering occurs elastically, the directions of the diffracted electron beams are given by the intersections of the reciprocal lattice with the Ewald sphere. The Ewald sphere has a radius $|\vec{k}_0|$, where \vec{k}_0 is chosen such that it is directed on a reciprocal lattice point. The origin of \vec{k}_0 is the center of the Ewald sphere.

Consequently, from the resulting diffraction pattern, which can be observed on the fluorescent screen, information about the structure of the growing thin film near the surface and also about the growth mode can be obtained [Tan07]: If the sample is polycrystalline, the surface is typically rough. The electrons are transmitted through a multitude of crystal grains with different orientation. The corresponding reciprocal lattice consists of concentric spheres. As a result, the obtained diffraction pattern on the screen consists of concentric rings, the Debye rings. Fig. 4.8 (a) depicts the situation, where a rough surface with epitaxially grown island structures on top is exposed to the electron beam. Here, the reciprocal lattice consists of points in a certain arrangement, depending on the crystal structure and its orientation with respect to the incident electron beam. The diffraction pattern consequently consists of points in a respective arrangement as indicated by Fig. 4.8 (b). As a third case, layer-by-layer growth of epitaxial thin films is to be mentioned. In contrast to the previously described cases, here, the electrons penetrate only very few atomic layers near the surface, such that instead of a transmission pattern, a reflection pattern is obtained. This means, that the reciprocal lattice consists of 1-dimensional crystal truncation rods and the diffraction pattern, ideally of distinct points. The radius of the Ewald sphere in RHEED is comparably large and in reality, imperfections in the crystal lattice near the surface lead to a broadening of the crystal truncation rods in the reciprocal space.

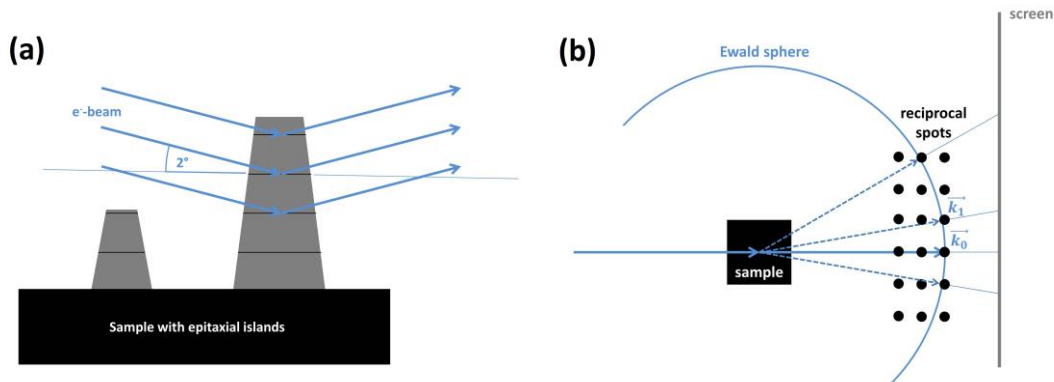


FIG. 4.8: Graphical representations of RHEED. (a) Electron beams are reflected from crystal lattice planes while being transmitted through crystalline island structures (adapted from [Tan07]) (b) A top-view of the reciprocal space (adapted from [Bra99]). The Ewald sphere is sketched here as well as the reciprocal lattice of the crystalline sample.

This usually leads to an elongation of the maxima in the experimental diffraction pattern of the screen. Hence, for layer-by-layer growth typically a diffraction pattern consisting of streaks is observed.

4.2.3 Transmission electron microscopy

Transmission electron microscopy (TEM) is used to investigate the microstructure as well as the defect structure of the deposited thin films. Here, electron energies of > 80 keV are employed yielding even smaller de Broglie wavelengths as described in the previous subsection. Again, due to the small wavelength, diffraction by lattice planes of a crystalline material is possible. Moreover, the small wavelength has a benefit in the context of microscopy, since in optical microscopy the resolution depends on the wavelength of the employed light according to the Abbe criterion [Bor05].

In TEM, a thin specimen is illuminated by a coherent electron beam. While being transmitted through the specimen, some electrons are elastically scattered depending on the local specimen properties, while other electrons are inelastically scattered. Thus, the transmitted electron waves contain information about specimen properties, which influence the scattering behavior of the electrons [Oco92].

The transmitted electrons are focused by an objective lens. The subsequent system of electron optics can either image the backfocal plane or the image plane of the objective lens. By this means, it is possible to detect a pattern of the elastically scattered electrons (diffraction mode) and an image of the specimen in real space (image mode), respectively [Wil09]. For the image mode, an objective aperture is used to select the electron beam, which is to be imaged. The transmitted electron beam itself can be selected and used for imaging. In this case, regions, where less scattering occurs (e.g. holes in a sample), appear bright and regions, where significant scattering occurs, appear dark on the detector (bright-field TEM). If a beamlet consisting only of Bragg-scattered electrons is selected, regions, where less scattering occurs, appear dark and region, where significant scattering occurs, appear bright in the final measurement (dark-field TEM). The contrast appearing in such a TEM measurement is called diffraction or mass-thickness contrast, and can be used to observe regions of different crystallinity, density or composition in a specimen. If for a crystalline specimen high resolution TEM (HRTEM) is to be measured, the objective aperture is adjusted in a way that at least two coherent electron beams are used for imaging (e.g. the transmitted electron beam itself and at least one Bragg-scattered electron beam). Consequently, the observed image is an interference pattern of the different coherent electron beams and the contrast in the image is due to the shifted phase of the electrons (phase-contrast TEM or HRTEM) [Ege07]. Apart from HRTEM, there is also the possibility to perform scanning TEM measurements (STEM). In this case the electron beam is focused on a small spot on the specimen instead of homogeneously

illuminating it; and the final image is composed from a series of measurements in different positions on the specimen. The advantage of STEM is that incoherent scattering, as it occurs from single atoms, can be exploited. Therefore, in STEM the contrast due to a difference in atomic number (z-contrast) is relevant instead of the phase of the electron beam [Wil09]. The STEM measurement presented in this work was measured using an annular dark field detector (ADF-STEM).

For HRTEM and STEM, the spatial resolution not only depends on the wavelength of the electrons, but also on the properties of the implemented lenses in the microscope. Particularly, the spherical aberration of the objective lens has to be taken into account as a resolution-limiting factor. However, the spherical aberration can be decreased and the spatial resolution thereby improved by additional electron optics, which typically involve multipole assemblies. Modern microscopes equipped with such aberration correction systems achieve a spatial resolution below 0.1 nm without decreasing the electron wavelength [Het04, Ina09].

The microscope employed in the frame of this work is a '*FEI Titan G2 60-300*'. Here, electrons are generated from a Schottky-type field-emission source. This microscope comprises a spherical-aberration-correction for the condenser lens system. Using this TEM it is possible to simultaneously resolve heavy and light atoms in compound materials, like e.g. Ga and N atoms in GaN [Lot14].

TEM measurements in general require a sophisticated specimen preparation. A thin TEM lamella that is sufficiently thin for the transmission of electrons with 300 keV, i.e. with a thickness of less than 100 nm, has to be fabricated. The TEM specimens presented as part of this work were prepared by ion beam milling in a 'Zeiss Auriga FIB-SEM Crossbeam System' using a Ga ion beam as well as an Ar ion beam in a separate 'Fischione NanoMill' system. Here, such a preparation process typically consists of the following steps:

- 1) A Pt layer is deposited on the region of interest, in order to avoid surface damage during the subsequent preparation steps, which include high-energy ion milling. For this purpose, a precursor gas is introduced into the vacuum system, the precursor is dissociated, and thereby the Pt is deposited in the respective positions. The dissociation of the Pt precursor and the deposition of the Pt protection layer are performed in two steps. First, an electron beam with a kinetic energy of 2 keV is applied, and second the thickness of the resulting Pt layer is increased by using a Ga ion beam with an applied acceleration voltage of 30 kV. The final thickness of this local Pt layer is typically $1 \mu\text{m} < d_{Pt} < 5 \mu\text{m}$.
- 2) The Ga ion beam with an acceleration voltage of 30 kV is used to cut the region of interest from the specimen as shown in Fig. 4.9 (a). Between the milled trenches, a focused ion beam (FIB) lamella with the Pt layer on top remains. Etching the trenches is executed in several consecutive steps, in

which the ion beam current is gradually decreased down to approx. 1 nA. By the end of this process, a FIB lamella with a Pt layer on top remains between the two trenches. Its thickness after this part of the process typically is $d_{bar} \approx 1.5 \mu\text{m}$.

- 3) The lamella has to be lifted off the sample. For doing so, an 'L-cut' is performed using the Ga ion beam. Fig. 4.9 (a) depicts the situation after such a cut. In the following, a sample manipulator is moved close to the lamella. The manipulator and the lamella are connected by depositing Pt between them. After a final etching step with the Ga ion beam, the lamella can be transferred freely by a sample manipulator.
- 4) The as-cut and freely-movable lamella is then fixed to a TEM grid by again depositing Pt between the grid and the lamella.
- 5) In order to facilitate the transmission of 300 keV electrons, as a last step in specimen preparation, the lamella is to be thinned further. This is done using the Ga ion beam in a few steps with stepwise decreasing ion beam current. Finally, the acceleration voltage for the Ga ion beam is reduced to 5 kV and the thinning process is continued with this low-energy ion beam. After this step, the lamella typically has a thickness of $100 \text{ nm} < d_{thinned \text{ lamella}} < 200 \text{ nm}$. Such a lamella can be seen in Fig. 4.9 (b).
- 6) The thickness of a FIB lamella can be further decreased by using a low-energy (acceleration voltage of several 100 V) Ar ion beam inside a separate 'Fischione NanoMill' system. A further advantage of this additional thinning is the removal of regions in the lamella, which were damaged or even amorphized by the high-energy Ga ion irradiation. The damage induced to the lamella by the low-energy Ar ion irradiation is significantly smaller [Lot15].

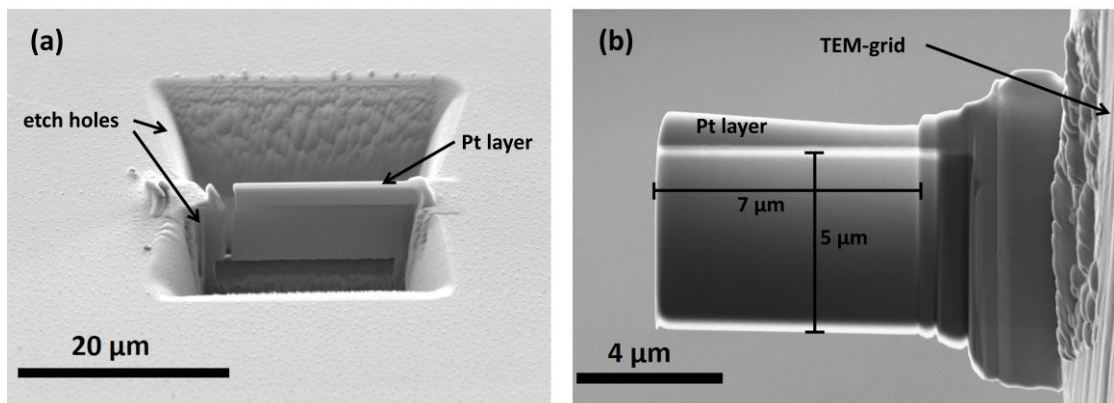


FIG. 4.9: Scanning electron microscopy images taken in different stages of a sample preparation process for TEM measurements: (a) isolation of a lamella from a substrate. An 'L-cut' is performed so that the lamella is only fixed to the sample on the right side. (b) The FIB lamella after transfer from a sample to a TEM-grid. The lamella was further processed using a low-energy Ga ion beam before introducing into the TEM.

4.3 Chemical composition

As mentioned previously, an Auger electron spectrometer (AES) is available for *in vacuo* measurements. Thus, it is possible to obtain information about the chemical composition of produced samples. The fundamental principle of AES is depicted in Fig. 4.10 and described e.g. by Browning [Bro92]. In the beginning, a secondary electron is emitted from a low-energy state E_1 in an atom (see Fig. 4.10 (a)). This emission can be induced by e.g. x-ray or energetic electron irradiation. In the present spectrometer, the sample is irradiated with electrons possessing a kinetic energy of 2.5 keV. The emission of a secondary electron causes a hole in this low-energy state, which is, consequently, filled by an electron from a state with a higher energy E_2 (see Fig. 4.10 (b)). In this process, the electron releases the energy $E_2 - E_1$, which is transferred to an electron in a state of energy E_3 with a specific probability. This is the Auger electron and it is emitted as a consequence (see Fig. 4.10 (c)). Its kinetic energy is $E_{kin} = E_2 - E_1 - W$, where W is the energy that the electron requires to move from the energy state E_3 into the vacuum. For the example of nitrogen, the three electrons in the process might be the 1s, the 2s and the 2p electrons, respectively. Auger electrons are also generated in larger distances from the surface; however, while travelling through the material, they rapidly lose their kinetic energy and cannot arrive on the surface. Therefore, AES is sensitive only to a depth of a few monolayers below the surface. In order to facilitate the distinction of the signal originating from the Auger transition and the background, the Auger electron spectra are typically given as the derivative of the number of measured electrons with respect to the kinetic energy.

Another technique to assess the chemical composition of surfaces is x-ray photoelectron spectroscopy (XPS).

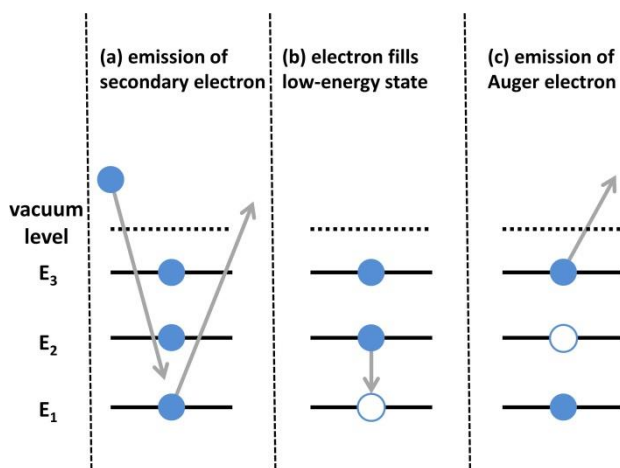


FIG. 4.10 The principle of the emission of Auger electrons in three consecutive steps: (a) An electron from a low-energy state is emitted leaving an empty state, (b) this empty state is occupied by another electron from a state with higher energy and (c) the energy that is available after that is transferred to a third electron of the same shell, which is emitted. This last electron is the Auger electron

Here, the sample is exposed to x-ray radiation. In this context, Al K_α radiation is applied. The x-ray radiation induces the emission of photoelectrons with binding energies E_{pe} . After the photoelectrons were ejected from the atom, they have a kinetic energy

$$E_{kin} = hf - E_{pe}, \quad (4.5)$$

if the spectrometer work function is zero [Oco92]. f is the frequency of the applied x-ray radiation. In order to facilitate the detection of small electron currents, the ejected electrons pass a set of electron optics. After that, their kinetic energy is measured by a concentric hemispherical analyzer in combination with a channel electron multiplier. Knowing the applied radiation frequency, the binding energy can be deduced from the kinetic energy. This binding energy is characteristic for specific energy states in different atoms. The x-ray photoelectron spectra are typically plotted as function of this binding energy E_{pe} . The ejection of Auger electrons is simultaneously induced by the x-ray radiation such that Auger electron transitions typically contribute to the spectrum, too. Note that in contrast to the kinetic energy of the photoelectrons, the kinetic energy of Auger electrons is independent of the applied radiation. Since in an x-ray photoelectron spectrum, the binding energy is plotted instead of the kinetic energy, the position in the spectrum, where the Auger transition appears, depends on the applied radiation.

4.4 Surface topography

For evaluating the surface topography, atomic force microscopy (AFM) is employed. The AFM, as was first reported about in 1986 [Bin86], was used to measure forces between a tip, consisting ideally of only one atom, and a sample surface. Different forces play a role in the interaction between the tip and a surface, among those are attractive forces, e.g. van-der-Waals forces, and repulsive forces, e.g. due to the Pauli principle. The dependence of the distance on the potential energy is typically described as a Lennard-Jones potential [Hau12]. Nowadays, using the distance-dependence of forces, AFM is frequently applied to measure the surface topography. The basic setup of AFM devices used for this purpose is depicted in Fig. 4.11. There are different modes, which can be used to obtain a topography map using AFM. Here, the 'intermittent contact mode' is applied. The cantilever oscillates at a frequency close to its resonance. Without contact to the surface, the oscillation of the cantilever has an amplitude A_0 . When the tip is brought close to a surface, repulsive forces play a more prominent role. Thus, the driven oscillation of the cantilever is damped and the amplitude decreases. While the tip is scanned over a surface in x- and y-direction, the amplitude of the driven cantilever oscillation is continuously measured. A feedback loop ensures that the amplitude remains at a chosen value by correcting the voltage applied to a piezo element controlling the z-position of the cantilever. In every

measured x - and y -position, this voltage is equivalent to the relative height of the surface. In the 'intermittent contact mode', the amplitude of the cantilever oscillation is large compared to different operating modes, i.e. the oscillation ranges from a tip-sample distance, for which the forces are repulsive to a distance, for which there are no forces between tip and sample [Eat10]. Therefore, in contrast to contact modes, where the tip-sample distance is maintained in the region of repulsive forces, here, lateral forces between tip and sample neither have an influence on the measurement nor damage the sample. The scanning in x - and y -direction is performed by additional piezo elements. In order to avoid creep of the piezo elements causing image artifacts, these scanners are operated in closed loop, i.e. the piezo voltage is corrected using position detectors in both x - and y -direction. The cantilevers used here consist of Si and possess an Al coating on their backsides for a better reflectivity. The tips have nominal and maximum radii of 7 nm and 10 nm, respectively, which limits the lateral resolution of the AFM images. Especially, if the surface is smooth and the structures to be visualized are small, often the raw AFM data is dominated by a drift in the z -piezo. In order to remove this effect, the data is levelled after measurement. This is done by fitting each scan line usually by a linear function, and subtracting the fit function from the measured data. Consequently, the average height in an image is $\overline{h_{i,j}} = 0$.

For characterizing the roughness of surfaces as measured by AFM, the root mean square (RMS) of the height is defined as

$$RMS = \sqrt{\frac{1}{MN} \sum_{i=1}^M \sum_{j=1}^N h_{i,j}^2}, \quad (4.6)$$

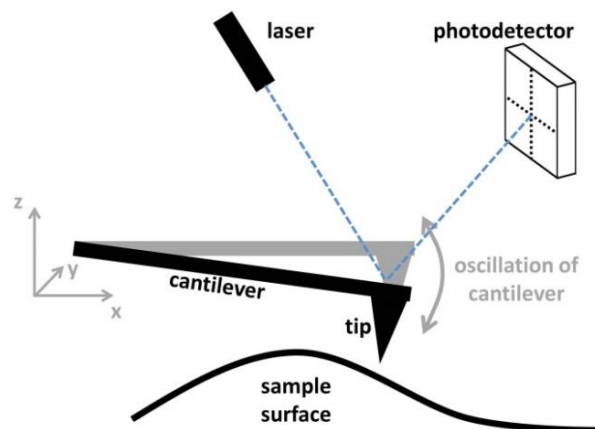


FIG. 4.11 The working principle of an AFM operated in 'intermittent contact mode'. While being systematically scanned over a surface the cantilever, to which a sharp tip is attached, is oscillated at a specific amplitude. This amplitude contains information about the z -coordinate of the sample surface. Light reflection from the backside of the cantilever is used to measure the amplitude of this oscillation.

where $h_{i,j}$ is the height at a position (x_i, y_j) in a topography map of $M \times N$ height measurements. There exists a large amount of statistics that are reasonable to apply to the measured surface topography. The autocorrelation function is one of them. It contains information about the occurrence, the length and the distance of possible correlations on the surface.

$$AC_{i,j} = \sum_{k=1}^{M-i} \sum_{l=1}^{N-j} h_{k,l} h_{i+k,j+l} \quad (4.7)$$

Further, by squaring the Fourier-transformation of the surface topography the area power spectral density can be obtained. The isotropic power spectral density is the average of this 2-dimensional function over all directions and can be applied to analyze periodic structures on the surface.

4.5 Model system: GaN growth on sapphire

In order to evaluate the feasibility of energy and mass selected IBAD, a thin film and a substrate material have to be chosen as model system. As previously mentioned, there is a large interest in nitride film synthesis by IBAD. One of the nitride materials, which attracted a significant amount of attention since the beginning of the 1990s is GaN. The relevance of GaN in the fabrication of blue light emitting diodes (LEDs) was acknowledged in that time [Nak93, Nak94]. Since then it was studied by many research groups using several, different methods for the synthesis. Nowadays, a large amount of knowledge about GaN, its properties, its structure and the possibilities and limitations of different deposition methods is available [Rut03]. In the context of this work it is beneficial to employ a well-known and well-studied material as model system, because it facilitates the assessment of the results with regard to the ion-solid interaction. Unlike with other metal nitride materials like e.g. TiN, ZrN or GdN, where the reactivity of the respective metal is high enough to chemically react with N_2 gas during thin film deposition directly, in the case of GaN the Ga metal is inert against molecular N_2 gas, preventing GaN formation. This is a prerequisite for the intended investigations in the frame of this thesis. Since the dependence of nitrogen ion beam parameters on the growth process is in the focus here, it is of advantage that thermal N_2 molecules from the background gas (i.e. without charge or energetic excitation) do not contribute to the GaN thin film growth.

In most cases, GaN crystallizes either in the wurtzite (w-GaN) or in the zincblende (z-GaN) structure [Mor08]. Both structures are illustrated in Fig. 4.12. The wurtzite structure is the thermodynamically stable structure for GaN. It is a hexagonal closed-packed lattice structure, which can be regarded as layered along w-GaN[0001]. There are two alternating layers, which are shifted with respect to each other. The layer sequence therefore is ABAB... The zincblende structure of GaN, however, is thermodynamically metastable.

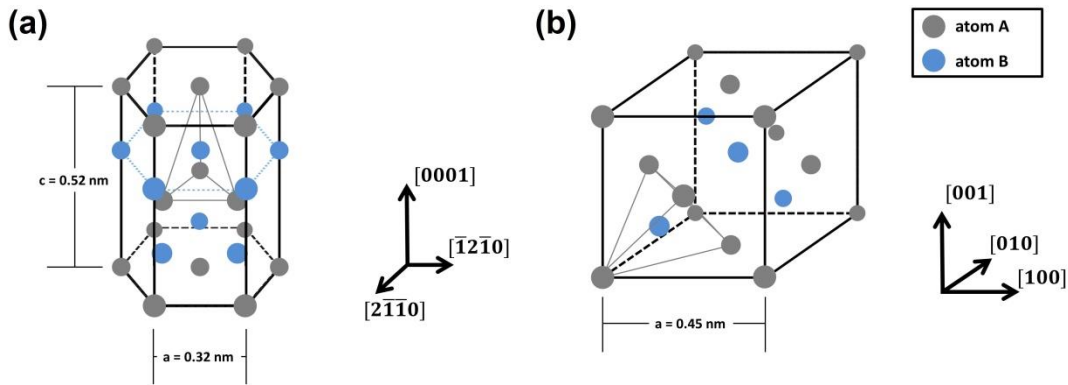


FIG. 4.12: Schematic representations of the crystal structure (a) wurtzitic GaN and (b) zincblende GaN. For the lattice constants see e.g. Morkoç [Mor08].

This lattice structure is face-centered cubic, which is also a closed-packed structure. The layers are stacked along the $[111]$ -direction in this case. In contrast to the wurtzite structure, there is a third layer present and the stacking sequence is ABCABC... For both cases an atom of one element is located in such a way that it has four nearest neighbors of the other element. This is indicated by the exemplary tetragons in Fig. 4.12. GaN was subject to extensive research in the past 25 years, mainly due to its properties as a semiconductor material with extraordinary optoelectronic characteristics [Tak07]. GaN exhibits a direct bandgap of $E_{gap} = 3.3 \dots 3.4$ eV, where the exact value depends on whether the structure is zincblende or wurtzite. It was also shown that by using alloy elements like Al or In in GaN the bandgap can be tailored. Due to its remarkable and tunable properties, GaN is an important material as constituent of electronic and optical devices, such as LEDs. Nevertheless, the possibilities to apply GaN in devices are not limited to LEDs, but also comprise e.g. laser diodes [Nak96], high electron mobility transistors for operation with high frequencies [Wal12] or at high power [Bal13] and integrated sensor applications [Stu02]. A multitude of deposition techniques have been applied successfully, among those are pulsed laser deposition [Vis97], hydride vapor phase epitaxy [Hem07], magnetron sputtering [Miy05], reactive [May99] and ion- or plasma assisted [Ger99] molecular beam epitaxy. However, variations of metal organic chemical vapor deposition [Nak91] are the ones that have gained the highest relevance in terms of industrial manufacturing of nitride semiconductor films.

To complete the model system Al_2O_3 is chosen as a substrate for the growth of GaN. Al_2O_3 is a frequently used substrate and well-established for the deposition of GaN because of its transparency, its easy availability and its high thermal and chemical stability [Liu02]. Possessing a band gap width $E_{gap} > 8$ eV Al_2O_3 is electrically insulating. Al_2O_3 has a rhombohedral structure, which in a simplified way can be described as a hexagonal closed-packed structure of O atoms with the lattice constants $a = 0.48$ nm and $c = 1.30$ nm, where two thirds of the octahedral voids are occupied by Al atoms. In the case of wurtzitic GaN growth on $\text{Al}_2\text{O}_3(0001)$, the GaN crystal

typically grows (0001)-oriented, too. However, the hexagonal GaN unit cell is rotated in-plane by 30° with respect to the Al_2O_3 unit cell, as it is shown schematically in Fig 4.13. For this epitaxial relation a lattice mismatch of 15% is obtained. For the growth of GaN on $\text{Al}_2\text{O}_3(1\bar{1}02)$, GaN typically grows $(11\bar{2}0)$ -oriented [Rod06]. This means, that the surface of the resulting GaN thin film is non-polar. Thin nitride films with non-polar surfaces are of interest, because device performance is expected to be enhanced, if there is no spontaneous or piezoelectric polarization along the growth direction [Pas08]. The symmetry of the interface in this case is not hexagonal, but rectangular. For this reason the lattice mismatch is anisotropic. It can be calculated to be 1% along $w\text{-GaN}[0001]$ and 15% along $w\text{-GaN}[1\bar{1}00]$. For the growth of GaN on $6\text{H-SiC}(0001)$, which is also well-established, the lattice mismatch is 3.1% [Liu02]. A comparably high lattice mismatch for the growth on Al_2O_3 results in lattice strain, which is usually released in the formation of defects like dislocations. Moreover, the thermal expansion of Al_2O_3 is larger than for GaN, which can cause additional damage to the produced thin film, when the substrate is cooled down after the deposition process.

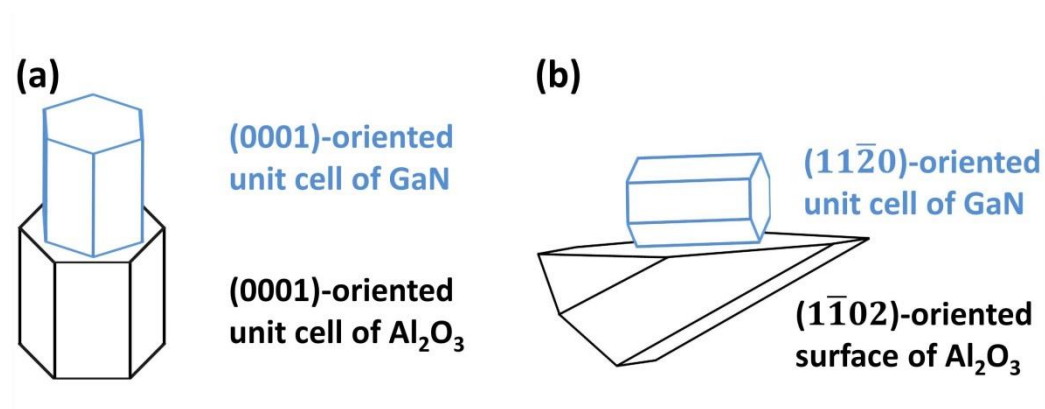


FIG. 4.13: Graphical representations of two typical epitaxial relationships between $w\text{-GaN}$ and Al_2O_3 surfaces. (a) (0001)-oriented GaN on (0001)-oriented Al_2O_3 and (b) non-polar $(11\bar{2}0)$ -oriented GaN on $(1\bar{1}02)$ -oriented Al_2O_3 .

5. Application of energy and mass selected ion-beam assisted deposition

After the applicability of the described setup for energy and mass selected IBAD was assessed and the relevant methods for thin film characterization were introduced, the consecutive step is to apply the setup and systematically carry out deposition experiments. In a first subsection, the aim of the application of this setup will be to synthesize spatially separated GaN nanocrystals. In a second subsection the setup is to be employed to synthesize compact GaN thin films with a high surface coverage. Thereby, the practical feasibility of energy and mass selected IBAD of very thin nitride films is to be ascertained. Accordingly, the purpose of the section is to discover the possibilities of energy and mass selected IBAD, in the context of the model system GaN grown on $\text{Al}_2\text{O}_3(1\bar{1}02)$. All sample sets presented in this section were produced on $\text{Al}_2\text{O}_3(1\bar{1}02)$ substrates, which were rinsed with isopropyl alcohol and de-ionized water. After the samples were introduced into the UHV system and brought into an appropriate position, they were heated at a small heat rate of $\sim 15 \text{ }^\circ\text{C min}^{-1}$ until the substrate temperature T_s was reached. Then, the sample was simultaneously exposed to both the energy and mass selected N ion beam and the Ga flux. For all cases presented in the following, this was done for 5 h. In order to reduce possibly remaining Ga agglomerations on the surface, subsequently, the samples were exposed only to the N ion beam for another 30 min. After that, the Ga effusion cell was shut and the samples slowly cooled down.

5.1 Growth of GaN nanocrystals

For small, spatially separated GaN crystals the terms 'quantum dot' or 'nanodot' are frequently used. Typically, such GaN quantum dots have dimensions of a few nm in height, a few 10 nm up to a few 100 nm laterally and area densities between $1 \cdot 10^8 \text{ cm}^{-2}$ and $1 \cdot 10^{12} \text{ cm}^{-2}$ [Sch11, Kad12, Yu14]. Here, such GaN structures will be referred to as nanocrystals. There exists significant research activity about such nanocrystals, also about non-polar nanocrystals, due to their interesting optical properties [Dau08]. It is to be pronounced that such non-polar GaN nanocrystals are also interesting and promising to be applied as template for thin film growth. It was recently shown that e.g. the density of crystal defects and the surface morphology can be controlled and optimized using such templates [Lee18].

As a first step towards energy and mass selected IBAD, such GaN nanocrystals are to be deposited and characterized. In this context, the quadrupole mass filter system was applied in the combination with the hollow-anode source. In this subsection, the results that could be obtained this way are presented in terms of quality and quantity of the surface coverage and the epitaxial relationship.

5.1.1 The influence of substrate temperature and Ga flux

In any thin film deposition process the substrate temperature T_s plays an important role, because diffusion, but also desorption and nucleation processes are temperature-dependent. For GaN it was shown, that thermal decomposition sets in already for temperatures as low as 710°C [Gro74], which yields an upper limit for T_s . In fact, recent studies, where IBAD was applied for the growth of GaN, revealed that the substrate temperature, which yields the best result in terms of crystal quality and surface topography, is 700°C [Pop15]. At this temperature the mobility of adatoms is enhanced and thermal decomposition has not set in, yet. In the frame of this work, the influence of the substrate temperature has to be evaluated again, since the deposition process is significantly changed compared to previous studies. In particular, the material fluxes are reduced. In IBAD, as shown in subsection 2.2.2, the ion-to-atom ratio $R_{I/A} = \phi_N^+ / \phi_{Ga}$ plays an important role, too. Therefore, as a first part of the deposition experiments the influence of $R_{I/A}$ also has to be investigated. This is done here by varying the effusion cell temperature T_{ec} and thereby ϕ_{Ga} , while keeping the ion current density j constant. In the later course of this section, the influence of the kinetic ion energy is to be evaluated. In order to facilitate comparison between depositions under irradiation with different kinetic energies, it is important that the ion current density remains constant. In general, it was shown in section 3 that a compromise must be found between low kinetic ion energies, which are necessary for avoiding deterioration of the crystal quality, and high ion current densities, which are favorable for high deposition rates. Here, this compromise is done by choosing $E_{kin} = 60$ eV as minimum kinetic energy for the subsequent investigations of the influence of the kinetic energy. Consequently, the ion current density is chosen to be the maximum ion current density, which is obtainable for $E_{kin} = 60$ eV. This ion current density is $j = (0.75 \pm 0.11) \mu\text{A cm}^{-2}$ corresponding to an ion flux $\phi_N^+ = (4.7 \pm 0.7) \cdot 10^{12} \text{ s}^{-1} \text{ cm}^{-2}$. Since the depositions presented in the following were assisted by N^+ irradiation only, $\phi_N = \phi_N^+$.

Fig. 5.1 depicts the temporal evolution of the RHEED patterns that were measured for different ϕ_{Ga} . The ion current density j was chosen as explained previously and the substrate temperature was chosen to be $T_s = 650^\circ\text{C}$, in order to ensure that thermal decomposition is negligible. The average kinetic energy was chosen to be 90 eV. Since ϕ_{Ga} is varied, $R_{I/A}$ also assumes different values, which are in this case 1.6, 1.1 and 0.7 (from the bottom to the top). The RHEED patterns in the left column originate from the Al_2O_3 substrate and therefore look similar in all depicted cases. Here, for all three cases, the arrangement of the intensity maxima is the same, the intensity is comparably high and the Kikuchi lines [Bra99], which are typical for smooth, crystalline substrates of high quality, are visible. For the highest Ga flux, the RHEED pattern of the Al_2O_3 substrate has completely vanished after 2 h. At the end of the deposition process, there is no pattern observable anymore, so it can be deduced that the surface is covered by non-crystalline material.

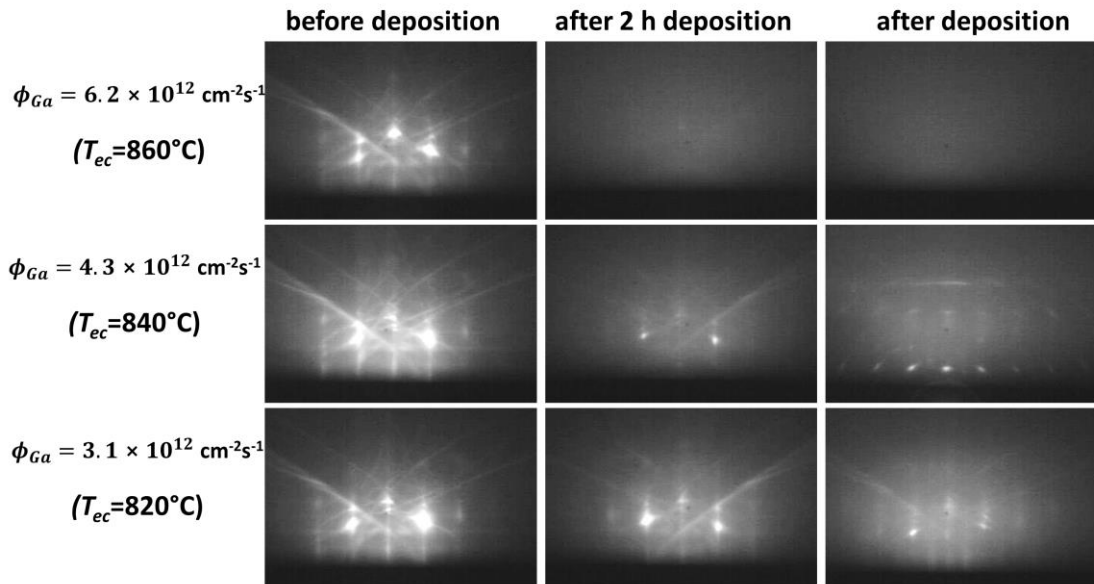


FIG. 5.1: RHEED patterns for three different ϕ_{Ga} (and correspondingly effusion cell temperatures T_{ec}). The depositions were carried out using N^+ ions with an average kinetic energy of (90 ± 20) eV. The ion current density for all samples was $j = (0.72 \pm 0.08)$ $\mu A/cm^2$ and the substrate temperature $T_s = 650^\circ C$.

Ga has a low melting point ($T_{melt} \approx 30^\circ C$). Therefore, in this case, where $\phi_{Ga} > \phi_N$, it can be assumed that liquid Ga droplets partially cover the surface [Zhe00]. If ϕ_{Ga} is small, the intensity of the RHEED pattern decreases with time, however, the arrangement of the intensity maxima in the RHEED pattern remains the same. Moreover, the Kikuchi lines originating from the substrate are still observable. Thus, it can be concluded, that in this case ($\phi_{Ga} < \phi_N$), the Ga flux is not sufficient for initiating significant changes to the substrate surface. Moreover, the adatom desorption depends on the ratio of Ga and N atoms on the surface. For a relatively small Ga concentration, the adatom desorption rate is larger [He06], reducing the Ga concentration on the surface even further. Regarding the case, where $\phi_{Ga} \approx \phi_N$, after 2 h of deposition time a decrease in intensity of the RHEED pattern associated with the Al_2O_3 substrate can be discerned. After the deposition process, a diffraction pattern occurs, which differs from the one that is associated with the Al_2O_3 substrate. Obviously, crystalline material has formed on the substrate surface in this case. Fig. 5.2 (a) shows a magnified image of this diffraction pattern. Due to the intensity maxima being point-like, it is found, that there is 3-dimensional growth of a crystalline film. Two rows of point-like intensity maxima can be observed here. Even a third row is slightly visible. However, this third row of high intensity seems to be blurred and not to consist of points. The Kikuchi lines of the Al_2O_3 substrate have vanished. Though, between the first two rows, two points are slightly visible, which are remnants of the diffraction pattern from the Al_2O_3 substrate. The presence of these two points indicates that the substrate surface is not completely covered by such a 3-dimensionally grown crystalline film. A diffraction pattern as it can be seen in Fig. 5.2

(a) also implies that the growth of these crystals is epitaxial. RHEED can also be used to determine the epitaxial relationship. In order to do so, it is necessary to know the orientation of the Al_2O_3 substrate with respect to the electron beam. As indicated in Fig. 5.2 (a), the electron beam is parallel to $\text{Al}_2\text{O}_3[1\bar{1}01]$. In subsection 4.5 it was already stated that GaN typically grows non-polar on $\text{Al}_2\text{O}_3(1\bar{1}02)$. In that case, the electron beam would be expected to be parallel to one of the following two directions of high symmetry w-GaN $[0001]$ or w-GaN $[11\bar{2}0]$. Fig. 5.2 (b) shows the arrangement of some expected intensity maxima labelled with the corresponding Miller indices for the case that the electron beam is parallel to w-GaN $[0001]$. For determining the expected positions of the intensity maxima, the software 'CaRine Crystallography' was made use of. It is evident that there is agreement between the expected and the measured diffraction pattern. Therefore, it can be confirmed that the 3-dimensionally and epitaxially grown crystalline films that partly cover the Al_2O_3 surface are w-GaN crystals. These GaN crystals are as expected non-polar. The analysis of the RHEED pattern reveals that the epitaxial relationship is as follows:

$$\text{w-GaN}(11\bar{2}0) \parallel \text{Al}_2\text{O}_3(1\bar{1}02) \quad \text{and} \quad \text{w-GaN}[0001] \parallel \text{Al}_2\text{O}_3[1\bar{1}01].$$

For w-GaN thin films with this epitaxial relationship, RHEED was also measured by other groups yielding diffraction patterns with the same arrangement of intensity maxima compared to the one presented here [Asc09]. Summing up Fig. 5.1, three different sample types are found. For $T_s = 650^\circ\text{C}$ those are:

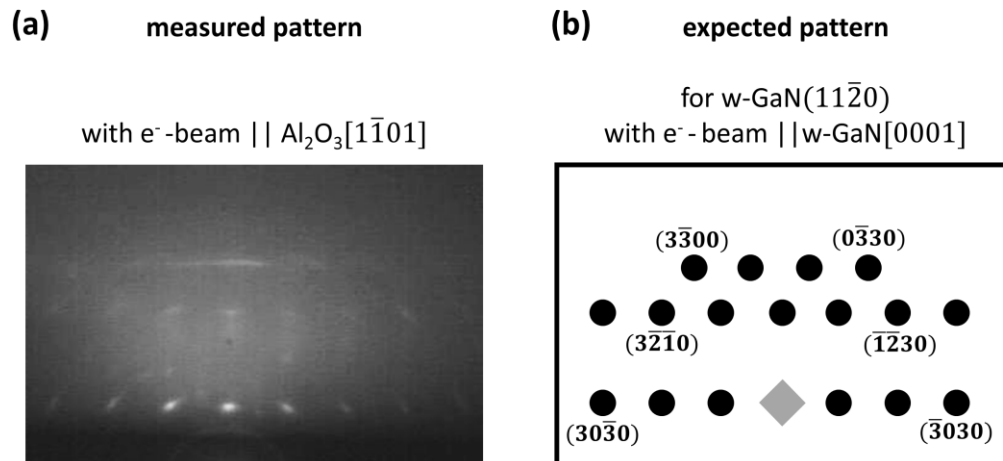


FIG. 5.2: (a) Magnified measured RHEED pattern as shown in Fig. 5.1 and (b) theoretical position of specific RHEED intensity maxima assuming a $(11\bar{2}0)$ -oriented w-GaN crystal, where the electron beam is parallel to w-GaN $[0001]$. Some of the intensity maxima are labelled with the respective Miller indices. The grey square in the bottom row represents the position of the electron beam that was reflected without being diffracted.

- I. $R_{I/A} < 1$: The substrate surface is predominantly covered by liquid or amorphous Ga.
- II. $R_{I/A} \approx 1$: The substrate surface is covered by epitaxial, non-polar, 3-dimensionally grown, w-GaN crystals.
- III. $R_{I/A} > 1$: There is no significant coverage of the substrate surface.

As second quantity of relevance in this subsection, T_s was already mentioned. Fig. 5.3 illustrates the regions in the T_s/T_{ec} -parameter space, where these three sample types occur. Regarding the influence of the substrate temperature, it can be seen, that at smaller substrate temperature ($T_s = 600^\circ\text{C}$), the formation of crystalline GaN is observed already for smaller ϕ_{Ga} . Simultaneously, for a larger substrate temperature ($T_s = 700^\circ\text{C}$), a comparably large ϕ_{Ga} is not sufficient to cause any growth processes on the substrate surface. In previous studies, where the quadrupole mass filter was not applied, it was possible to synthesize GaN thin films over a broad range of $R_{I/A}$ [Neu13]. Compared to such studies an important difference is that the material fluxes are smaller here. Therefore, the density of adatoms on the surface is smaller and the process is more sensitive to an increase of the adatom desorption. Thus, the observed dependence of the substrate temperature on the crystal growth, might be due to the temperature dependence of the adatom desorption rate, which can be considered to be less dominant for smaller temperatures [Hey00]. This means that at larger substrate temperature Ga desorbs fast, such that at any time the concentration of available Ga atoms on the surface is small. The growth of GaN, however, requires a certain concentration of Ga on the surface to take place.

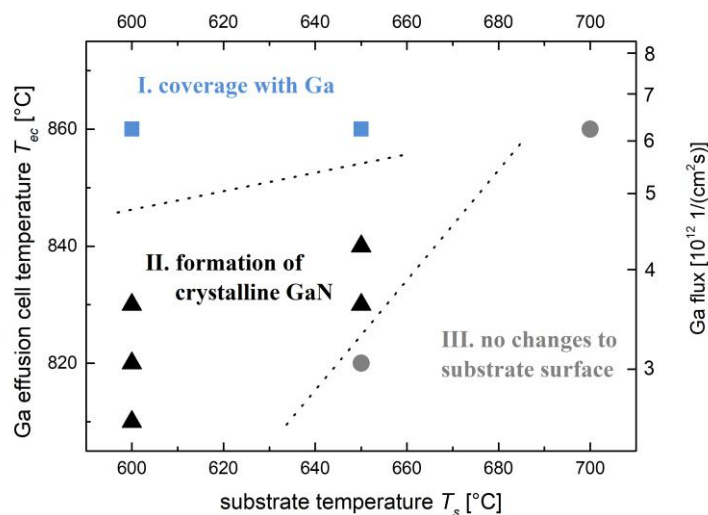


FIG. 5.3: The T_s/T_{ec} -parameter space for GaN depositions using N^+ ions with an average kinetic energy of 90 eV and an ion current density of $j = (0.77 \pm 0.1) \mu\text{A}/\text{cm}^2$. The dotted lines are added as guide for the eye indicating the borders of regions in this parameter space, where different sample types result.

At smaller substrate temperature, desorption rates are small, meaning that the Ga concentration is sufficient for GaN growth. If ϕ_{Ga} is increased above a certain level, the Ga concentration on the surface becomes so large, that the formation of Ga agglomerations is favored instead of the formation of crystalline GaN [Bro06].

The presence of three sample types can also be observed in the surface composition as measured by AES. Fig. 5.4 shows four measured Auger electron spectra. The first spectrum was measured for a bare Al_2O_3 substrate. Within the measured interval of electron energies, there is only one peak observable, which is the peak corresponding to the KLL Auger electron transition in O atoms. When the RHEED measurements suggest that the substrate surface is not significantly covered (as in (ii)), a second, smaller peak emerges. This peak originates from the KLL Auger electron transition in N atoms. Although in RHEED the diffraction pattern of the substrate is still visible, here N can be detected on the surface. Note, that AES is more sensitive for N than e.g. for Ga [Dav78]. Therefore, it is possible that the area density of Ga atoms bound to N atoms is sufficiently small for the Ga content not to be detectable. An alternative explanation is that a certain fraction of incoming N ions is implanted in a volume near the Al_2O_3 surface. According to SRIM calculations similar to those depicted in Fig. 2.6, the medium projected range of N^+ ions with $E_{kin} = 90$ eV in Al_2O_3 can be estimated to 0.6 nm with a straggling (FWHM) of 0.3 nm. This means that a certain number of ions may be implanted into the second monolayer or even below. The origin of the N peak here would consequently be implanted N atoms instead of GaN crystals on the surface. When the RHEED pattern reveals the formation of GaN crystals, in the Auger electron spectrum (as in (iii)) a contribution of the LMM transition in Ga atoms is present in addition.

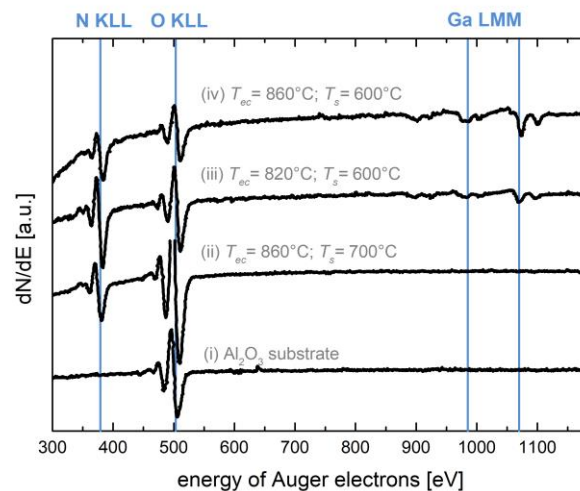


FIG. 5.4: Auger electron spectra for the Al_2O_3 substrate and for three sample types from the parameter space in Fig. 5.3 as labelled. The blue lines indicate the position of the minimum in the derivative dN/dE for the respective Auger electron transitions [Dav78]. The measurement of the Al_2O_3 was performed with decreased lock-in amplifier sensitivity (50 %) compared to the measurements (ii)-(iv).

Furthermore, in relation to the O peak, the N peak has become more prominent compared to the previously discussed case. This indicates, that a larger fraction of the surface is covered and possibly both the area density of Ga and N atoms on the surface is larger. Finally, an Auger electron spectrum was also measured for the case, for which the surface is assumed to be covered by Ga according to the previous considerations (as seen in (iv)). For such a measurement, the Ga peak becomes more prominent in relation to both the O and the N peak. All in all, the data obtained from the Auger electron spectra agrees with the previous considerations based on the evaluation of the RHEED patterns.

In order to extend the investigations of the sample set summed up in Fig. 5.3, AFM measurements were performed. The AFM measurement shown in Fig. 5.5 (a) was performed on a bare Al_2O_3 substrate. On an area of $2\ \mu\text{m} \times 2\ \mu\text{m}$, the average roughness is negligible with $RMS = 0.1\ \text{nm}$. However, in AFM measurements of the sample type with a high Ga coverage, as shown in Fig. 5.5 (c), the Ga coverage can clearly be identified. It can be discerned, that there are no smooth, plain regions left on the depicted area. The substrate surface is mainly covered by Ga droplets. The isotropic power spectral density function (see subsection 4.4) for this measurement exhibits a maximum, from which the average separation of maxima can be determined to be $(135 \pm 35)\ \text{nm}$. Since the droplets cover nearly the whole surface, this can also be understood as an approximate value for the lateral size of the droplets.

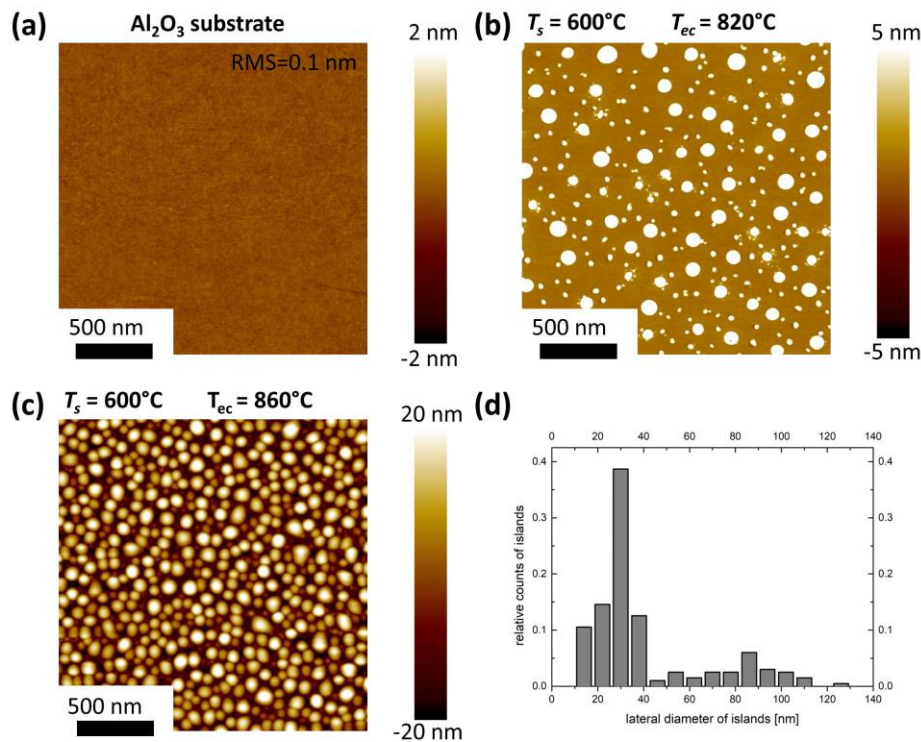


FIG: 5.5: AFM measurements of (a) the bare Al_2O_3 substrate, GaN films produced using N^+ ions with an average kinetic energy of 90 eV, with $T_s = 600^\circ\text{C}$ and with (b) $T_{ec} = 820^\circ\text{C}$ and (c) $T_{ec} = 860^\circ\text{C}$. The size distribution of islands (defined by a threshold of 3nm) in (b) is depicted in (d).

The third AFM measurement in Fig. 5.5 (b) reveals a smooth background, which can be identified as the Al_2O_3 substrate. On such a surface, mounds with different lateral size can be observed protruding from this smooth background. By choosing a threshold value of 3 nm, and defining every structure above this threshold as island, a total of 199 islands can be counted. The distribution of the lateral size of these islands is plotted in Fig. 5.5 (d). This distribution exhibits a maximum for lateral diameters of approx. 30 nm. 76 % of the counted islands have lateral diameters below 42 nm. Though, a second maximum evolves for lateral diameters of approx. 85 nm. Apparently, two different kinds of island structures are present on the surface. There are structures with a typical lateral size of 85 nm, which is similar to the lateral size of the Ga droplets, mentioned in the context of Fig. 5.5 (c). Furthermore, there is a much larger number of smaller structures. RHEED and AES measurements suggest the presence of GaN crystals on such samples. Therefore, it can be assumed, that those structures with lateral diameters of up to approx. 40 nm, are w-GaN crystals. For comparing the lateral size of the droplets and the nanocrystals, the report of Debnath *et al.* can be used [Deb09]. For $T_s = 580^\circ\text{C}$, these authors found average diameters of 200 nm and 60 nm for Ga droplets and GaN nanodots, respectively. Due to the different substrate (Si(111)) used in that case, the droplets or nanocrystals cannot be expected to have the exact same diameters as in the frame of this work. However, the order of magnitude is the same and the ratio of the diameters of droplets and nanocrystals is comparable. In general, comparing to reports about GaN nanodots such as the one of Debnath *et al.* suggests that in this case the GaN nanocrystals are formed by Ga droplet nitridation.

5.1.2 The role of the kinetic energy

In the previous subsection, it was shown that for a chosen ion current density of $j = (0.75 \pm 0.11) \mu\text{A cm}^{-2}$, the substrate temperature T_s and the Ga flux ϕ_{Ga} have to fulfill certain conditions if the formation of GaN crystals is desired. Based on these findings, now the influence of the kinetic ion energy E_{kin} on the formation of GaN crystals at a constant ion current density of $j = 0.75 \mu\text{A cm}^{-2}$ can be investigated. The substrate temperature is chosen to be $T_s = 650^\circ\text{C}$, since for this temperature it could already be shown, in which interval of ϕ_{Ga} crystalline GaN can be deposited. Fig. 5.6 is a compilation of RHEED patterns that were taken after the deposition and the post-nitridation. Here, the influence of both ϕ_{Ga} and E_{kin} is discernable. The patterns for the smaller $R_{I/A}$ ($R_{I/A} < 1.5$) are all similar to the diffraction pattern shown in Fig. 5.2 (a). The only difference between these diffraction patterns is the intensity and the number of diffraction orders that appear. Hence, in terms of epitaxial relationship and growth mode no differences are found. However, differences in the intensity of the diffraction patterns suggest that size and area density of GaN crystallites as well as the coverage of the surface with such crystallites differ significantly.

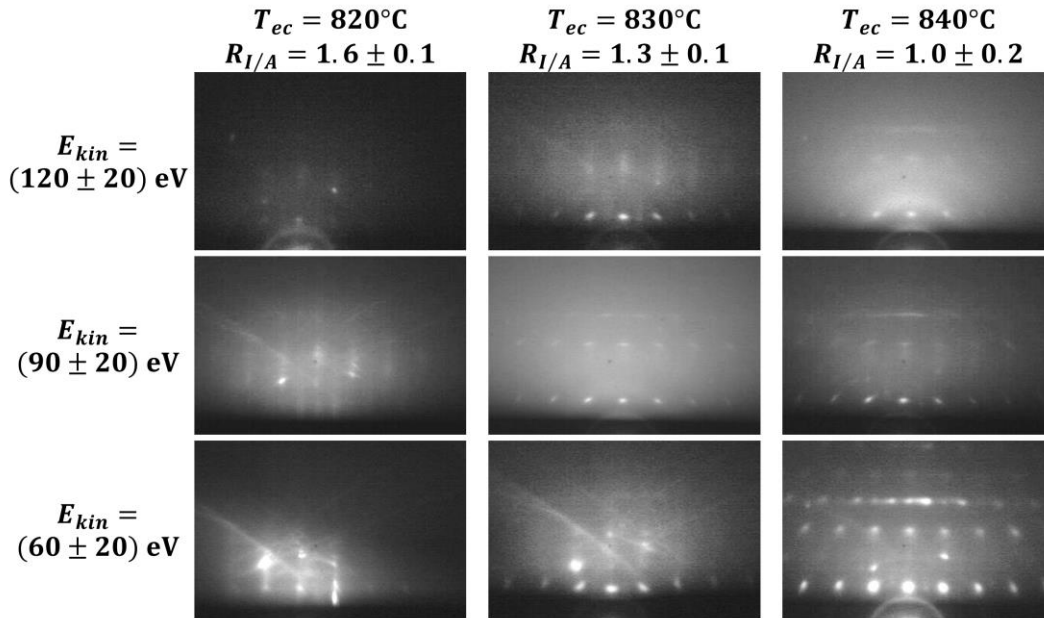


FIG. 5.6: RHEED patterns for GaN films produced with different ion kinetic energy and Ga flux. Depositions were carried out using N^+ ions with a constant ion current density. The substrate temperature was $T_s = 650^\circ\text{C}$. Each RHEED pattern was taken after the post-nitridation. The kinetic energy of the ions is increased from the bottom to the top and the Ga flux increased from the left to the right as labelled next to the patterns. The error of the kinetic energy is assumed as half of the FWHM of the energy distribution.

The diffraction pattern which is the most pronounced was measured for $R_{I/A} = 1.0$ and $E_{kin} = 60$ eV. This kinetic energy is relatively close to the Brice window (see subsection 2.2.1), so here, crystalline growth with a high quality is expected rather than if higher kinetic energies are applied. There are three reasons, why the yield of crystalline GaN can be expected to be larger if smaller kinetic energies are applied:

- 1) **Sputtering** is to be taken into account for higher ion energies. Here, ion irradiation might already cause an erosion of the deposited GaN.
- 2) **Damage formation in the Al_2O_3 substrate** is also relevant particularly for higher energies. As can be seen for larger $R_{I/A}$ ($R_{I/A} = 1.6$) the diffraction pattern associated with the Al_2O_3 substrate and the Kikuchi lines are less intense with increasing ion energy. For $E_{kin} = 120$ eV, the pattern is hardly visible anymore. Also for $R_{I/A} < 1.6$, the substrate pattern is clearly observable at smaller kinetic energies ($E_{kin} = 60$ eV), while it cannot readily be identified for higher E_{kin} . This is an apparent indication for ion-induced surface-near substrate damage. If the substrate surface is damaged, it can be assumed that this considerably impedes epitaxial growth.
- 3) **Ion implantation** leads to a decrease of the number of ions available for growth processes. A large fraction of ions with $E_{kin} = 120$ eV can be expected to penetrate below the surface and stop e.g. in the third monolayer or deeper. The first consequence is that damage is induced, which may impede the

epitaxial growth. A second consequence might be that a fraction of ions is implanted into the substrate and therefore the effective number of ions which is available for the growth process on the surface, i.e. on the first monolayer, is decreased. This explanation is supported by the following observation: For $E_{kin} = 60$ eV the coverage of the surface with crystalline GaN is most significant for $R_{I/A} = 1.0$. Simultaneously, the diffraction pattern associated with the substrate is clearly discernable. When a kinetic ion energy of $E_{kin} = 120$ eV is regarded, for the same $R_{I/A}$, there are no intensity maxima associated with the substrate. However, when ϕ_{Ga} is decreased such that $R_{I/A} = 1.3$ (and still $E_{kin} = 120$ eV), the Kikuchi lines of the substrate diffraction pattern are visible again. This means that for higher kinetic energies, ϕ_{Ga} must be smaller for avoiding a high Ga coverage of the substrate. This may indicate that the number of available N ions is smaller than if a smaller ion energy is applied.

As described, these considerations are mainly with regard to size and density of deposited GaN crystals. The most significant coverage with crystalline GaN was found for $E_{kin} = 60$ eV and $R_{I/A} = 1.0$. In order to specify the density and size of the GaN crystals, for this set of deposition parameters AFM measurements were conducted, one of which is shown in Fig. 5.7 (a). Similar to the AFM measurement shown in Fig. 5.5 (b), there is also a smooth background, identified as the Al_2O_3 substrate. On the substrate, a large number of islands can be identified. If a threshold value of 1 nm is set, a number of 606 islands is obtained for this measurement covering approx. 5.2 % of the surface area. This corresponds to an island density of $1.5 \cdot 10^{10} \text{ cm}^{-2}$. The distribution of the lateral diameter of these islands is shown in Fig. 5.7 (b). The lateral diameter is below 40 nm with a maximum evolving approx. for diameters of 20 nm. The lateral size of those islands is comparable to the islands that were identified as GaN crystals in Fig. 5.5. Also for these deposition parameters, it can be assumed that the RHEED diffraction pattern is caused by such islands, which are correspondingly epitaxially grown w-GaN nanocrystals. The height of these GaN nanocrystals is below 10 nm. Height, lateral diameter and density of the GaN nanocrystals are in agreement with 'nanodots' or 'quantum dots' as frequently referred to in the literature.

In order to confirm that the observed crystals are GaN, the presence of both Ga and N on the surface can additionally be proven by XPS. The respective spectrum is shown in Fig. 5.7 (c). Since the coverage of 5.2 % as it was determined by AFM, is relatively small, in this spectrum the substrate contributions are comparably strong. Among those are the 2s and the 2p photoelectrons from the Al atoms in the substrate and particularly the 1s photoelectrons from the O atoms. As in the previously shown Auger electron spectra, in this XPS spectrum, KLL Auger electrons from the O atoms also contribute. The presence of Ga can be proven by two contributions to this photoelectron spectrum.

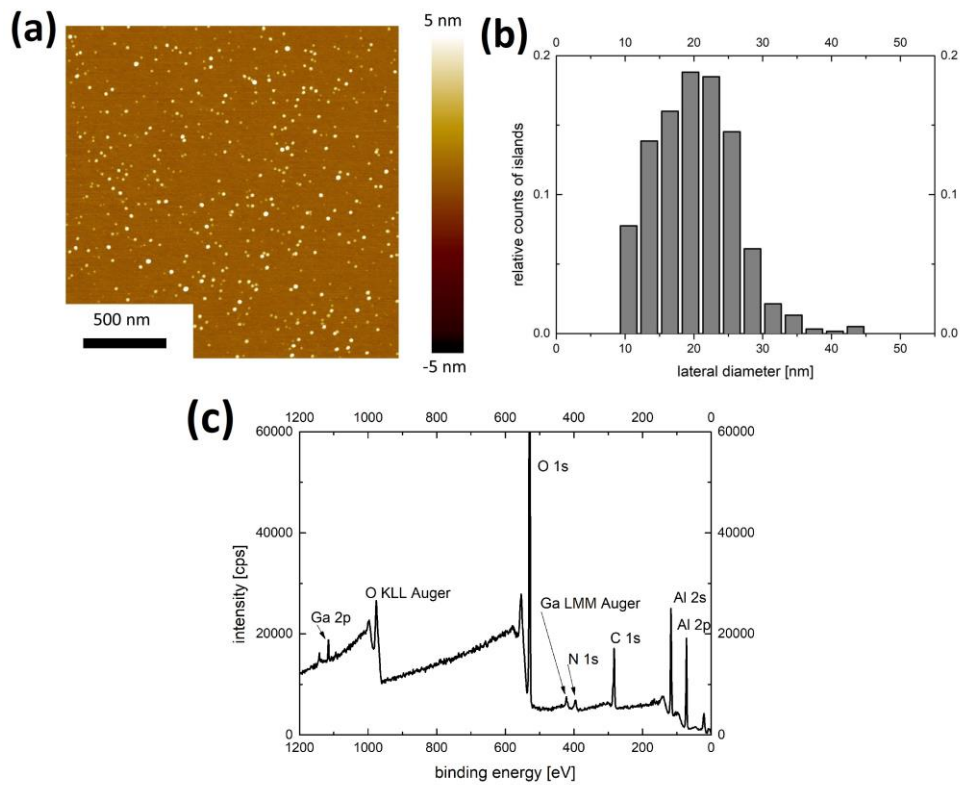


FIG. 5.7: (a) AFM measurement of GaN nanocrystals. The corresponding RHEED pattern is depicted in Fig. 5.6 [$E_{kin} = (60 \pm 20)$ eV; $R_{I/A} = 1.0$; $j = (0.72 \pm 0.08)$ $\mu\text{A}/\text{cm}^2$; N^+ ions]. (b) The distribution of lateral diameters of islands on the measurement shown in (a) defined by a threshold value of 1 nm. (c) XPS spectrum measured from this set of samples using Al $\text{K}\alpha$ radiation.

The first is the one of the 2p electrons appearing for high binding energies. These electrons are degenerate and the binding energy is $E_{pe} = 1117$ eV for a magnetic quantum number $m = 3/2$ and $E_{pe} = 1144$ eV for $m = 1/2$ [Mou95]. Both corresponding peaks are clearly visible in this spectrum. The second contribution of Ga atoms is the Auger line of the KLL transition. If Al $\text{K}\alpha$ irradiation is applied to excite this Auger electron transition, the 'binding energy' value that corresponds to the kinetic energy of these Auger electrons is $E_{pe} = 417$ eV. The presence of N on the sample surface can also be shown by the contribution of the 1s photoelectrons appearing at $E_{pe} = 398$ eV [Mou95]. Apart from the presence of both Ga and N, this spectrum reveals a clean surface and demonstrates that there is no significant amount of undesired contaminations. The only peak in this spectrum that belongs neither to the GaN nanocrystals nor to the Al_2O_3 substrate is the peak that originates from the 1s photoelectrons of C atoms. Since XPS was not measured *in vacuo*, the sample had to be transferred and was exposed to the atmosphere in the laboratory. The C contamination is caused during this transfer.

5.1.3 Crystal structure of GaN nanocrystals

Up to now, the formation of thin films consisting of single, well-separated GaN nanocrystals was described. Furthermore, it was found that the deposition with $R_{I/A} = 1.0$ and assisted by N^+ irradiation with $E_{kin} = 60$ eV leads to the largest deposition rate of crystalline GaN. This subsection is focused on the characterization of those crystals themselves. XRD and TEM measurements provide supplementary information with regard to the crystalline structure and the epitaxial relationship to the substrate. The dimension of the GaN crystals is still small and a typical XRD analysis including $2\theta/\omega$ measurements is challenging, because peak positions of substrate and nanocrystals are close to each other, while the substrate peak is several orders of magnitude more intense. However, in an XRD pole figure, the pole density maxima originating from the Al_2O_3 substrate and the GaN nanocrystals are well-separated. In Fig. 5.8 (a) such a pole figure measurement is presented for the w-GaN $\{10\bar{1}1\}$ planes. Comparison of an experimentally measured pole figure with the simulated pole figure in Fig. 5.8 (b) enables the association of the occurring pole density maxima to the respective family of lattice planes. The w-GaN $\{10\bar{1}1\}$ planes have a similar lattice spacing compared to the $Al_2O_3\{11\bar{2}0\}$ planes and the $Al_2O_3\{1\bar{1}04\}$ planes ($\pm 1^\circ$ in 2θ for Cu K_α radiation). Thus, these pole density maxima appear with a high intensity in the pole figure measurement. Also the $Al_2O_3\{0006\}$ planes ($\Delta(2\theta) = 4.85^\circ$ with Cu K_α radiation compared to the w-GaN $\{10\bar{1}1\}$ planes) contribute to the pole figure measurement, probably due to the corresponding Cu K_β or W L_α contribution. The w-GaN $\{10\bar{1}1\}$ planes have sixfold symmetry. Thus 6 pole density maxima are expected in the pole figure. Four of those pole density maxima are expected at $\alpha = 40^\circ$, while two further pole density maxima originate from planes perpendicular to the sample surface. The pole density maxima therefore are expected to be at $\alpha = 90^\circ$. The positions of the first four pole density maxima are very close to those of the Al_2O_3 substrate. The remaining two pole density maxima appear as four, since they are positioned at $\alpha = 90^\circ$ and therefore measured from two sides each.

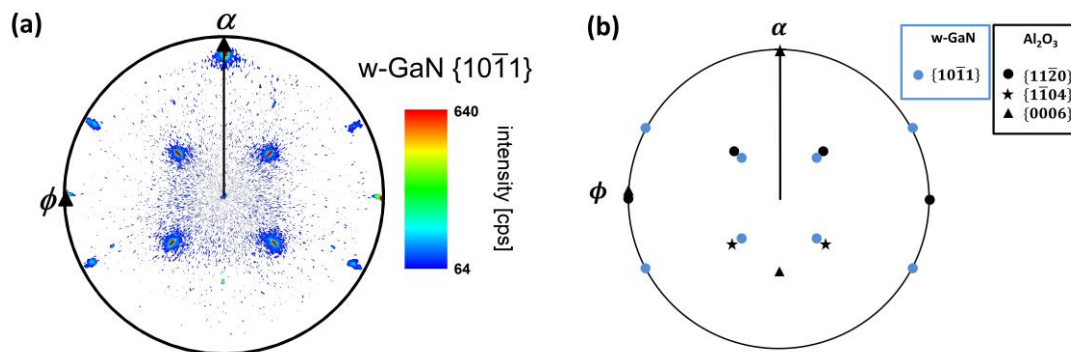


FIG. 5.8: (a) w-GaN $\{10\bar{1}1\}$ XRD pole figure measurement of GaN nanocrystals produced with N^+ ions with $E_{kin} = (60 \pm 20)$ eV and $R_{I/A} = 1.0$ (for corresponding RHEED pattern see bottom right in Fig. 5.6). (b) Expected position of some intensity maxima in a w-GaN $\{10\bar{1}1\}$ pole figure measurement, if the epitaxial relationship is as described earlier (see subsection 5.1.1).

Regarding these positions an unambiguous association with w-GaN lattice planes is feasible. Due to the occurrence of pole density maxima of both the Al_2O_3 substrate and the w-GaN nanocrystals, this pole figure measurement can confirm the presence of w-GaN crystals with the epitaxial relationship that was given earlier (see subsection 5.1.1).

Additionally, TEM was applied in order to obtain microscopic, cross-sectional images of such GaN crystals. Two lamellae were cut for TEM investigations. The first lamella was cut along $\text{Al}_2\text{O}_3[11\bar{2}0]$ and w-GaN $[\bar{1}\bar{1}00]$, respectively. Figure 5.9 (a) depicts a HRTEM image of such a GaN nanocrystal. The crystal possesses a height of 10 nm and a lateral diameter of approx. 15 nm. These dimensions are comparable to those, which were found by the AFM measurements. Since the viewing direction is w-GaN $[0001]$, a hexagonal arrangement of atoms is seen. The hexagonal structure is disturbed within a layer of a few nm above the interface. Above this layer the hexagonal arrangement of intensity maxima is regular and undisturbed. It is however apparent that the GaN nanocrystal is tilted to the right side. The w-GaN $[11\bar{2}0]$ -direction is expected to be perpendicular to the interface of the substrate and the GaN crystal. The angle between this direction and $\text{Al}_2\text{O}_3[\bar{1}\bar{1}20]$, which is parallel to the interface and perpendicular to the viewing direction, is $(85\pm 1)^\circ$ instead of 90° as would be expected. Fig. 5.9 also contains Fast Fourier transformation (FFT) images of the Al_2O_3 substrate and the GaN crystal. The simulated FFT patterns as shown in Fig. 5.9 (c) and (e), were produced by the software 'CaRine Crystallography'.

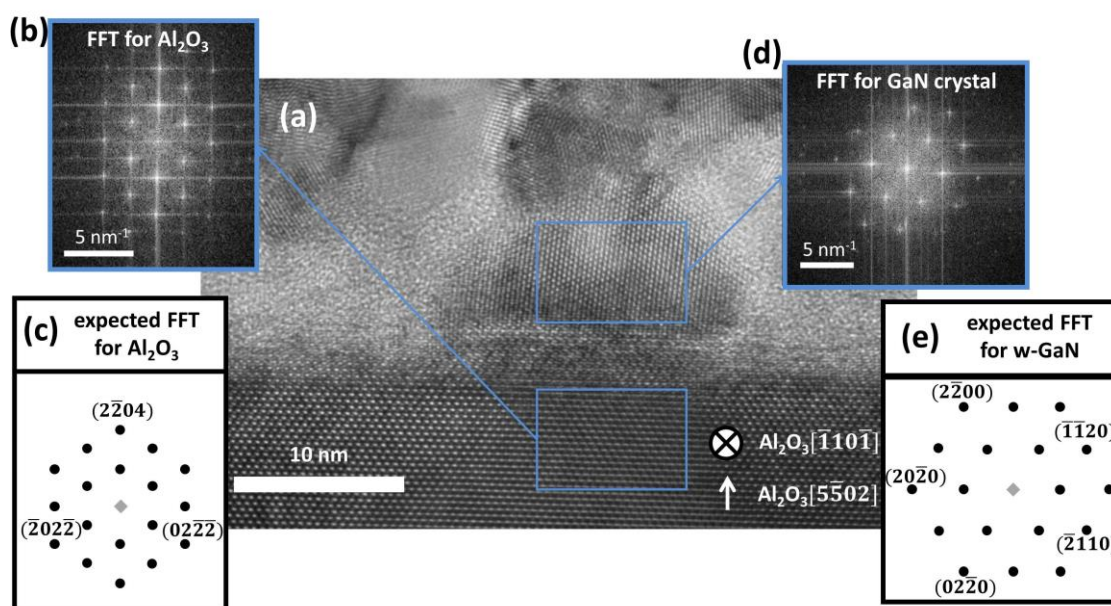


FIG. 5.9: (a) HRTEM analysis of a GaN nanocrystal [$E_{kin} = (60 \pm 20) \text{ eV}$; $R_{I/A} = 1.0$; $j = (0.72 \pm 0.08) \mu\text{A cm}^{-2}$; N^+ ions]. The viewing direction is w-GaN $[0001]$. (b) FFT image obtained from the Al_2O_3 substrate in (a). (c) Simulated FFT image for the Al_2O_3 substrate assuming the already determined epitaxial relationship. (d) FFT image obtained from the w-GaN nanocrystal in (a). (e) Simulated FFT image for the w-GaN nanocrystal. FFT simulations were performed by using the software 'CaRine Crystallography'.

For the Al_2O_3 substrate, the experimentally determined and the simulated FFTs are in agreement. Also for the GaN crystal there is agreement between the experimentally and the theoretically determined FFT. In both cases, the arrangement of the atoms in this cross-sectional image is represented by a hexagonal intensity pattern in the FFT. Though, the tilt of the w-GaN unit cell with respect to the w-GaN[0001]-axis is also apparent in the FFT images. The second lamella was cut along $\text{Al}_2\text{O}_3[\bar{1}10\bar{1}]$ and w-GaN[0001], respectively. Fig. 5.10 (a) is a representation of a HRTEM measurement that was conducted on such a lamella. Again, a GaN crystal is clearly visible. Its approximate dimensions being 10 nm in height and 20 nm laterally are also similar to the AFM measurements shown before. For this cross-section in contrast to the previous one, the atoms are expected to show a rectangular arrangement in the GaN crystal, which is clearly observable. Comparably to the previously presented lamella, the TEM image here yields a periodic pattern with no significant irregularities. A difference in comparison to the previously presented lamella is the interface of the Al_2O_3 substrate. Here, this interface is well-defined. The periodic pattern, corresponding to the arrangement of the atoms in the GaN crystal, sets in almost immediately. A layer with a certain thickness, where the periodic patterns of the Al_2O_3 substrate or the GaN crystal appear disturbed, is not as striking as in the previous case. Moreover, in the HRTEM image, the w-GaN[11 $\bar{2}$ 0]-axis does not reveal any angle with respect to the interface that significantly differs from 90° . Therefore, there is no crystal tilt observable in this HRTEM measurement. Here, the FFT images for both the Al_2O_3 substrate and the w-GaN crystal coincide with the expected patterns.

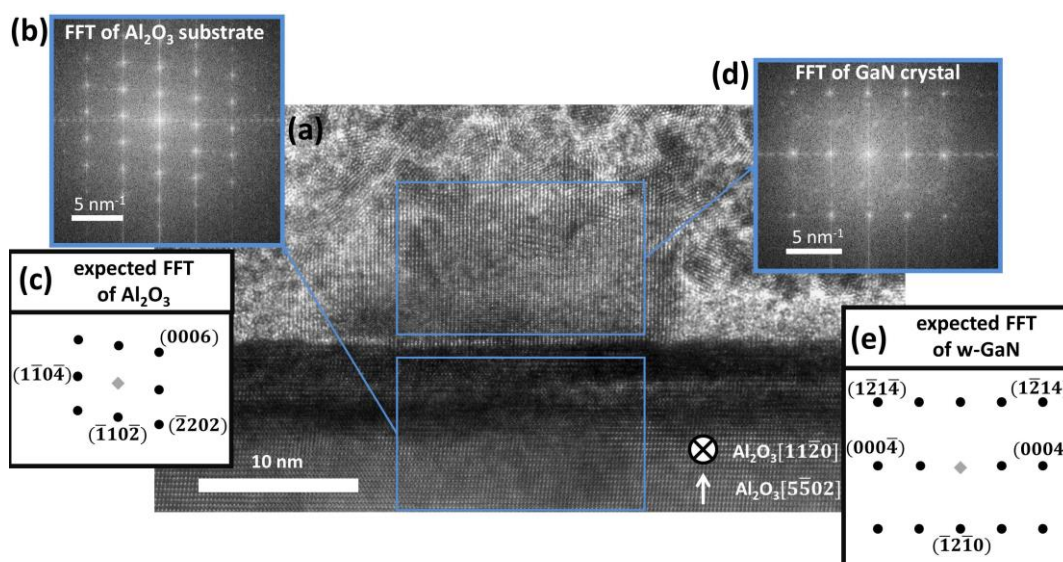


FIG. 5.10: (a) HRTEM analysis of a GaN nanocrystal [$E_{kin} = (60 \pm 20) \text{ eV}$; $R_{I/A} = 1.0$; $j = (0.72 \pm 0.08) \mu\text{A cm}^{-2}$; N^+ ions]. The viewing direction is w-GaN[1 $\bar{1}$ 00]. (b) FFT image obtained from the Al_2O_3 substrate in (a). (c) Simulated FFT image for the Al_2O_3 substrate assuming the already determined epitaxial relationship. (d) FFT image obtained from the w-GaN nanocrystal in (a). (e) Simulated FFT image for the w-GaN nanocrystal. FFT simulations were performed by using the software 'CaRine Crystallography'.

Considering both lamellae, the suggested crystal structure and the epitaxial relationship could again be confirmed. A tilt of the GaN crystals into the $\text{Al}_2\text{O}_3[11\bar{2}0]$ direction was observed. As mentioned above, the lattice mismatch of wurtzitic GaN growing on $\text{Al}_2\text{O}_3(1\bar{1}02)$ is anisotropic. The larger lattice mismatch of 15 % occurs along $\text{Al}_2\text{O}_3[11\bar{2}0]$. A tilt of the GaN crystal in this direction was observed. The smaller lattice mismatch of only 1 % is along $\text{Al}_2\text{O}_3[\bar{1}10\bar{1}]$. This lattice mismatch is relevant for the interface as observed in the second case (Fig. 5.10). Here, no tilt of GaN crystals was found and additionally the interface appeared less disturbed as in the first case. Note, that TEM measurements are very local methods for the characterization of epitaxial crystals. For a meaningful and general proposition about the tilt of crystals it is not sufficient to regard only some crystals. Though, since there is an anisotropic lattice mismatch, it is reasonable to take this into account when analyzing these TEM measurements and further consider them as a reason for differences particularly in the interface structure that is observed in different directions. For non-polar, wurtzitic thin films grown on Al_2O_3 , typically the defect structure is dominated by the presence of planar basal stacking faults, accompanied by partial dislocations and possibly prismatic stacking faults [Ven12]. These basal stacking faults are supposedly created in coalescence boundaries. It is therefore consistent that in the TEM measurements here, such basal or prismatic stacking faults cannot be observed.

5.1.4 Deposition of GaN using molecular N ions

All results presented in this section up to now, refer to the GaN deposition using N^+ ions only. Since ion mass selection is a crucial part of this work, it is necessary to also evaluate the possibility to deposit GaN thin films using N_2^+ ions. Fig. 5.11 presents RHEED patterns for such thin films where the N_2^+ ion irradiation was carried out with $E_{kin} = (60 \pm 5)$ eV and with varying $R_{I/A}$. The ion current density $j = (0.82 \pm 0.04)$ $\mu\text{A cm}^{-2}$ is the same as in Fig. 5.6. Employing N_2^+ ions, the three sample types defined in subsection 5.1.1 are recognizable, too: For large $R_{I/A}$ ($R_{I/A} = 1.7$), the RHEED pattern originating from the Al_2O_3 substrate dominates, suggesting a lack of sufficient Ga concentration on the surface, while for small $R_{I/A}$ ($R_{I/A} = 1.2$), the surface is partly covered by non-crystalline Ga droplets. In an intermediate region of $R_{I/A}$, there are a few intensity maxima visible in the diffraction pattern, which indicate the presence of epitaxial w-GaN nanocrystals, with an epitaxial relationship as described before. This means that in principle N_2^+ ions can be used for the deposition of such nanocrystals as well as N^+ ions. Comparing the RHEED patterns here with the patterns in Fig. 5.6 for $E_{kin} = 60$ eV, two differences can be observed: when N_2^+ ions are employed, the ideal $R_{I/A}$ seems to be shifted to higher values and the diffraction pattern is less pronounced.

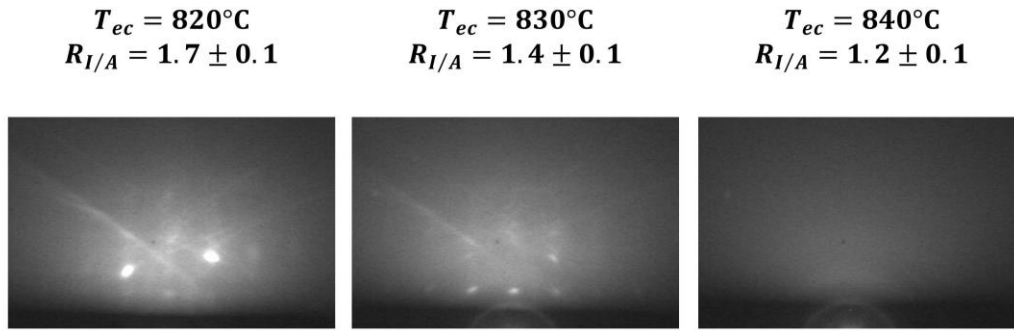


FIG. 5.11: RHEED patterns of GaN nanocrystals [$E_{kin} = (60 \pm 5)$ eV; $j = (0.82 \pm 0.04)$ $\mu\text{A cm}^{-2}$; $T_s = 650^{\circ}\text{C}$] after the post-nitridation deposited using N_2^+ ions. ϕ_{Ga} is increased from the left to the right.

Both could be induced by a smaller arrival rate of N atoms. As shown in section 3, the ion beam profile for N_2^+ ion beams is narrower, i.e. the total ion current on 1 cm x 1 cm, might be smaller as compared to a N^+ ion beam. However, in principle one could expect a larger N concentration on the surface using N_2^+ , because a constant ion current carries twice as much N atoms. It is therefore not straightforward to discuss the differences of the RHEED results here. Though, it is to be noted that the following might also play a role in rendering the crystal growth slower: Assuming that approx. 10 eV are required to dissociate an N_2^+ ion, the dissociated two N particles would have remaining average energies of approx. 25 eV, which is already close to the lower limit of the Brice window as depicted in Fig. 2.5. Presumably, the adatoms are less mobile, because the enhancement of adatom diffusion is less prominent.

5.1.5 Summary

For high substrate temperatures ($T_s = 700^{\circ}\text{C}$), no Ga or GaN deposition could be achieved within reasonable values of ϕ_{Ga} using N^+ ions only. The reason may be a high adatom desorption rate. When $T_s = 650^{\circ}\text{C}$, the adatom desorption rate is smaller and three sample types can be distinguished depending on $R_{I/A}$. For $\phi_{Ga} < \phi_N$, the Ga concentration on the surface is not sufficient for crystal growth; when $\phi_{Ga} \approx \phi_N$, GaN crystal growth can be observed; and when $\phi_{Ga} > \phi_N$, the Al_2O_3 surface is mainly covered by non-crystalline Ga agglomerations. The GaN crystals obtained in the intermediate region of $R_{I/A}$, are wurtzitic, epitaxial and grow 3-dimensionally. The orientation of the crystals is with the w-GaN(11 $\bar{2}$ 0)-plane being parallel to the interface, the nanocrystals are therefore non-polar. The lateral dimension of the nanocrystals is a few 10 nm and the height several nm. The area density of nanocrystals may be as large as $1.5 \cdot 10^{10} \text{ cm}^{-2}$. Due to a high lattice mismatch along $\text{Al}_2\text{O}_3[11\bar{2}0]$, a defect-rich, disturbed layer with a thickness of a few nm close to the interface can be observed. Moreover, a tilt of the crystals around w-GaN[0001] is

present. For the dependency of the kinetic energy, it was found that using N^+ ions for $E_{kin} = 60$ eV, the best results in terms of yield can be obtained. The reasons for a deterioration of the yield at higher energies may be sputtering and ion-induced damage formation in the Al_2O_3 substrate. Furthermore, the ideal $R_{I/A}$ shifts to higher values, when the kinetic energy is increased, which suggests that ion implantation effectively reduces the available N concentration on the surface. The deposition of GaN nanocrystals is demonstrated to be also feasible using N_2^+ ions only.

5.2 Growth of GaN thin films

In the previous subsection it was demonstrated that epitaxial GaN nanocrystals could be synthesized using the introduced experimental setup for energy and mass selected IBAD. In the end, the aim of the realization of this setup is the investigation of the influence of ion beam parameters on thin film properties. It is therefore necessary to also evaluate, if compact GaN thin films, which significantly cover the substrate surface, can be deposited. Here, a Kaufman ion source instead of the previously used hollow-anode source, is applied. The substrate temperature of $T_s = 650^\circ C$ was already found to be reasonable for depositing GaN nanocrystals. Thus, this temperature is employed for the depositions presented in the following, too.

5.2.1 Film thickness and deposition rates

The deposition experiments using the Kaufman ion source were carried out under conditions comparable to the previously presented depositions. Fig. 5.12 (a) compares the temporal evolution of RHEED patterns when the hollow-anode source is applied and GaN nanocrystals are synthesized with the case, where the Kaufman ion source is applied. For the two temporal evolutions shown here, the average kinetic energy E_{kin} , the ion-to-atom ratio $R_{I/A}$ and the particle species are identical. As described in section 3, the maximum achievable ion current density is larger by a factor of approx. 2, when the Kaufman ion source is applied. $R_{I/A}$ is to be kept constant, meaning that ϕ_{Ga} is to be increased by a factor of 2, too. In this case, after 2 h of deposition the diffraction pattern of the Al_2O_3 substrate has completely been superseded by a diffraction pattern associated with GaN. Simultaneously, the diffraction pattern is still dominated by the intensity maxima associated with the Al_2O_3 substrate, when the hollow-anode source is applied. Clearly, using the Kaufman ion source the deposition rate could be significantly increased. Comparing the final diffraction patterns after the deposition, it becomes clear that the arrangement of the intensity maxima is the same in both depicted temporal evolutions. This indicates that when the material fluxes are increased, the resulting GaN is also wurtzitic and exhibits the same epitaxial relationship compared to the nanocrystals.

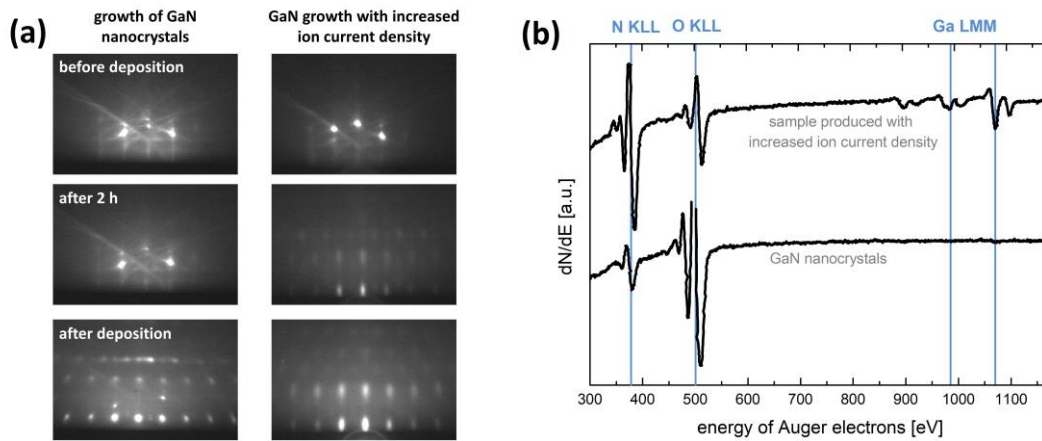


Fig: 5.12: Comparison of GaN nanocrystals deposited using the hollow-anode source and thin films produced with similar parameters (N^+ ions with an average kinetic energy of $E_{kin} = 60$ eV; $R_{I/A} \approx 1.1$) using the Kaufman ion source. The difference is the ion current density being half as high for the GaN nanocrystal sample. In (a) the temporal evolution of the surface structure in the RHEED pattern is compared and in (b) the surface composition as measured by AES.

Though, there are two noticeable differences between the final diffraction patterns. First, the intensity maxima associated with the substrate are still visible when the hollow-anode source is applied, in the other case, however, they have vanished. And second, the intensity maxima are point-like when the hollow-anode source is applied and to a certain extent elongated when the Kaufman ion source is applied. It can therefore be assumed that increasing the material fluxes by a factor of 2, significantly increases the deposition rate of crystalline GaN. Moreover, the growth mode can still be characterized as 3-dimensional. Though, the elongation of the intensity maxima indicates a tendency to a 2-dimensional growth. In order to complement this comparison, the surface composition as examined by AES in Fig. 5.12 (b) can also be considered. The peaks associated with the Auger electron transitions in both N and Ga atoms become more intense in relation to the peak associated with the O Auger electron transition, when the Kaufman ion source is applied instead of the hollow-anode source. It is evident also from the AES that the area density of Ga and N on the surface is larger, when increased material fluxes are applied.

As the observations made by RHEED and AES suggest significant changes in terms of surface coverage and deposition rate, it is reasonable to quantify the coverage of the Al_2O_3 substrate and possibly determine film thicknesses. Fig. 5.13 depicts exemplary plots of XRR measurements. The depositions were assisted by both N^+ and N_2^+ ion irradiation. For all of the plotted XRR measurements, Kiessig fringes are observable. This means that for these samples a GaN film thickness can be determined. In order to do so, for each of these examples a simulated function is plotted in Fig. 5.13. This function was determined with the software IMD [Win98].

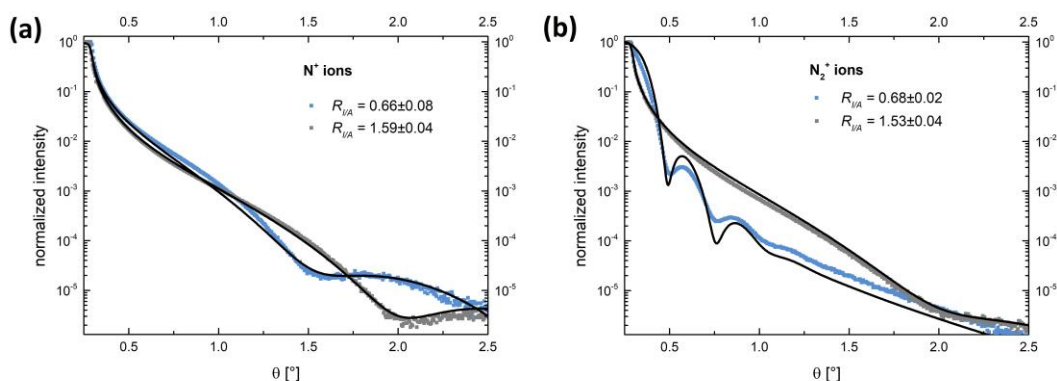


FIG. 5.13: Exemplary XRR measurements with the corresponding simulated curves in black in the case that (a) the deposition process is assisted with N^+ ions and (b) the deposition process is assisted with N_2^+ ions. The film thicknesses corresponding to the simulated functions are $d = 3$ nm and $d = 2.3$ nm in (a) and $d = 13$ nm and $d = 2.3$ nm in (b).

For all simulated functions, Cu K_α radiation is assumed ($E = 8.048$ keV), the angular resolution of the diffractometer is assumed to be $\Delta\theta = 0.01^\circ$ and the mass density of the Al_2O_3 substrate to be $\rho(Al_2O_3) = 3.98$ g cm^{-3} [Liu02]. The remaining parameters that are included in the simulated functions are listed in table 5.1. The film thickness d in three cases is 2 nm $< d < 3$ nm. One plotted XRR curve (N_2^+ ; $R_{I/A} = 0.7$) stands out with a comparably high film thickness of $d = 13$ nm. In this XRR curve, Kiessig fringes are already observable for angles of $\theta < 1^\circ$. The mass density of bulk GaN is $\rho(GaN) = 6.15$ g cm^{-3} [Mor08]. The mass densities of the thin film as used for the simulated curves are 5.7 g $cm^{-3} < \rho < 6.5$ g cm^{-3} , hence in agreement with the mass density of GaN. Assuming that the ion irradiation with $E_{kin} < 100$ eV does not induce changes of the roughness of the Al_2O_3 substrate, the interface roughness as determined by XRR should be similar to the roughness of the substrate that was determined by AFM. The RMS roughness of the Al_2O_3 substrate surface was previously determined by AFM to be 0.1 nm on an area of $2 \mu m \times 2 \mu m$. This value is in fact similar to the interface roughness values obtained from the simulated curves. These are between 0.1 nm $< RMS_{interface} < 0.33$ nm. The XRR curves contain information about a several orders of magnitude larger sample surface compared to typical AFM measurements; it is therefore consistent to find that the interface roughness determined by XRR tends to be larger. The surface roughness of the thin films as obtained from the simulated curves is clearly larger than the interface roughness.

Table 5.1: Simulation parameters for the four exemplary XRR curves shown in Fig. 5.12. The simulated curves were generated using the IMD software [Win98].

Particle species	I/A ratio	Thickness [nm]	Density [g cm^{-3}]	Surface roughness [nm]	Interface roughness [nm]
N^+	0.7	3	6.2	0.45	0.3
	1.6	2.3	6.1	0.42	0.1
N_2^+	0.7	13	6.5	1.9	0.3
	1.5	2.3	5.7	0.45	0.33

Particularly for a larger film thickness ($d = 13$ nm), the surface roughness is comparably high with $RMS = 1.9$ nm. This corresponds to the growth mode being mainly 3-dimensional as deduced from the RHEED patterns e.g. in Fig. 5.12 (a). The thickness of typical GaN thin films that were deposited using the Kaufman ion source as determined from XRR are summed up in Fig. 5.14. The film thickness is plotted in dependence of $R_{I/A}$. If N_2^+ ions are employed, the GaN film thickness increases with decreasing $R_{I/A}$. This result suggests that the deposition rate is limited by the Ga flux ϕ_{Ga} . Even thicker films could therefore be expected if $R_{I/A}$ is decreased further. Though, for $R_{I/A} \ll 1$, the formation of Ga droplets sets in and at some point the surface might be covered by such Ga droplets as shown in subsection 5.1. Hence, even if the deposition rate is limited by ϕ_{Ga} , it is assumed that for a significant increase in deposition rate both ϕ_{Ga} and j are to be increased. In Fig. 5.14 (b) it can be discerned that for $R_{I/A} \approx 1$, the material fluxes were varied. The ion flux was reduced from $\phi_N^+ = 1.7 \times 10^{13} \text{ s}^{-1} \text{ cm}^{-2}$ down to $\phi_N^+ = 0.5 \times 10^{13} \text{ s}^{-1} \text{ cm}^{-2}$. This can be done e.g. by defocusing the ion beam. When decreasing both material fluxes, by a factor of 3.4, the film thickness decreases by a factor of 5.9. It can also be seen that varying the average kinetic energy between $E_{kin} = 60$ eV and $E_{kin} = 80$ eV does not significantly affect the film thickness, when the material fluxes are identical. This confirms that the film thickness can most readily be controlled by simultaneous variation of both material fluxes. As a consequence, the maximum obtainable film thickness would be limited by the restrictions described in section 3.

In the case that N^+ ions are employed, the GaN films also tend to be thicker for smaller $R_{I/A}$. However, the deviations in film thickness are less prominent. For an ion flux of $\phi_N^+ = 1 \cdot 10^{13} \text{ s}^{-1} \text{ cm}^{-2}$, the average value for the film thickness is $d = 2.7$ nm with a standard deviation of $\Delta d = 0.4$ nm. For an ion flux of $\phi_N^+ = 1.7 \cdot 10^{13} \text{ s}^{-1} \text{ cm}^{-2}$, it is $d = 4.1$ nm with a standard deviation of $\Delta d = 1.6$ nm. The film thickness varies only to a small extent, in the case that ϕ_{Ga} is changed (i.e. $R_{I/A}$ is changed in Fig. 5.14 (a)).

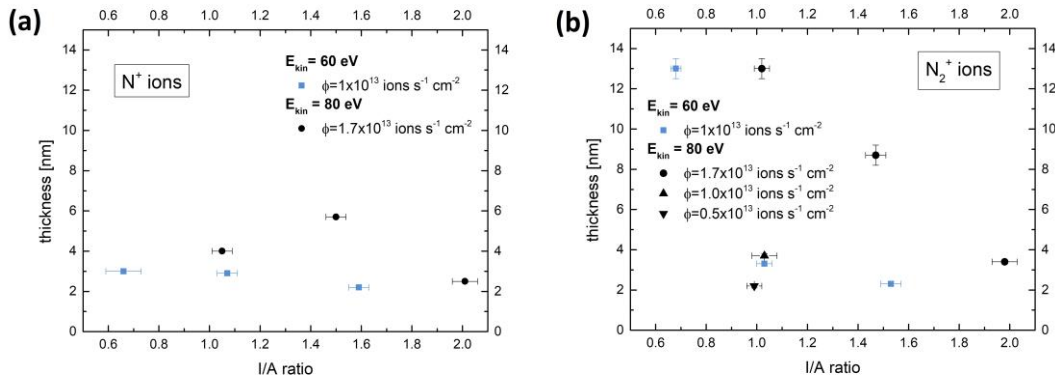


FIG. 5.14: The film thicknesses determined by XRR and plotted in dependence of $R_{I/A}$. The film thickness is plotted for both (a) N^+ ions and (b) N_2^+ ions. The applied average kinetic energies as well as ion fluxes can be drawn from the inscription.

However, if both material fluxes are increased (from blue points to black points in Fig. 5.14 (a)), the film thickness increases. This suggests that in contrast to film growth assisted by N_2^+ ion irradiation, here the deposition rate is limited by the ion current density j . Note that N^+ ions transport half as much mass compared to N_2^+ ions, if the ion current density is identical. It is therefore plausible, that the deposition rates significantly differ and different parameters have a limiting influence, if the growth is assisted either by N^+ or by N_2^+ ion irradiation with the same ion current density. Furthermore, the maximum achieved film thickness using N^+ irradiation assisting the growth is $d = 5.7$ nm, while it is $d = 13$ nm using N_2^+ irradiation. Correspondingly, the maximum achievable deposition rates are $r = 1$ nm h⁻¹ and $r = 2.4$ nm h⁻¹, respectively. The factor between these two deposition rates or thickness values corresponds to the ratio of mass transported per measured impinging ion.

In order to grow GaN films with a large thickness, not only the material fluxes play a role, but also the the number of atoms that are incorporated in the GaN thin film as fractions of the number of atoms provided during the growth by the Ga flux and the N ion beam. Table 5.2 lists this quantity for exemplary samples. The provided number of Ga and N atoms is derived from the material fluxes and the deposition time. Note that all samples are exposed to the N ion beam 30 min longer than to the Ga flux. The area density of incorporated Ga atoms n_{Ga} is assumed to be equal to the area density of incorporated N atoms n_N , since GaN films have a stoichiometry of 1:1. Consequently, the area density is calculated according to

$$n_{Ga} = n_N = \frac{\rho(\text{GaN})d}{M(\text{Ga})+M(\text{N})}, \quad (5.1)$$

where $M(\text{Ga})$ and $M(\text{N})$ are the atomic masses of Ga and N. For the films with $d = 13$ nm, approximately every fifth atom (of both Ga and N) is incorporated in the GaN film. Considering reflection of ions, desorption of atoms and possibly also sputtering, this is a satisfactory fraction. However, for the thinner films, the fraction of incorporated atoms obviously is much smaller. As listed in table 5.2, it is between 2% and 10%. If less than every tenth atom contributes to the growth process, this means that there might be possibilities to increase the deposition rate and obtain a larger film thickness without necessarily increasing the material fluxes. In this context, two parameters are to be mentioned. The deposition temperature has an impact on desorption processes, diffusion behavior of adatoms and could therefore have an improving influence on the deposition rate. Furthermore, the fraction of incorporated atoms might also be substrate-dependent. A different substrate material might promote thin film growth with a larger deposition rate, e.g. if the combination of the interface energies and the lattice mismatch are more appropriate.

Table 5.2: Four exemplary samples, for which the number of N and Ga atoms incorporated in the GaN thin film was calculated as fraction of the provided number of N and Ga atoms. For all listed samples the applied kinetic energy was $E_{kin} = 60$ eV.

Particle species	I/A ratio	Provided Ga atoms [10^{17} cm $^{-2}$]	Provided N atoms [10^{17} cm $^{-2}$]	Thickness [nm]	Incorporated Ga atoms [%]	Incorporated N atoms [%]
N $^{+}$	0.7	2.6	1.9 \pm 0.2	3	5.2	7.2 \pm 0.7
N $_2^{+}$			3.8 \pm 0.1	13	22.3	15.0 \pm 0.4
N $^{+}$	2.0	1.5	3.3 \pm 0.1	2.5	7.4	3.4 \pm 0.1
N $_2^{+}$			6.5 \pm 0.2	3.4	10.1	2.3 \pm 0.1

5.2.2 Characterization of crystal structure by X-ray diffraction

After the deposition rates of the setup for energy and mass selected IBA-MBE could be increased and defined film thicknesses could be measured, XRD was applied to investigate the crystal structure. Such an investigation provides information about the epitaxial relationship, crystallite sizes, twist and tilt distribution of crystallites and the relief of in-plane stress. The results presented here, were obtained in depositions using N $_2^{+}$ irradiation with $E_{kin} = (80 \pm 8)$ eV. ϕ_{Ga} and correspondingly $R_{I/A}$ were varied, resulting in a change of film thickness as determined by XRR between $3.4 \text{ nm} < d < 13 \text{ nm}$. The ion current density was $j = (2.60 \pm 0.07) \mu\text{A cm}^{-2}$.

In subsection 5.1.3, an XRD pole figure using the w-GaN{10 $\bar{1}$ 1} reflection was already presented including a calculated pole figure. Fig. 5.15 (a) presents the same kind of measurement for a GaN thin film with $d = 13$ nm. The arrangement of pole density maxima is similar, which indicates that again there is wurtzitic GaN with the same epitaxial relationship. The intensities of the w-GaN pole density maxima as compared to the pole figure measurement of the w-GaN nanocrystals in subsection 5.1.3 are considerably larger here. In contrast to the pole figure of the nanocrystals, the four w-GaN{10 $\bar{1}$ 1} pole density maxima at $\alpha = 40^\circ$ are clearly distinguishable from the Al $_2$ O $_3$ {11 $\bar{2}$ 0} and the Al $_2$ O $_3$ {1 $\bar{1}$ 04} pole density maxima in their vicinity. Apart from this pole figure measurement, a further pole figure measurement is depicted in Fig. 5.15 (b) and a corresponding simulated pole figure in Fig. 5.15 (c). This pole figure was measured for the same GaN thin film but for the w-GaN{10 $\bar{1}$ 3} reflections. The features of this pole figure are similar. The symmetry is also sixfold. Therefore, four pole density maxima are expected at $\alpha = 63^\circ$. In contrast to the previously described pole figure, these four 'inner' pole density maxima do not form a square, but a rectangle facilitating the determination of the epitaxial relationship by regarding only these pole density maxima. Four additional pole density maxima, originating from the remaining two reflections, are expected at $\alpha = 90^\circ$. All 8 pole density maxima are easily discernable in the measured pole figure. Additionally, the pole figure contains several narrow pole density maxima originating from Al $_2$ O $_3$ lattice planes.

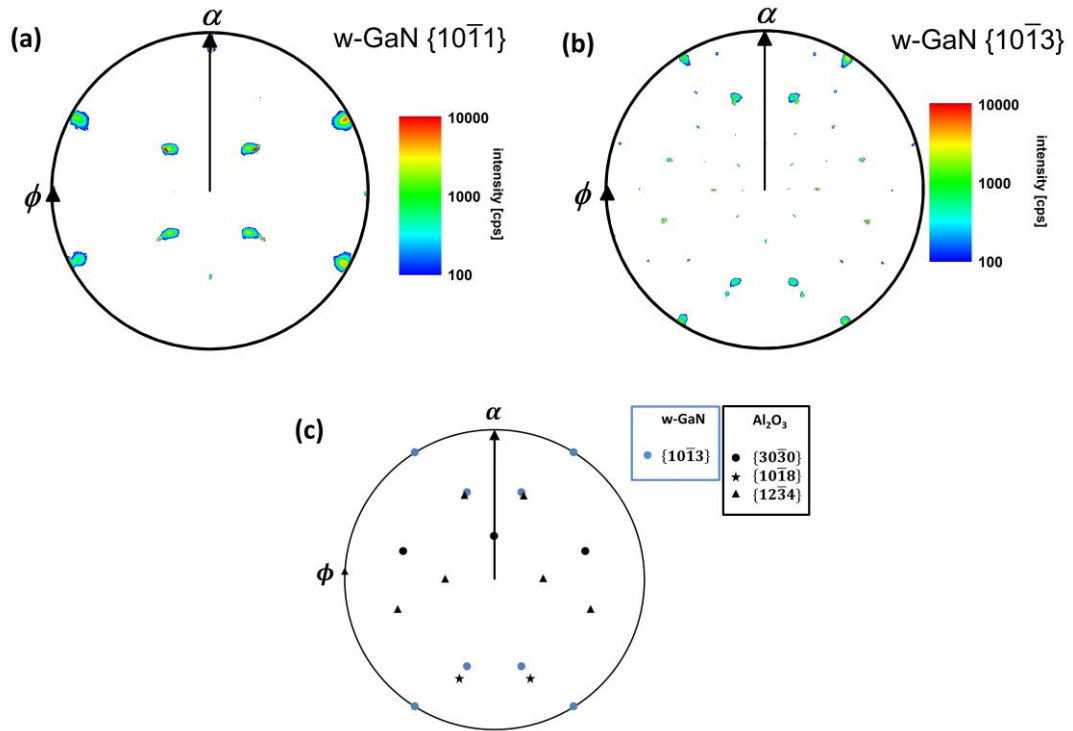


FIG. 5.15: XRD pole figures. (a) and (b) show XRD pole figures that were measured for the w-GaN{10 $\bar{1}$ 1} planes and for the w-GaN{10 $\bar{1}$ 3} planes, respectively. The corresponding GaN thin film with a film thickness $d = 13$ nm was deposited under N_2^+ ion irradiation with $E_{kin} = (80 \pm 8)$ eV. The ion-to-atom ratio was $R_{I/A}=1.0$. A simulation of the measured XRD pole figure in (a) is depicted in Fig. 5.8 (b) and a simulation of the measured XRD pole figure in (b) is depicted in (c). Here, a choice of substrate contributions is included.

In the theoretical pole figure, specific pole density maxima associated with the Al₂O₃{30 $\bar{3}$ 0}, the Al₂O₃{10 $\bar{1}$ 8} and the Al₂O₃{12 $\bar{3}$ 4} lattice planes are included. The Al₂O₃{10 $\bar{1}$ 8} lattice planes have a similar lattice spacing compared to the w-GaN {10 $\bar{1}$ 3} lattice planes ($\Delta(2\theta) \approx 2^\circ$ with Cu K α radiation). If the W L α contributions of the Al₂O₃{30 $\bar{3}$ 0} and the Al₂O₃{12 $\bar{3}$ 4} pole density maxima are taken into account, all four lattice planes can be measured within a range of approx. $\pm 2^\circ$ in 2θ . Agreement can be found between the measured and the simulated pole figure, which again confirms the epitaxial relationship.

Fig. 5.16 (a) presents a $2\theta/\omega$ measurement of a GaN thin film measured in a wide angular range $20^\circ < 2\theta < 70^\circ$. Since this method is sensitive only to lattice planes parallel to the sample surface, the Al₂O₃(1 $\bar{1}$ 02) lattice planes cause a peak in this spectrum, which is located at $2\theta = 25.6^\circ$. The corresponding second order reflection consequently appears in this spectrum at $2\theta = 52.6^\circ$. Both of these substrate peaks are asymmetrical because of the W L α contribution to the spectrum. Also the Cu K β radiation causes a satellite peak for each of the two substrate peaks. The applied graphite monochromator only reduces the intensity of both the W L α and the Cu K β radiation.

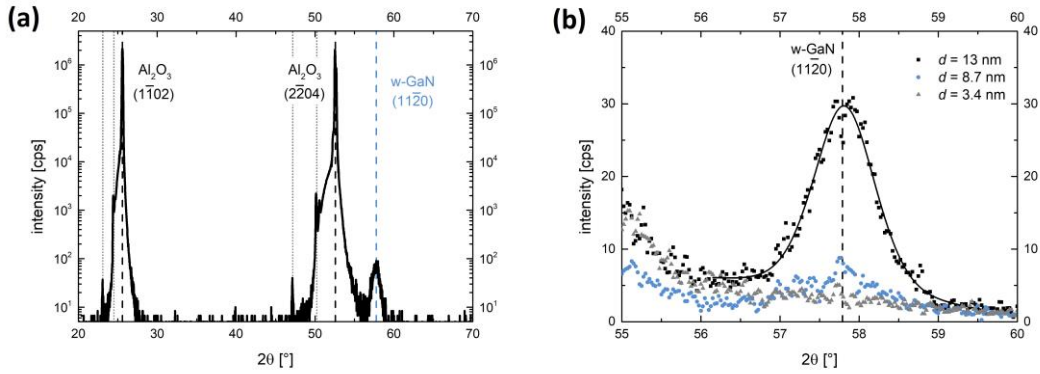


FIG. 5.16: (a) A $2\theta/\omega$ measurement of a GaN thin film with a film thickness $d = 13$ nm that was deposited under N_2^+ ion irradiation with $E_{kin} = (80 \pm 8)$ eV. The ion-to-atom ratio was $R_{I/A}=1.0$. The expected peak positions are indicated by vertical lines. For the two substrate reflections, the contributions of Cu K_β and the W L_α radiation are visualized by two grey dotted lines each. (b) $2\theta/\omega$ XRD measurements depicted in a narrow angular range around the position of the w-GaN(11 $\bar{2}$ 0) reflection. The depositions were carried out under N_2^+ ion irradiation with $E_{kin} = 80$ eV. The film thickness was varied by changing ϕ_{Ga} and correspondingly $R_{I/A}$.

The only GaN-related peak for the determined crystal orientation that can be expected in a $2\theta/\omega$ XRD spectrum in this range (see e.g. [Cra02]), originates from the w-GaN(11 $\bar{2}$ 0) lattice planes. On a logarithmic scale, this peak is indeed observable. Fig. 5.16 (b) shows that in the vicinity of the second order substrate reflection the expected w-GaN(11 $\bar{2}$ 0) reflection ($2\theta = 57.77^\circ$) is present. Here, measurements for three different film thicknesses (and $R_{I/A}$ correspondingly) are plotted. For the film thickness $d = 3.4$ nm, there is no such peak observable. For the film thicknesses $d = 8.7$ nm, it is slightly visible, while for $d = 13$ nm the peak is distinct and in the expected position. The fit for this latter peak reveals a FWHM of 0.94° . Scherrer's formula relates the FWHM of a peak in a $2\theta/\omega$ scan to the size of crystallites d_{crys} perpendicular to the measured lattice planes as [Cul01]

$$d_{crys} = \frac{K\lambda(\text{Cu } K_\alpha)}{\text{FWHM } \cos(\theta)}. \quad (5.2)$$

K is a shape factor and can be approximated as $K = 1$. In this case $d_{crys} \approx 10$ nm is obtained, which is consistent with the film thickness obtained by XRR. In addition to the loss in intensity with decreasing film thickness, the $2\theta/\omega$ peaks originating from the GaN films are correspondingly expected to broaden. Consequently, the peaks are increasingly difficult to observe, for the thinner films. However, for at least two cases, $2\theta/\omega$ XRD peaks are observable, which enables the measurement of XRD rocking curves. For measuring XRD rocking curves of non-polar GaN thin films it was already observed that particularly their width may depend on the rotational position of the sample (φ position) [Kyu09]. Fig. 5.17 (a) therefore depicts two XRD rocking curves measured for the GaN film with $d = 13$ nm, where the rotational position of the sample during the measurement differs by 90° .

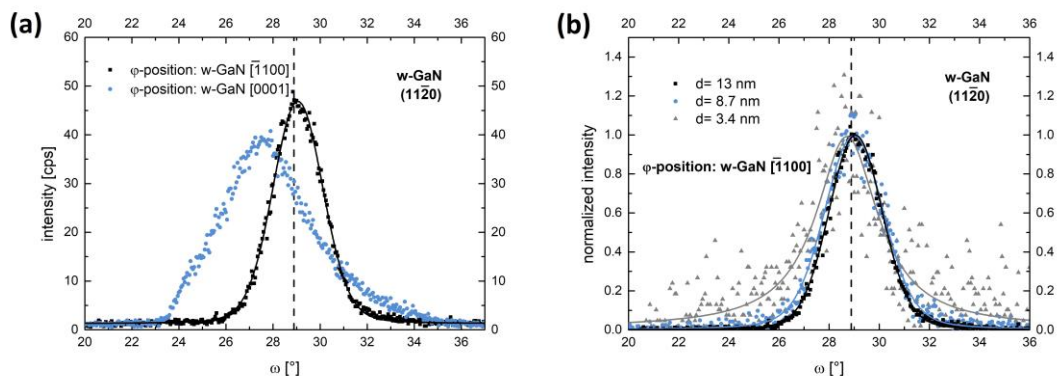


FIG. 5.17: (a) XRD rocking curves measured after GaN deposition under N_2^+ ion irradiation with $E_{kin} = (80 \pm 8)$ eV. The ion-to-atom ratio was $R_{I/A}=1.0$ and the resulting film thickness $d = 13$ nm. The measurements were carried out for two different representative in-plane rotations of the sample (ϕ positions). (b) Three normalized XRD rocking curve measurements with the in-plane rotation as labelled. The depicted curves represent thin films that were deposited under N_2^+ ion irradiation with $E_{kin} = (80 \pm 8)$ eV. The film thickness was varied by changing ϕ_{Ga} and correspondingly $R_{I/A}$.

Clearly, also here the XRD rocking curve depends on the rotational direction and different results may be obtained depending on whether the crystal tilt around w-GaN[0001] or w-GaN[$\bar{1}100$] is regarded. For the case that $\phi \parallel$ w-GaN[$\bar{1}100$], a comparably narrow, symmetric rocking curve can be measured, whereas the rocking curve is broadened and shifted for $\phi \parallel$ w-GaN[0001]. Even though the precise dependencies are not known, strain relief and basal plane stacking faults are mentioned as possible reasons for a broadening of the rocking curve measured along w-GaN[0001] [Mor09]. In the following, the focus is put on the XRD rocking curve measured with $\phi \parallel$ w-GaN [$\bar{1}100$]. Reports of the FWHM of the rocking curve measured along this direction vary depending on the details of the deposition process. For films with a much higher thickness (a few μm) this width may vary between 0.1° and 0.8° [Oeh14]. A shift of the position of the rocking curves depending on the rotational sample position was observed by the same authors, too. Here, the samples were carefully aligned such that the $\text{Al}_2\text{O}_3(1\bar{1}02)$ plane lies in the horizontal plane. A possible reason for the shifted rocking curve is a misalignment of the w-GaN($11\bar{2}0$) planes with the horizontal and the $\text{Al}_2\text{O}_3(1\bar{1}02)$, correspondingly. In Fig. 5.17 (b), the normalized rocking curves for different film thicknesses are plotted. For the film thicknesses $d = 8.7$ nm and $d = 13$ nm, the FWHM as obtained from the fit function are $(2.80 \pm 0.03)^\circ$ and $(2.53 \pm 0.01)^\circ$, respectively. For the GaN film with $d = 3.4$ nm, the signal-to-noise ratio is comparably small. However, a peak is clearly present and the fit function reveals a FWHM of $(3.01 \pm 0.20)^\circ$. These values are approximately one order of magnitude larger than those reported for μm -thick GaN films. This indicates that the distribution of crystallite tilts is comparably broad. However, the tendency clearly shows that the thicker the films get, the narrower is the XRD rocking curve. Employing ion-beam nitridation of Ga droplets, rough non-polar GaN thin films with thicknesses of up to approx. 50 nm and rocking curve FWHM of 1.12° were reported

[Pop15]. This is the same order of magnitude compared to the measured values here. It is possible that the main reason for the large differences in the rocking curve FWHM to reported values is the film thickness and relaxation mechanisms, which have not fully taken place yet. Note that it may be possible to obtain narrower crystal tilt distributions, when the used kinetic energy is further optimized.

In order to complete the investigations of these GaN thin films in terms of XRD, in-plane measurements were carried out. In the previously presented out-of-plane XRD measurements in some cases, the signal was small compared to the noise level. The $2\theta_\chi/\varphi$ scan is the in-plane analogue to the $2\theta/\omega$ scan. The benefit of XRD in-plane measurements is the lower penetration depth of the radiation and thereby the higher surface sensitivity. Fig. 5.18 (a) contains plots of the $2\theta_\chi/\varphi$ XRD scans of the samples, where initially (for $2\theta_\chi = 0$) $\varphi \parallel$ w-GaN $[\bar{1}100]$. Indeed, the intensity is sufficiently high to yield a clearly observable peak even for a GaN film with $d = 3.4$ nm. The parameters of the corresponding fit functions are listed in table 5.3. The width of the peak can be used – in a manner similar to the out-of-plane case - to estimate the size of the GaN crystallites along the w-GaN $[\bar{1}100]$ -direction (eq. (5.2)). This crystallite size increases with increasing film thickness. For $d = 3.4$ nm, the crystallite size is even larger than the film thickness, indicating a high lateral growth velocity in the very early stage of the growth. For larger film thicknesses, the crystallite size as determined is similar to the film thickness. Another striking feature, which is observable in the $2\theta_\chi/\varphi$ scans, is related to the peak position. Obviously, for the film with $d = 3.4$ nm the peak is shifted to a larger $2\theta_\chi$ angle. The lattice mismatch along the w-GaN $[\bar{1}100]$ -direction is relatively high (15%) with Al₂O₃ possessing the smaller distance between neighboring atoms along that direction. It is therefore consistent that in an early stage of the growth the peak in the $2\theta_\chi/\varphi$ scan is shifted to higher angles. This implies that a relaxation mechanism has set in for larger d and the in-plane stress in the thin film is reduced with increasing film thickness. The peak position of the w-GaN($\bar{1}100$) lattice planes is expected to be $2\theta_\chi = 32.39^\circ$. For films with $d = 8.7$ nm and $d = 13$ nm, the corresponding peak positions are closer to the relaxed position, however, there is a small shift to higher angles left, indicating that in-plane stress is still present to a certain extent. The normalized φ scans for these $2\theta_\chi/\varphi$ peaks are plotted in Fig. 5.18 (b) as in-plane analogue to the out-of-plane XRD rocking curve. The widths of these scans contain information about the twist of the GaN crystals. The FWHM of the φ scans is approx. 2° . In literature, an exemplary value for the FWHM of the φ scan of the w-GaN($\bar{1}100$) reflections in (11 $\bar{2}0$)-oriented w-GaN of 1.35° can be found [Cha06]. Again, this is for μm -thick films, which hinders a direct comparison to the values obtained here. However, it is to be noted that the order of magnitude is the same and therefore the twist distribution is not drastically different from what this group reported. The FWHM values of the measured φ scans indicate that the GaN crystals are to a similar extent twisted as they are tilted.

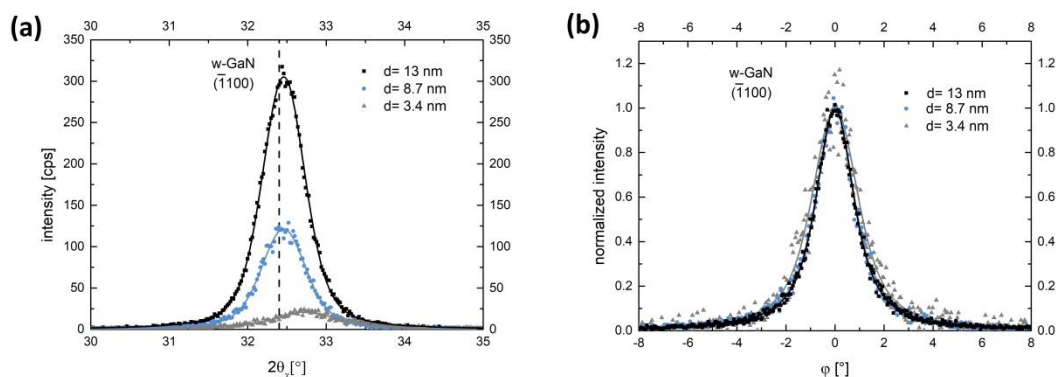


FIG. 5.18: (a) $2\theta_\chi/\phi$ measurements for the w-GaN ($\bar{1}100$) plane. The three depicted curves represent GaN thin films deposited under N_2^+ ion irradiation with $E_{kin} = (80 \pm 8)$ eV. The film thickness was varied by changing ϕ_{Ga} and correspondingly $R_{I/A}$. (b) normalized ϕ scans for the scans in (a).

A relaxation process, which was found considering the $2\theta_\chi/\phi$ peak positions and the rocking curve widths, can also be observed here. The FWHM of the ϕ scans and accordingly the width of the crystal tilt distribution apparently decreases with increasing film thickness.

5.2.3 Surface topography and microstructure

In this subsection, the surface topography as measured by AFM is characterized and the microstructure as measured by HRTEM. Fig. 5.19 presents a compilation of AFM images. The depositions were assisted by ion irradiation with $E_{kin} = (60 \pm 15)$ eV and $j = (1.51 \pm 0.15)\mu A cm^{-2}$. The used ion species was varied as well as $R_{I/A}$. For depositions assisted by N^+ irradiation, the resulting GaN films are relatively thin. Correspondingly, the surface appears smooth in the depicted AFM images. However, the RMS roughness is $RMS = 0.5$ nm and $RMS = 0.4$ nm and therefore significantly larger than the roughness of the Al_2O_3 substrate. Furthermore, the surface topography appears isotropic and there is no pronounced structure standing out. The growth mode was already characterized as predominantly 3-dimensional. It is therefore consequential that the thicker films deposited under N_2^+ irradiation exhibit a larger surface roughness. For a film thickness $d = 3.3$ nm, the RMS roughness is $RMS = 0.6$ nm, which is slightly larger compared to the films deposited under N^+ irradiation.

Table 5.3: Fit parameters of XRD in-plane measurements shown in Fig. 5.18. The crystallite size is the in-plane coherence length of crystallites as calculated from eq. (5.2).

Film thickness [nm]	FWHM of $2\theta_\chi/\phi$ peak [°]	crystallite size [nm]	Position of $2\theta_\chi/\phi$ peak [°]	FWHM of ϕ scan [°]
3.4	0.99 ± 0.09	8.4	32.74 ± 0.01	2.28 ± 0.04
8.7	0.68 ± 0.01	12.2	32.46 ± 0.01	1.90 ± 0.02
13	0.65 ± 0.01	12.7	32.46 ± 0.01	1.87 ± 0.01

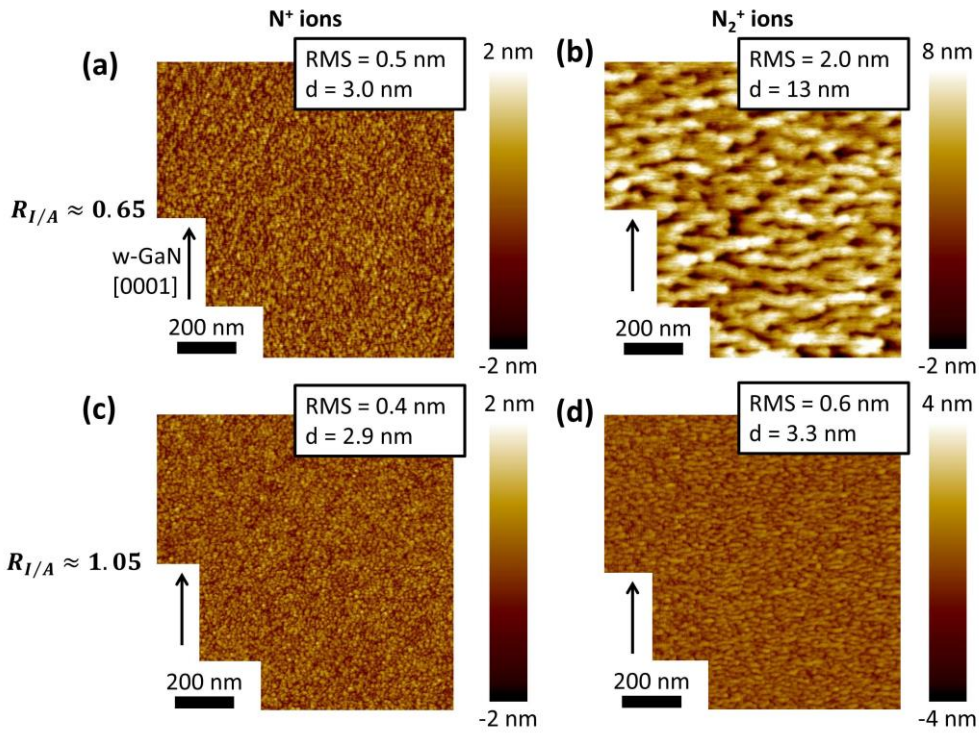


FIG. 5.19: AFM images with w-GaN [0001] from the bottom to the top as indicated by the black arrows. The depositions were assisted by ion irradiation with $E_{kin} = (60 \pm 15)$ eV and $j = (1.51 \pm 0.15)\mu\text{A cm}^{-2}$. For the measurements shown in (a) and (c), the deposition was assisted by N^+ irradiation, in (b) and (d) by N_2^+ irradiation. $R_{I/A} = 0.7$ for the measurements shown in (a) and (b), and $R_{I/A} = 1.1$. The corresponding film thickness d and the roughness RMS are given in the white boxes.

Though, there is another difference. In Fig. 5.19 (d), it is already observable that the surface structures are not isotropic anymore. While for the AFM images presented in Fig. 5.19 (c) the structures are mainly circular, here they are clearly elongated. Note that the elongation of the GaN crystals is not in an arbitrary direction, but along w-GaN $[\bar{1}100]$. The observation of both increasing surface roughness and the evolution of elongated GaN crystals is heightened for the film with $d = 13$ nm. The observed anisotropy of the GaN crystals can be characterized by means of the autocorrelation function (see eq. (4.7)). The autocorrelation as a 2-dimensional function contains direction-dependent information about correlation lengths, i.e. the average lateral dimension of structures on the surface and also average separations of repeating structures. In Fig. 5.20 for two different film thicknesses, two cross-sections of the autocorrelation are depicted each, one of which parallel to w-GaN $[\bar{1}100]$ and the other one parallel to w-GaN[0001]. The surface anisotropy becomes obvious here because the autocorrelation along these two directions behaves differently. It is easily discernable that the center peak is broader along w-GaN $[\bar{1}100]$. The FWHM of the Gaussian fit function of these center peaks are listed in table 5.4. For the thinner GaN film it is broader by a factor of approx. 2, for the thicker even by a factor of 3. This implies that the height is correlated over larger distances along w-GaN $[\bar{1}100]$ than along w-GaN[0001].

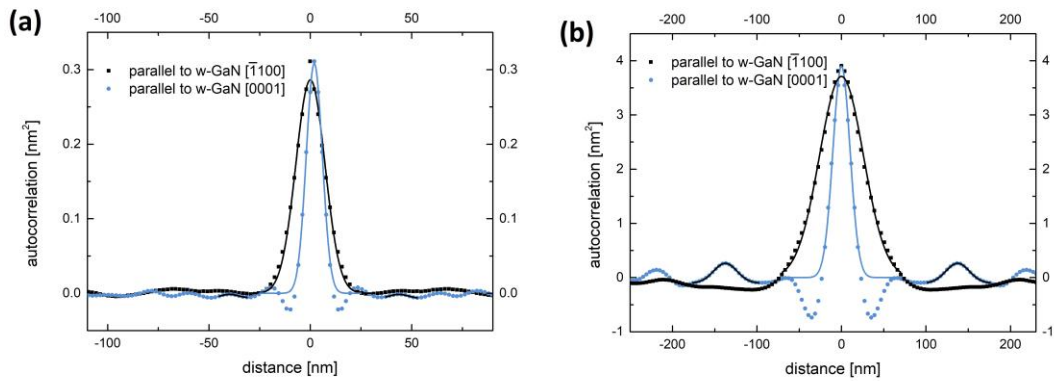


FIG. 5.20: Autocorrelation function as determined for two different surface topographies and two directions, each (a) for the topography as shown in Fig. 5.19 (d) [N_2^+ , $E_{kin} = (60 \pm 15)$ eV, $j = (1.51 \pm 0.15)\mu\text{A cm}^{-2}$, $R_{I/A} = 1.1$] and (b) for the topography shown in Fig. 5.19 (b) ($R_{I/A} = 0.7$, otherwise same parameters). Data obtained from the AFM measurements is depicted as dots, fit functions as continuous lines

The reason for the occurrence of this anisotropy is a preferred and therefore faster growth in the w-GaN $[\bar{1}100]$ direction. The difference in lateral growth velocity of the GaN crystals might be related to the anisotropy of the lattice mismatch. The observation here is that the preferred growth direction simultaneously is the direction of the larger lattice mismatch. This is reasonable considering that the crystal planes perpendicular to the direction of the larger lattice mismatch appear less strained. The attachment of adatoms to such crystal planes is assumed to be favorable. For growth in the direction perpendicular to the direction of the smaller lattice mismatch, the relevant lattice planes can be assumed to contain more strain, which may hinder a fast lateral growth. A second difference between the autocorrelation functions along the two directions lies in the occurrence of further local maxima and minima. Along w-GaN $[0001]$ in both directions from the main peak first a distinct minimum arises and subsequently a maximum, while along the w-GaN $[\bar{1}100]$ this is not readily observable. These minima and maxima appear periodically along w-GaN $[0001]$ and also in larger distances from the main peak. The second maxima on both sides of the main maximum were fitted using Gaussian functions as indicated by the black curves in Fig. 5.20. The distance of the center of these two Gaussian functions is divided by 4 in each case in order to obtain the distance between the maxima in the autocorrelation as listed in table 5.4. The occurrence of these maxima in the autocorrelation demonstrates the periodicity of the surface topography. After a certain distance in w-GaN $[0001]$ a correlation of the height is found, which can be used to characterize the average distance between the center positions of the 3-dimensionally grown GaN crystals along that direction. Comparing the two samples it is noticeable that the FWHM of the center peaks and thereby the correlation lengths increase with increasing film thickness due to the presence of lateral growth of the crystals.

5.2 Growth of GaN thin films

Table 5.4: Fit parameters of the autocorrelation functions depicted in Fig. 5.19. Those fit parameters are the FWHM of the main peaks in two perpendicular directions as well as the separation of the periodically appearing maxima in the autocorrelation along w-GaN [0001].

Film thickness [nm]	FWHM of AC peak w-GaN [0001] [nm]	FWHM of AC peak w-GaN [$\bar{1}100$] [nm]	separation of AC-maxima along w-GaN [0001][nm]
3.3	9.3±0.1	16.9±0.4	20.9±0.1
13	23.9±0.6	61.3±0.7	68.7±0.1

The different lateral growth velocities as mentioned before cause the correlation lengths to increase with different rates depending on the crystal direction. Increasing the film thickness from $d = 3.3$ nm to $d = 13$ nm, the correlation length increases by a factor of 2.6 ± 0.2 along w-GaN [0001] and by a factor of 3.6 ± 0.1 along w-GaN [$\bar{1}100$]. As a consequence the ellipticity of the crystalline GaN structures increases.

The fact, that the surface anisotropies are not observable for N^+ (Fig. 5.19 (c)), but only for N_2^+ ions (Fig. 5.19 (d)), even though the film thickness is nearly constant, suggests that there is a dependence of the ion species and the ion kinetic energy on the lateral growth velocities. Regarding N^+ ions, $E_{kin} = 60$ eV is clearly beyond the Brice window. Thus, adatom mobility is strongly enhanced, while the ion irradiation might also induce displacement of atoms below the first monolayer. For N_2^+ ions, dissociation and consequent division of the kinetic energy on two N particles would enhance adatom mobility to a smaller extent such that other influences like the anisotropic lattice mismatch govern the lateral growth velocities.

Other work groups found the surface topography of (11 $\bar{2}0$)-oriented w-GaN grown on (1 $\bar{1}02$)-oriented Al_2O_3 to consist of elongated stripes, too [Zhu07, Li04]. In contrast to the surface topographies characterized here, the stripes reported about by those groups are aligned with w-GaN[0001]. Supposedly, the growth rate is larger along w-GaN[0001], because Ga adatoms have larger migration lengths along this direction. The typical w-GaN films in such reports have film thicknesses of a few μm and are therefore not only much thicker, than those that were deposited here, but also completely coalesced. Consequently, for such extremely small film thicknesses, the lattice mismatch, instead of the adatom migration along different w-GaN lattice planes, can be assumed to govern the lateral growth velocities and the evolving surface morphology as described previously. In fact, Ni *et al.* showed that formation of the stripes aligned with w-GaN [0001] cannot be observed before island coalescence significantly sets in, which in their case occurs for film thicknesses of approx. 50 nm [Ni06]. This group also found structures, which were elongated perpendicular to w-GaN[0001] for 3-dimensional growth and a not fully coalesced w-GaN film, similar as in the present case.

Regarding the surface topography, another feature can be observed for GaN films with thicknesses $d > 10$ nm. Fig. 5.21 (a) illustrates the results of an AFM measurement

for an exemplary GaN thin film deposited under N_2^+ irradiation with $E_{kin} = (81 \pm 16)$ eV and $j = (2.60 \pm 0.07) \mu A cm^{-2}$. The ion-to-atom ratio was $R_{I/A} = 1.0$ yielding a film thickness $d = 13$ nm as determined by XRR. This AFM image is dominated by the presence of relatively large mound structures, which are much higher than the film thickness. Similarly as described before, these mounds also exhibit an ellipticity with the longer axis being parallel to $w\text{-GaN}[\bar{1}100]$. Fig. 5.21 (b) is a histogram of the heights that occur in this AFM measurement, where the smallest occurring height is set as zero. A pronounced maximum evolves for $h = 16.3$ nm. This is in agreement with the film thickness as it was determined by XRR. The fact that the film thickness can in principle be deduced from AFM measurements demonstrates that the Al_2O_3 surface is not completely covered. In the histogram, a shoulder on the high-height side of this maximum evolves and ranges to heights of up to $h \approx 30$ nm. Even heights of up to $h \approx 50$ nm are present in this histogram, which represents these mound structures. TEM measurements with a low magnification as depicted in Fig. 5.21 (c) can be compared to this AFM image. Here, regions with a homogeneous film thickness can be found (e.g. on the right hand side), where the film thickness agrees with the film thickness found by XRR and AFM. Apart from these, there are regions, where the already described mounds appear. In the given example the largest mound is 45 nm high. Between such mounds, it is possible to find regions, where the GaN film has a reduced film thickness and where the coverage of the Al_2O_3 substrate is almost interrupted. In order to evaluate the microstructure of the thin GaN films, first the region, in which a thin film with a locally homogeneous thickness can be found, was chosen for TEM measurements.

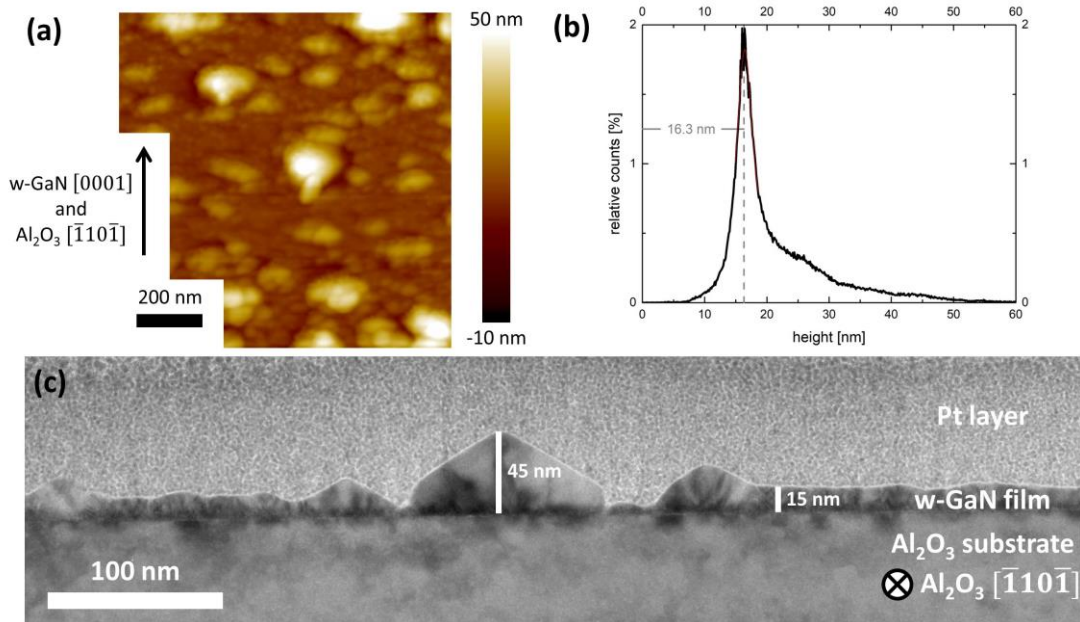


FIG. 5.21: For a GaN thin film [N_2^+ , $E_{kin} = (81 \pm 16)$ eV, $j = (2.60 \pm 0.07) \mu A cm^{-2}$, $R_{I/A}=1.0$] (a) an AFM image, (b) the corresponding histogram of measured heights and (c) a TEM measurement with a relatively low magnification to allow for an overview and for comparison with the AFM measurements.

Starting with Fig. 5.22 (a), a HRTEM measurement of a lamella that was cut along $\text{Al}_2\text{O}_3[\bar{1}10\bar{1}]$ is depicted. The $w\text{-GaN}[0001]$ direction, which is the direction of the comparably small lattice mismatch, lies horizontally within the image plane. Here, the TEM image appears periodic and there is no indication of broad crystallite tilt distributions. Comparably to the microstructure of the nanocrystals, which was presented previously (Fig. 5.10), here the GaN crystal lattice is discernable already from the first monolayer. The interface is undisturbed and therefore, there is no defect-rich layer at the interface observable. With the lamella cut this way, a rectangular symmetry of the crystal lattice is expected as shown in Fig. 5.22 (c). The resolution of the TEM for this kind of measurement is approx. 0.1 nm, while the vertical distance between Ga atoms projected on the image plane is 0.16 nm. A possible reason for the imaged lattice consisting of columns instead of distinct points might be a small crystal tilt around $\text{Al}_2\text{O}_3[\bar{1}10\bar{1}]$. The horizontal distance of the observed columns is 0.26 nm, which is consistent with being half the lattice constant along $w\text{-GaN}[0001]$. Fig. 5.22 (d) shows a HRTEM image of a lamella cut along $\text{Al}_2\text{O}_3[11\bar{2}0]$.

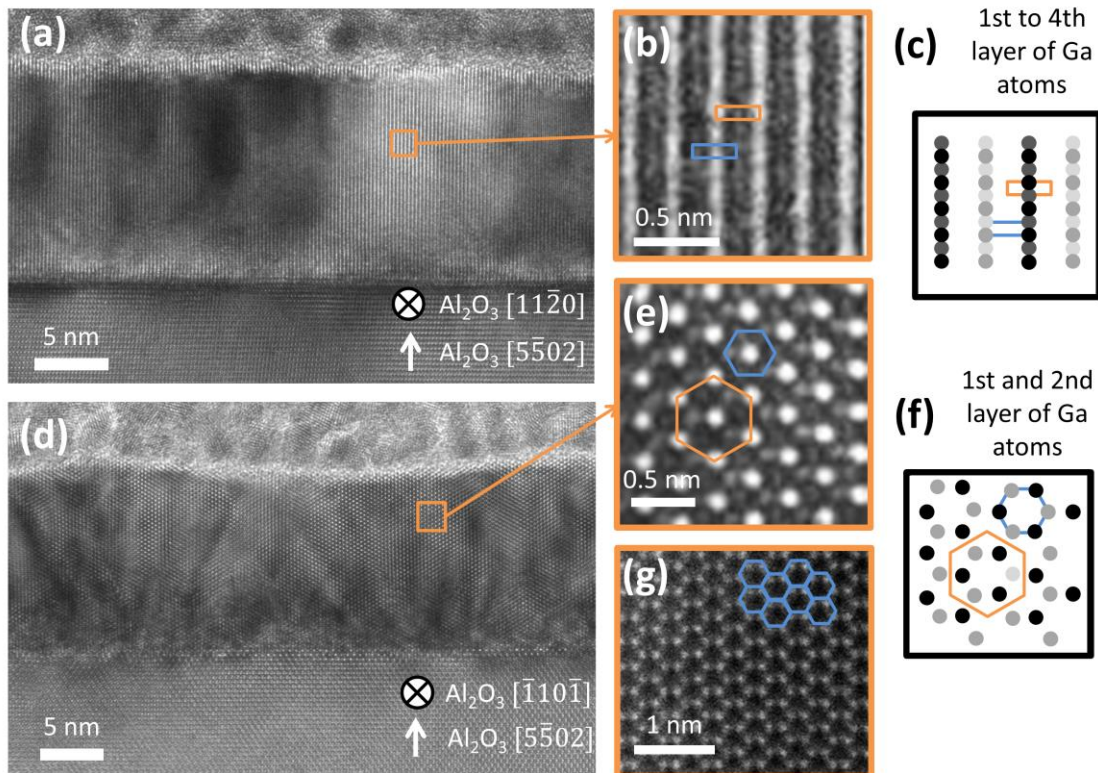


FIG. 5.22: The regarded GaN thin film is the one presented in the previous figure [N_2^+ , $E_{kin} = (81 \pm 16)$ eV, $j = (2.60 \pm 0.07)$ $\mu\text{A cm}^{-2}$, $R_{I/A}=1.0$]. (a) and (d) are HRTEM images taken from two different lamellae, which were cut in perpendicular directions. (b) and (e) are magnifications from (a) and (d) as indicated by the orange squares. (c) and (f) are the expected projections of Ga atom positions in the $w\text{-GaN}$ lattice on the plane, along which the respective lamella was cut. (g) is an ADF-STEM measurement of the lamella presented in (d).

In the depicted region of the lamella the thin film also has a homogeneous thickness corresponding to the film thickness measured by XRR or AFM. In contrast to the previously described lamella, here a defect-rich layer above the interface becomes observable, because the direction with the high lattice mismatch lies horizontally in this image. This defect-rich layer has a thickness of a few nm, as observed previously for the nanocrystal samples, too. Here, the w-GaN[0001] axis is directed into the image plane. Therefore, a hexagonal symmetry is expected. The magnified image in Fig. 5.22 (e) reveals such a hexagonal symmetry. The orange hexagon indicates the symmetry of the intensity maxima in the TEM image. In Fig. 5.22 (f) the positions of the Ga atoms as projected on w-GaN(0001) are visualized. It can be seen that the arrangement of the intensity maxima in the TEM image corresponds to the arrangement of voids in the projection of the crystal lattice on w-GaN(0001). In a phase-contrast TEM image, the position of the atoms is represented by dark spots. Therefore, the blue hexagon indicates the arrangement of Ga atoms in this projection. It can be discerned that also for this arrangement the projection as suggested by Fig 5.22 (f) agrees with the TEM image as shown in Fig. 5.22 (e). Fig. 5.22 (g) depicts an ADF-STEM measurement. Here, z-contrast is responsible for the image formation instead of phase contrast. Therefore, the ADF-STEM image corresponds to the projection of the crystal lattice on w-GaN(0001) as shown in Fig. 5.22 (f) with the intensity maxima representing the projected positions of Ga atoms.

Another striking feature in Fig. 5.22 (d) is the occurrence of inclined lines originating at the defect-rich interface and extending to the surface. These lines are inclined either to the left or to the right with an angle of inclination (angle between the line and the interface) that can be determined to be $(63\pm 3)^\circ$. They only appear in the cross-section with w-GaN[0001] as the viewing direction. Thus, they seem to be confined in the basal plane. Moreover, for the same viewing direction, these lines were not visible for the nanocrystals as presented in section 5.1.3. Sun *et al.* associated the presence of such extended defects with partial dislocations that accompany basal stacking faults [Sun09]. According to this group such basal stacking faults can originate from the coalescence of GaN islands, which would explain that these line defects are not observed in section 5.1.3 for the nanocrystals. The inclination of the partial dislocation lines was also observed by this group. The fast growing facets, e.g. $\{10\bar{1}\bar{2}\}$, which are inclined, correspondingly, are given as a reason for this observation. Furthermore, the confinement of the partial dislocations within the basal plane was also observed by them. Line defects, which are observable in this viewing direction, with an inclination of 60° might also be prismatic stacking faults accompanying basal stacking faults as shown e.g. by Kong *et al.* [Kon12]. For the results presented in this work however, the previously presented XRD rocking curves indicate a comparably broad distribution of the crystallite tilt. For a coalesced thin film this means that the presence of low angle grain boundaries is expected. The observation of the inclined line defects has to be understood in that context. In general, a low angle grain boundary may consist of

dislocations [Got14]. Therefore, the observed inclined line defects may as well indicate the presence of low angle grain boundaries consisting of dislocations.

Finally, the GaN mounds that were observed in Fig. 5.21, are to be examined by HRTEM measurements. Fig. 5.23 (a) is a HRTEM measurement of such a GaN mound with a height in the range of $45 \text{ nm} < h < 50 \text{ nm}$. Since the viewing direction again is $\text{Al}_2\text{O}_3[\bar{1}10\bar{1}]$ and $w\text{-GaN}[0001]$, respectively, the inclined line defects are visible again. Moreover, the shape of the mound reveals the hexagonal symmetry with the growth fronts being e.g. $w\text{-GaN}\{10\bar{1}\bar{2}\}$ [Sun08]. For the FFT, the arrangement of intensity maxima as shown in Fig. 5.9 (e) is expected. The three different FFT images that are presented in Fig. 5.23 all match this expectation. However, there are some differences between the three FFT images. Fig. 5.23 (d) is obtained from a region close to the interface. When compared to the other two images that were obtained in larger distances from the interface, the intensity maxima are found to be broadened, blurred and less well-defined. This reflects the defect-rich, near-interface layer, which was mentioned previously to appear for this viewing direction. Fig. 5.23 (c) and (e) are obtained from regions that are at approximately the same distance from the interface. The two FFTs are obtained for the left hand side and the right hand side of the GaN mound, respectively.

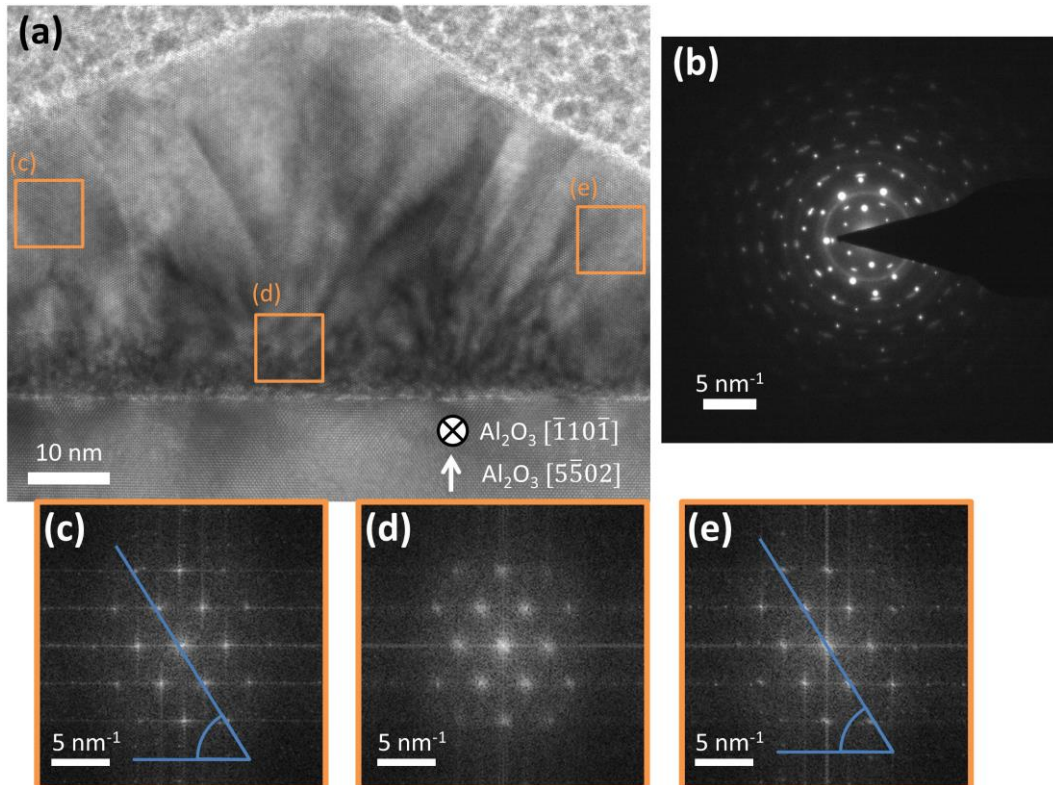


FIG. 5.23: The regarded sample is the GaN thin film also presented in the previous figure [N_2^+ , $E_{kin} = (81 \pm 16) \text{ eV}$, $j = (2.60 \pm 0.07) \mu\text{A cm}^{-2}$, $R_{I/A}=1.0$]. (a) HRTEM image of a crystalline GaN mound. (b) electron diffraction pattern recorded in the TEM. (c) – (e) FFT images obtained in three different positions as indicated in (a). The blue lines in (c) and (e) represent an angle of 58.2° .

In Fig. 5.23 (c) the $(\bar{1}100)$ reflections are at an angle of $(58.2 \pm 0.1)^\circ$ to the horizontal as indicated by the blue line. The same blue line is depicted in Fig. 5.23 (e). Here, however it is visible that the $(\bar{1}100)$ reflections are not arranged parallel to the blue line, but they are tilted with respect to it. The angle of the reflections to the horizontal is determined to be $(60.4 \pm 0.2)^\circ$. Within one crystalline GaN mound structure this example shows a crystallite tilt of $(2.2 \pm 0.2)^\circ$. This value lies within the tilt distribution that was determined in subsection 5.2.2, where the XRD rocking curve FWHM for this curve was shown to be $(2.53 \pm 0.01)^\circ$. The broad tilt distribution of GaN crystals can also be observed from the measured electron diffraction pattern depicted in Fig. 5.23 (b) (for comparison with the expected pattern see Fig. 5.9). There are two types of intensity maxima. The bright, round spots originate from the Al_2O_3 substrate. The remaining intensity maxima are elongated along a circle around the center of the diffraction pattern. The shape of the GaN diffraction spots clearly suggests a tilt of the GaN crystals around $w\text{-GaN}[0001]$.

5.2.4 Summary

It was shown that the deposition rate of crystalline GaN and the surface coverage of the Al_2O_3 substrate could be increased, when the Kaufman ion source is applied. Thereby, instead of well-separated single $w\text{-GaN}$ nanocrystals as with applying the hollow-anode source, thin films, which have homogeneous thicknesses, can be deposited. The homogeneous and well-defined film thickness is determined by XRR. If N_2^+ ions are employed, the film thickness increases for increasing ϕ_{Ga} , i.e. the growth is limited by ϕ_{Ga} . However, increasing ϕ_{Ga} , further implies reducing $R_{I/A}$ well below 1. This may lead to the deposition of Ga droplets. The maximum obtained film thickness in the frame of this work is 13 nm. If N^+ ions are employed and experiments are performed under the same conditions (including the same range of $R_{I/A}$), the film thickness does not significantly increase with increasing ϕ_{Ga} . In this case the maximum achieved film thickness is approx. 6 nm. However, if both ϕ_{N}^+ and ϕ_{Ga} are increased, the film thickness increases. This suggests that applying N^+ ions, the growth is limited by ϕ_{N}^+ . In any case, considering that $R_{I/A}$ is expected to be close to 1, the material fluxes and therefore the deposition rates are limited. Comparing the material fluxes with the obtained film thickness, it is found that the fraction of the atoms that are incorporated in the thin film is small (in some cases only 1/20). Apart from increasing the material fluxes, different measures, such as changing the substrate material or the substrate temperature, might consequently lead to an increased film thickness, too. When N_2^+ ions are employed, the surface topography reveals elongated structures, which indicate anisotropic lateral growth velocities due to the anisotropic lattice mismatch. In contrast, when N^+ ions are used, this effect is not observed, which might be due to a strong enhancement of the adatom mobility. The obtained GaN films are epitaxial, wurtzitic and $(11\bar{2}0)$ -oriented. Compared to μm -thick GaN films

in the literature, the crystal tilt distribution is very broad. However, relaxation mechanisms have already set in after a few nm of film thickness. The in-plane stress as well as the widths of the crystal tilt and twist distributions decrease with increasing film thickness. Cross-sectional HRTEM images reveal apart from the presence of crystallite tilt, the occurrence of a defect-rich, interface-near layer with a thickness of a few nm. This layer is caused by the large lattice mismatch along $\text{Al}_2\text{O}_3[11\bar{2}0]$. RHEED measurements reveal that the growth mode is still predominantly 3-dimensional, even though tendencies to 2-dimensional growth are recognizable. Therefore, it is clear that coalescence has to occur, if the high coverage determined by AFM and TEM is to be obtained. Correspondingly, TEM measurements combined with XRD rocking curve measurements suggest that low angle grain boundaries consisting of dislocations are the dominant crystal defects in the GaN films.

6. Conclusion and Outlook

This work aims at implementing an experimental setup for energy and mass selected IBAD and evaluating its feasibility using the model system GaN growth on $\text{Al}_2\text{O}_3(1\bar{1}02)$. Five requirements were formulated, which could be used to assess the performance of the implemented instrumentation. Those requirements refer to the spatial dimension of the instrumentation, the obtainable ion current, the selectability and resolution of the ion kinetic energy, the selectability and the resolution of the ion mass and the homogeneity of the ion beam. It is shown that the ion mass is selectable with the required precision. The measured behavior in terms of mass selection agrees with trajectory simulations as well as the general theory of quadrupole mass filtering. The kinetic energy is also shown to be selectable with adequate precision. However, the width of the energy distributions is slightly larger compared to values in literature. The obtainable ion currents are limited by either the coupling out of the RF potential as suggested by trajectory simulations or by space charge repulsion between ions on the way between quadrupole and sample as suggested by calculations with respect to the ion beam spread. Though, the maximum obtainable ion currents are appropriate in comparison to the instrumentation used by other groups. The homogeneity of the beam may vary depending on deposition parameters, e.g. the ion species. In most cases the width of the ion beam in the relevant position is on the order of 1 cm. In some cases defocusing the beam in order to increase the beam width might be necessary. Two different ion sources, a constricted-glow discharge plasma source and a Kaufman-type ion source, were tested in combination with the quadrupole mass filter system. The difference in the performance between the two ion sources is due to the ion extraction, which happens within the quadrupole entry electrodes in the first case and in a grid system implemented in the ion source in the second case. This has consequences on the distribution of kinetic energies as well as on the ion current density as measured in the sample position. Nevertheless, the requirements for energy and mass selected IBAD are fulfilled for both ion sources.

With these results the feasibility of energy and mass selected IBAD can only be assessed hypothetically. Since the reality of epitaxial thin film deposition is accompanied by an interplay of a multitude of processes, among which are sputtering, surface diffusion, reflection, adatom desorption, the formation of lattice defects and stress relief, in a second part of this work, epitaxial thin film deposition was carried out applying the quadrupole system. In order to simultaneously examine the variety of possibilities that this novel experimental setup offers, both well-separated, epitaxial w-GaN nanocrystals ('nanodots' or 'quantum dots') and predominantly (though not completely) coalesced, epitaxial GaN thin films with defined, homogeneous film thicknesses are deposited.

The GaN nanocrystals have a lateral dimension of a few 10 nm and a vertical dimension of up to 10 nm. Their area density can reach values of up to $1.5 \cdot 10^{10} \text{ cm}^{-2}$ and their epitaxial relationship is as reported in literature for the growth on

$\text{Al}_2\text{O}_3(1\bar{1}02)$. The deposition of separated GaN nanocrystals is achieved using only N_2^+ ions as well as only N^+ ions. The isolated influence of the kinetic energy was regarded for the irradiation with N^+ ions. Thereby, differences became evident between the growth with kinetic energies close to the Brice window of ion-enhanced epitaxy ($E_{kin} = 60$ eV) and well above the Brice window ($E_{kin} = 120$ eV). The largest yield could be obtained for $E_{kin} = 60$ eV and for $R_{I/A} = 1.0$. For the larger energies, substrate damage as well as sputtering is assumed to be induced by the ion irradiation counteracting a larger yield of epitaxially grown GaN. Furthermore, the optimal value for $R_{I/A}$ shifts to larger values when E_{kin} is increased, which suggests a reduction of the N atom concentration on the surface due to ion implantation in volumes below the first monolayer.

The GaN thin films are also successfully deposited by using both only N^+ and only N_2^+ ions. If N_2^+ ions are used, the growth is limited by ϕ_{Ga} . The maximum obtained film thickness in this case is $d = 13$ nm. N^+ ions carry half as much atoms for the same ion current. In fact, the obtained film thickness is half as much compared to the films, where the growth is assisted by N_2^+ ion irradiation. The growth of GaN, which is assisted by N^+ ion irradiation, is found to be limited by ϕ_N^+ . In some cases the surface topography of the GaN films is anisotropic. Such anisotropies were observed before by other groups for non-polar GaN thin films on $\text{Al}_2\text{O}_3(1\bar{1}02)$, especially if the growth mode is 3-dimensional and the film not fully coalesced. The reason for the lateral growth velocities varying with the crystal direction is assumed to be the anisotropic lattice mismatch. It is to be noted that the surface anisotropies were not observed if N^+ ions were employed. Experiments in this context were performed with $E_{kin} = 60$ eV. The reason for this observation might be that significantly enhanced surface diffusion of adatoms due to N^+ irradiation governs the lateral growth, whereas the role of enhanced surface diffusion is less dominant for N_2^+ ions such that the anisotropic lattice mismatch becomes relevant for the lateral growth velocities. The epitaxial relationship of the GaN thin films is the same as for the nanocrystals. The distribution of crystallite twist and especially crystallite tilt are broad compared to literature values. However, the width of both crystallite tilt distribution and crystallite twist distribution and the in-plane lattice strain decrease with increasing film thickness. This indicates a relaxation of the crystal lattice with increasing film thickness. The defect structure is dominated by low angle grain boundaries, which consist of dislocations and are created during coalescence of slightly tilted GaN crystallites. Their presence is indicated by the observation of inclined line defects in TEM measurements in combination with the observed broad crystallite tilt distribution. The frequently reported occurrence of basal stacking faults accompanied by prismatic stacking faults and partial dislocations for coalesced, non-polar GaN thin films might also be an explanation for the observed line defects.

The deposition experiments demonstrate that the quadrupole mass filter system in combination with different ion sources can successfully be applied to perform energy

and mass selected IBAD. It was shown that both nanocrystals and thin films could be grown assisted by different ion species (N^+ and N_2^+) with different kinetic energies ($60 \text{ eV} \leq E_{kin} \leq 120 \text{ eV}$). Differences between the growth assisted by different kinetic energies but the same ion species (N^+) were found and assumed to be due to sputtering, ion implantation and crystal defect formation. Moreover, differences between the growth with the same kinetic energy ($E_{kin} = 60 \text{ eV}$), but different ion species were found. Due to dissociation of molecular ions and division of kinetic energy, the surface diffusion is assumed to be enhanced to a different extent by N^+ or by N_2^+ ions, which has consequences on the surface topography of the GaN thin films. These observations are consistent with the Brice model, however they are not to be understood as complete investigation of the influence of the ion kinetic energy or the ion species on the epitaxial growth. Nevertheless, since differences are hinted by the presented experiments, further approaching the isolated dependence of the ion species and the kinetic energy experimentally is motivated.

As in most previous works, in this work the ion-to-atom ratio $R_{I/A}$ was used as process parameter [Pop15, Fin15, Neu13]. It was shown that if in IBAD growth is assisted by N^+ ion or by N_2^+ ion irradiation keeping $R_{I/A} = \phi_N^+ / \phi_{Ga}$ constant, the results differ significantly. For future experiments, it may therefore be of interest to consider the 'atom-to-atom ratio' $R = \phi_N / \phi_{Ga}$ (being $2 \cdot R_{I/A}$ for N_2^+) instead as experimental parameter, for a better comparability of results obtained with different ion species. Further approaching the dependencies of ion species and ion kinetic energy implies the necessity to increase the deposition rate. For GaN growth, interesting effects like changes of the crystal phase may not be observable for film thicknesses $d < 15 \text{ nm}$ (see e.g. [Pop15a]). Moreover, it will be important to also deposit GaN thin films with significant thickness, where the growth is assisted by N^+ ion irradiation or by ion irradiation with $E_{kin} < 60 \text{ eV}$. As was elucidated in detail, increasing the ion current density imposes considerable challenges. Though, in principle the ion current density is sufficient for reasonable deposition rates such that it does not need to be increased necessarily. Therefore, efforts with respect to increasing the deposition rate must focus on increasing the number of incorporated atoms as fraction of the material fluxes. One possibility to do so could be the deposition temperature. In this work, most of the experiments were conducted at 650°C . It was shown e.g. in the subsection about the nanocrystals that for $T_s = 650^\circ\text{C}$, there is an upper limit for ϕ_{Ga} , since Ga droplet formation sets in and predominantly covers the surface. For the deposition of thin films using the Kaufman ion source, increasing the deposition temperature might enable a further increase of ϕ_{Ga} without a significant Ga droplet formation [Hey00]. This would be beneficial in terms of deposition rate, because it was shown that in some cases the growth was limited by ϕ_{Ga} . Another possibility to increase the deposition rate without increasing the material fluxes might be the choice of the substrate. Compared to Al_2O_3 , there are substrates with smaller lattice mismatches for GaN growth like 6H-SiC, where a faster GaN growth might be facilitated [Liu02]. Further, since a deteriorating effect of charge

building up locally on the Al_2O_3 cannot be ruled out completely, it might be beneficial to choose a substrate, which is not electrically insulating. Using a different substrate like 6H-SiC is interesting for another reason apart from increasing the deposition rate: In contrast to $\text{Al}_2\text{O}_3(1\bar{1}02)$, it was often observed that depending on parameters like $R_{I/A}$ or E_{kin} , the thermodynamically stable wurtzite and the metastable zincblende structure may occur in varying ratios on different substrates [Ger01,Shi06]. Using such a substrate the influence on the crystal phase can also be investigated.

References

- [Abr69] A. A. Abrahamson, *Phys. Rev.* **178**, 76 (1969).
- [Adl88] D. L. Adler and B. H. Cooper, *Rev. Sci. Instrum.* **59**, 137 (1988).
- [Aka90] H. Akazawa and Y. Murata, *J. Chem. Phys.* **92**, 5560 (1990).
- [And98] A. Anders and M. Kühn, *Rev. Sci. Instrum.* **69**, 1340 (1998).
- [And96] A. Anders, N. Newman, M. Rubin, M. Dickinson, E. Jones, P. Phatak and A. Grassmann, *Rev. Sci. Instrum.* **67**, 905 (1996).
- [Asc09] T. Aschenbrenner, C. Kruse, G. Kunert, S. Figge, K. Sebald, J. Kalden, T. Voss, J. Gutowski and D. Hommel, *Nanotechnology* **20**, 075604 (2009).
- [Atk14] P. Atkins and J. d. Paula, *Physical Chemistry 10th edition* (Oxford University Press, 2014).
- [Bal13] B. J. Baliga, *Semicond. Sci. Technol.* **28**, 074011 (2013).
- [Bin86] G. Binnig, C. F. Quate and C. Gerber, *Phys. Rev. Lett.* **56**, 930 (1986).
- [Bir06] M. Birkholz, *Thin Film Analysis by X-Ray Scattering* (Wiley-VCH, Weinheim, 2006).
- [Bod13] A. Bodin, R. Laloo, P. Abeilhou, L. Guiraud, S. Gauthier and D. Martrou, *Rev. Sc. Instrum.* **84**, 095104 (2013).
- [Bor05] M. Born and E. Wolf, *Principles of Optics: electromagnetic theory of propagation, interference and diffraction of light* (Cambridge University Press, 2005).
- [Bra99] W. Braun, *Applied RHEED: Reflection High-Energy Electron Diffraction During Crystal Growth* (Springer-Verlag, Berlin/Heidelberg, 1999).
- [Bri89] D. K. Brice, J. Y. Tsao and S. T. Picraux, *Nucl. Instrum. Meth. B* **44**, 68 (1989).
- [Bro06] J. S. Brown, G. Koblmüller, F. Wu, R. Averbeck, H. Riechert and J. S. Speck, *J. Appl. Phys.* **99**, 074902 (2006).
- [Bro04] I. G. Brown, *The physics and Technology of Ion Sources* (Wiley-VCH, Weinheim, 2004).
- [Bro92] R. Browning, *Auger Spectroscopy and Scanning Auger Microscopy, Surface Analysis Methods in Materials Science* (Eds: D. J. O'Connor, B. A. Sexton and R. St. C. Smart, Springer-Verlag, Berlin/Heidelberg, 1992).
- [Cer05] I. Cermak, *Rev. Sci. Instrum.* **76**, 063302 (2005).

References

- [Cha14] N. Chauvin, *Space Charge Effects*, (Ed.: R. Bailey), CERN Yellow Report CERN-2016-007, 2014.
- [Cha06] A. Chakraborty, K. C. Kim, F. Wu, J. S. Speck, S. P. DenBaars and U. K. Mishra, *Appl. Phys. Lett.* **89**, 041903 (2006).
- [Chi11] C. D. Child, *Phys. Rev. (Series I)* **32**, 492 (1911).
- [Cho90] W. Y. Choi, T. H. Kang and H. Kang, *Bull. Korean Chem. Soc.* **11**, 290 (1990).
- [Col86] J. S. Colligon, *Vacuum* **36**, 413 (1986).
- [Cra02] M. D. Craven, S. H. Lim, F. Wu, J. S. Speck and S. P. DenBaars, *Appl. Phys. Lett.* **81**, 469 (2002).
- [Cre16] C. D. Cress, S. W. Schmucker, A. L. Friedmann, P. Dev, J. C. Culbertson, J. W. Lyding and J. T. Robinson, *ACS Nano* **10**, 3714 (2016).
- [Cul01] B. D. Cullity and S. R. Stock, *Elements of x-ray diffraction third edition* (Prentice Hall Inc, Upper Saddle River, NJ, 2001).
- [Dah11] SIMION 8.1, D. A. Dahl, Idaho National Engineering Laboratory, *simion.com*, 2011.
- [Dau08] B. Daudin, *J. Phys.: Condens Matter* **20**, 473201 (2008).
- [Dav78] L. E. Davis, N. C. MacDonald, P. W. Palmberg, G. E. Riach and R. E. Weber, *Handbook of Auger Electron Spectroscopy: A Reference Book of Standard Data for Identification and Interpretation of Auger Electron Spectroscopy Data* (Physical Electronics Division Perkin-Elmer Corporation, Eden Prairie, Mn, 1978).
- [Daw90] P. H. Dawson, *Int. J. Mass. Spectrom.* **100**, 41 (1990).
- [Daw76] P. H. Dawson (ed.), *Quadrupole Mass Spectrometry and its applications* (Elsevier, Amsterdam, 1976).
- [Daw71] P. H. Dawson, *Int. J. Mass Spectrom. Ion Phys.* **6**, 33 (1971).
- [Deb09] R. K. Debnath, T. Stoica, A. Besmehn, K. Jeganathan, E. Sutter, R. Meijers, H. Lüth and R. Calarco, *J. Cryst. Growth* **311**, 3389 (2009).
- [Den07] Z. Den, I. Bald, E. Illenberger and M. A. Huels, *J. Chem. Phys.* **127**, 144715 (2007).
- [Eat10] P. Eaton and P. West, *Atomic Force Microscopy* (Oxford University Press, 2010).
- [Eck03] W. Eckstein and R. Preuss, *J. Nucl. Mater.* **320**, 209 (2003).

- [Eck85] W. Eckstein and J. P. Biersack, *Appl. Phys. A* **37**, 95 (1985).
- [Ege07] R. F. Egerton, *Physical Principles of Electron Microscopy: An Introduction to TEM, SEM, and AEM* (Springer Science and Business Media, LLC, New York, NY, 2007).
- [Ens92] W. Ensinger, *Rev. Sci. Instrum.* **63**, 5217 (1992).
- [Fin15] A. Finzel, thesis, Universität Leipzig, 2015.
- [Fre03] L. B. Freund and S. Suresh, *Thin Film Materials* (Cambridge University Press, 2003).
- [Fro56] D. C. Frost and C. A. McDowell, *Proc. R. Soc. Lond. A* **236**, 278 (1956).
- [Ger17] J. W. Gerlach, P. Schumacher, M. Mensing, S. Rauschenbach, I. Cermak and B. Rauschenbach, *Rev. Sc. Instrum.* **88**, 063306 (2017).
- [Ger07] J. W. Gerlach, A. Hofmann, T. Höche and B. Rauschenbach, *Nucl. Instrum. Meth. B* **257**, 315 (2007).
- [Ger07a] J. W. Gerlach, J. Mennig and B. Rauschenbach, *Appl. Phys. Lett.* **90**, 61919 (2007).
- [Ger01] J. W. Gerlach, S. Sienz, W. Attenberger and B. Rauschenbach, *Physica B* **308-310**, 81 (2001).
- [Ger00] J. W. Gerlach, thesis, Universität Augsburg, 2000.
- [Ger00a] J. W. Gerlach, R. Schwertberger, D. Schrupp, S. Sienz, W. Attenberger and B. Rauschenbach, *IPAP Conf. Ser.* **1**, 202 (2000).
- [Ger99] J. W. Gerlach, D. Schrupp, K. Volz, M. Zeitler, B. Rauschenbach and A. Anders, *Nucl. Instrum. Methods B* **148**, 406 (1999).
- [Ger92] D. Gerlich, *Advances in Chemical Physics Series, State Selected and State to State Ion – Molecule Reaction Dynamics, Part 1: Experiment, Vol. 82, Inhomogeneous RF fields: A versatile tool for the study of processes with slow ions* (Eds.: C. Y. Ng, M. Bear, John Wiley & Sons, New York, 1992).
- [Gon03] A. R. González-Elipe, F. Yubero and J. M. Sanz, *Low energy ion assisted film growth* (Imperial College Press, 2003).
- [Got14] G. Gottstein, *Materialwissenschaft und Werkstofftechnik: Physikalische Grundlagen* (Springer-Verlag, Berlin, Heidelberg, 2014).
- [Gra83] A. Gras-Marti and J. A. Valles-Abarca, *J. Appl. Phys.* **54**, 1071 (1983).

References

- [Gri01] V. Grill, J. Shen, C. Evans and R. G. Cooks, *Rev. Sci. Instrum.* **72**, 3149 (2001).
- [Gro74] R. Groh, G. Gerey, L. Bartha and J. I. Pankove, *Phys. Stat. Sol. A* **26**, 353 (1974).
- [Hab98] S. Habenicht, W. Bolse and K.-P. Lieb, *Rev. Sci. Instrum.* **69**, 2120 (1998).
- [Hau12] G. Haugstad, *Atomic Force Microscopy – Understanding Basic Modes and Advanced Applications* (John Wiley & Sons, Hoboken, New Jersey, 2012).
- [He06] L. He, Y. T. Moon, J. Xie, M. Muñoz, D. Johnstone and H. Morkoç, *Appl. Phys. Lett.* **88**, 071901 (2006).
- [Hem07] C. Hemmingsson, P.P Paskov, G. Pozina, M. Heuken, B. Schineller and B. Monemar, *J. Cryst. Growth* **300**, 32 (2007).
- [Het04] C. Hetherington, *Mater. Today* **7**, 50 (2004).
- [Hey00] B. Heying, R. Averbeck, L. F. Chen, E. Haus, H. Riechert and J. S. Speck, *J. Appl. Phys.* **88**, 1855 (2000).
- [Hir91] J. K. Hirvonen, *Mater. Sci. Rep.* **6**, 215 (1991).
- [Ina09] H. Inada, L. Wu, J. Wall, D. Su and Y. Zhu, *J. Electron Microsc.* **58**, 111 (2009).
- [Jac02] D. C. Jacobs, *Annu. Rev. Phys. Chem.* **53**, 379 (2002).
- [Joh16] G. E. Johnson, D. Gunaratne and J. Laskin, *Mass Spectrom. Rev.* **35**, 439 (2016).
- [Kad12] A. Kadir, K. Bellmann, T. Simoneit, M. Pristovsek and M. Kneissl, *Phys. Status Solidi A* **209**, 2487 (2012).
- [Kau90] H. R. Kaufman, *Rev. Sci. Instrum.* **61**, 230 (1990).
- [Kid10] M. Kidszun, R. Hühne, B. Holzapfel and L. Schultz, *Supercond. Sci. Technol.* **23**, 25010 (2010).
- [Kie31] H. Kiessig, *Ann. Phys.* **402**, 769 (1931).
- [Kik06] T. Kikuchi, A. S. Somintac, O. Ariyada, M. Wada and T. Ohachi, *J. Cryst. Growth* **292**, 221 (2006).
- [Kim95] B. C. Kim, J. R. Hahn and H. Kang, *Nucl. Instrum. Meth. B* **106**, 137 (1995).
- [Koc97] T. Koch and P. Ziemann, *Thin Solid Films* **303**, 122 (1997).

- [Kon12] B. H. Kong, Q. Sun, J. Han, I.-H. Lee and H. K. Cho, *Appl. Surf. Sci.* **258**, 2522 (2012).
- [Kud05] Y. Kudriavtsev, A. Villegas, A. Godines and R. Asomoza, *Appl. Surf. Sci.* **239**, 237 (2005).
- [Kyu09] R. N. Kyutt, M. P. Shcheglov, V. V. Ratnikov and A. E. Kalmykov, *Phys. Status Solidi A* **206**, 1757 (2009).
- [Lan13] I. Langmuir, *Phys. Rev.* **2**, 450 (1913).
- [Lea96] J. J. Leary and R. L. Schmidt, *J. Chem. Edu.* **73**, 1142 (1996).
- [Lee18] M. Lee, M. Yang, J.-S. Wi and S. Park, *Cryst. Eng. Comm.* **20**, 4036 (2018).
- [Li04] D. S. Li, H. Chen, H. B. Yu, X. H. Zheng, Q. Huang and J. M. Zhou, *J. Crystal Growth* **265**, 107 (2004).
- [Lif90] Y. Lifshitz, S. R. Kasi, J. W. Rabalais and W. Eckstein, *Phys. Rev. B* **41**, 10468 (1990).
- [Liu02] L. Liu and J. H. Edgar, *Mat. Sci. Eng. R* **37**, 61 (2002).
- [Lot15] A. Lotnyk, D. Poppitz, U. Ross, J. W. Gerlach, F. Frost, S. Bernütz, E. Thelander and B. Rauschenbach, *Microelectron. Reliab.* **55**, 2119 (2015).
- [Lot14] A. Lotnyk, D. Poppitz, J. W. Gerlach and B. Rauschenbach, *Appl. Phys. Lett.* **104**, 071908 (2014).
- [Ma99] Z. Q. Ma, Y. F. Zheng and B. X. Liu, *Appl. Surf. Sci.* **137**, 184 (1990).
- [Ma98] Z. Q. Ma and B. X. Liu, *Chin. Phys. Lett.* **15**, 668 (1998).
- [Mab85] M. A. Mabud, M. J. Dekrey and R. G. Cooks, *Int. J. Mass Spectrom.* **67**, 285 (1985).
- [Mac14] J. Mach, T. Šamořil, M. Kolíbal, J. Zlámal, S. Voborný, M. Bartošík and T. Šikola, *Rev. Sci. Instrum.* **85**, 083302 (2014).
- [Mac11] J. Mach, T. Šamořil, S. Voborný, M. Kolíbal, J. Zlámal, J. Spousta, L. Dittrichová and T. Šikola, *Rev. Sci. Instrum.* **82**, 083302 (2011).
- [Mal88] G. P. Malafsky and N. Winograd, *Rev. Sci. Instrum.* **59**, 1294 (1988).
- [Mar10] P. M. Martin (ed.), *Handbook of Deposition Technologies for Films and Coatings: Science, Applications and Technology* (Elsevier Inc., Oxford, UK, 2010).
- [Mar03] I. V. Markov, *Crystal Growth for Beginners: Fundamentals of Nucleation, Crystal Growth and Epitaxy* (World Scientific Publishing Co. Pte. Ltd., Singapore, 2003).

References

- [Mar89] R. E. March and R. J. Hughes, *Chemical Analysis Vol. 102, Quadrupole Mass Spectrometry*, ed. J. D. Winefordner (John Wiley & Sons, New York, 1989).
- [May99] M. Mayer, A. Pelzmann, H. Y. Chung, M. Kamp and K. J. Ebeling, *J. Cryst. Growth* **201/202**, 318 (1999).
- [Men15] J. Meng, X. Liu, Z. Fu, X. Wang and L. Hao, *Appl. Surf. Sci.* **347**, 109 (2015).
- [Mey81] K. Meyer, I. K. Schuller and C. M. Falco, *J. Appl. Phys.* **52**, 5803 (1981).
- [Mil86] P. E. Miller and M. B. Denton, *J. Chem. Edu.* **63**, 617 (1986).
- [Miy05] T. Miyazaki, K. Takada, S. Adachi and K. Ohtsuka, *J. Appl. Phys.* **97**, 093516 (2005).
- [Mor09] M. A. Moram, C. F. Johnston, J. L. Hollander, M. J. Kappers and C. J. Humphreys, *J. Appl. Phys.* **105**, 113501 (2009).
- [Mor08] H. Morkoç, *Handbook of Nitride Semiconductors and Devices, Vol. 1: Materials Properties, Physics and Growth* (Wiley-VCH, Weinheim, 2008).
- [Mou95] J. F. Moulder, W. F. Stickle, P. E. Sobol and K. D. Bomben, *Handbook of X-ray Photoelectron Spectroscopy: A Reference Book of Standard Spectra for Identification and Interpretation of XPS Data* (Eds.: J. Chastain and R. C. King, ULVAC-PHI, Chigasaki, Japan and Physical Electronics USA, Inc., Chanhassen, MN, 1995).
- [Mue86] K.-H. Müller, *J. Appl. Phys.* **59**, 2803 (1986).
- [Nak96] S. Nakamura, M. Senoh, S. Nagahama, N. Iwasa, T. Yamada, T. Matsushita, Y. Sugimoto and H. Kiyoku, *Appl. Phys. Lett.* **69**, 4056 (1996).
- [Nak94] S. Nakamura, T. Mukai and M. Senoh, *Appl. Phys. Lett.* **64**, 1687 (1994).
- [Nak93] S. Nakamura, M. Senoh and T. Mukai, *Jpn. J. Appl. Phys.* **32**, L8 (1993).
- [Nak91] S. Nakamura, Y. Harada and M. Seno, *Appl. Phys. Lett.* **58**, 2021 (1991).
- [Nas96] M. Nastasi, J.W. Mayer and J. K. Hirvonen, *Ion-solid interactions: fundamentals and applications* (Cambridge University Press, 1996).
- [Neu13] L. Neumann, thesis, Universität Leipzig, 2013.
- [Neu12] L. Neumann, J. W. Gerlach and B. Rauschenbach, *Thin Solid Films* **520**, 3936 (2012).
- [Neu01] A. Neumaier, *Introduction to numerical analysis* (Cambridge University Press, 2001).

- [Ni06] X. Ni, Y. Fu, Y. T. Moon, N. Biyikli and H. Morkoç, *J. Cryst. Growth* **290**, 166 (2006).
- [Nie89] J. A. Nieminen and K. Kaski, *Phys. Rev. A* **40**, 2088 (1989).
- [Nor03] J. Nord, K. Nordlund, J. Keinonen and K. Albe, *Nucl. Instrum. Meth. Phys. B* **202**, 93 (2003).
- [Oeh14] F. Oehler, D. Sutherland, T. Zhu, R. Emery, T. J. Badcock, M. J. Kappers, C. J. Humphreys, P. Dawson, R. A. Oliver, *J. Crystal Growth* **408**, 32 (2014).
- [Oco92] D. J. O'Connor, B. A. Sexton, R. S. C. Smart (Eds.), *Surface Analysis Methods in Materials Science* (Springer-Verlag, Berlin, Heidelberg, 1992).
- [Par92] K. H. Park, B. C. Kim and H. Kang, *J. Chem. Phys.* **97**, 2742 (1992).
- [Pas08] T. Paskova, *Phys. Status Solidi B* **245**, 1011 (2008).
- [Pau58] W. Paul, H. P. Reinhard and U. von Zahn, *Z. Phys.* **152**, 143 (1958).
- [Phe91] A. V. Phelps, *J. Phys. Chem. Ref. Data* **20**, 557 (1991).
- [Pok13] P. Pokorný, M. Novotný, J. Musil, P. Fitl, J. Bulíř and J. Lančok, *Plasma Process. Polym.* **10**, 593 (2013).
- [Pom02] J. M. Pomeroy, A. J. Couture, M. V. R. Murty, E. N. Butler and B. H. Cooper, *Rev. Sci. Instrum.* **73**, 3846 (2002).
- [Pop15] D. Poppitz, thesis, Universität Leipzig, 2015.
- [Pop15a] D. Poppitz, A. Lotnyk, J. W. Gerlach, J. Lenzner, M. Grundmann and B. Rauschenbach, *Micron* **73**, 1 (2015).
- [Qui95] J. Qian, D. C. Jacobs and D. J. Tannor, *J. Chem. Phys.* **103**, 10764 (1995).
- [Rap68] D. Rapp and T. Kassal, *Chem. Rev.* **69**, 61 (1969).
- [Rau17] B. Rauschenbach, A. Lotnyk, L. Neumann, D. Poppitz and J. W. Gerlach, *Materials* **10**, 690 (2017).
- [Rau06] S. Rauschenbach, F. L. Stadler, E. Lunedei, N. Malinowski, S. Koltsov, G. Costantini and K. Kern, *Small* **2**, 540 (2006).
- [Ray00] Rayflex Diffraction Software provided by Rich. Seifert & Co., which is now part of General Electric.
- [Rod06] C. Roder, S. Einfeldt, S. Figge, T. Paskova, D. Hommel, P. P. Paskov, B. Monemar, U. Behn, B. A. Haskell, P. T. Fini and S. Nakamura, *J. Appl. Phys.* **100**, 103511 (2006).

References

- [Rut03] P. Ruterana, M. Albrecht and J. Neugebauer (Eds.), *Nitride Semiconductors: Handbook on Materials and Devices* (Wiley-VCH, Weinheim, 2003).
- [Sch11] T. Schupp, T. Meisch, B. Neuschl, M. Feneberg, K. Thonke, K. Lischka and D. J. As, *Phys. Status Solidi C* **8**, 1495 (2011).
- [Sch99] R. Schwertberger, diploma thesis, Universität Augsburg, 1999.
- [Shi06] B. M. Shi, M. H. Xie, H. S. Wu, N. Wang and S. Y. Tong, *Appl. Phys. Lett.* **89**, 151921 (2006).
- [Sie04] S. Sienz, J. W. Gerlach, T. Höche, A. Sidorenko, T. G. Mayerhöfer, G. Benndorf and B. Rauschenbach, *J. Cryst. Growth* **264**, 184 (2004).
- [Smi90] F. A. Smidt, *Int. Mater. Rev.* **35**, 61 (1990).
- [Stu02] M. Stutzmann, G. Steinhoff, M. Eickhoff, O. Ambacher, C. E. Nebel, J. Schalwig, R. Neuberger and G. Müller, *Diam. Relat. Mater.* **11**, 886 (2002).
- [Sun09] Q. Sun, B. H. Kong, C. D. Yerino, T.-S. Ko, B. Leung, H. K. Cho and J. Han, *J. Appl. Phys.* **106**, 123519 (2009).
- [Sun08] Q. Sun, C. D. Yerino, T. S. Ko, Y. S. Cho, I.-H. Lee, J. Han and M. E. Coltrin, *J. Appl. Phys.* **104**, 093523 (2008).
- [Tak07] K. Takahashi, A. Yoshikawa and A. Sandhu (Eds.), *Wide Bandgap Semiconductors, Fundamental Properties and Modern Photonic and Electronic Devices* (Springer, Berlin, Heidelberg, 2007).
- [Tan07] F. Tang, T. Parker, G.-C. Wang and T.-M. Lu, *J. Phys. D: Appl. Phys.* **40**, R427 (2007).
- [Tun00] S. Tungasmita, J. Birch, P. O. Å. Persson, K. Järrendahl and L. Hultman, *Appl. Phys. Lett.* **76**, 170 (2000).
- [Uhr05] M. Uhrmacher and H. Hofsäss, *Nucl. Instrum. Meth. B* **240**, 48 (2005).
- [Vec90] D. Van Vechten, G. K. Hubler, E. P. Donovan and F. D. Correll, *J. Vac. Sci. Technol. A* **8**, 821 (1990).
- [Ven12] P. Vennéguès, J. M. Chauveau, Z. Bougrioua, T. Zhu, D. Martin and N. Grandjean, *J. Appl. Phys.* **112**, 113518 (2012).
- [Ven03] J. A. Venables, *Introduction to Surface and Thin Film Processes* (Cambridge University Press, 2003).
- [Ven73] J. A. Venables, *Pilos. Mag.* **26**, 697 (1973).

- [Vis06] V. M. Vishnyakov, V. I. Bachurin, K. F. Minnebaev, R. Valizadeh, D. G. Teer, J. S. Colligon, V. V. Vishnyakov and V. E. Yurasova, *Thin Solid Films* **497**, 189 (2006).
- [Vis97] R. D. Vispute, V. Talyansky, R. P. Sharma, S. Choopun, M. Downes and T. Venkatesan, *Appl. Phys. Lett.* **71**, 102 (1997).
- [Wal12] P. Waltereit, W. Bronner, R. Quay, M. Dammann, M. Cäsar, S. Müller, F. v. Raay, R. Kiefer, P. Brückner, J. Kühn, M. Musser, L. Kirste, C. Haupt, W. Pletschen, T. Lim, R. Aidam, M. Mikulla and O. Ambacher, *Phys. Status Solidi A* **209**, 491 (2012).
- [Wil15] P. Willke, J. A. Amani, A. Sinterhauf, S. Thakur, T. Kotzott, T. Druga, S. Weikert, K. Maiti, H. Hofsäss and M. Wenderoth, *Nano Lett.* **15**, 5110 (2015).
- [Wil09] D. B. Williams and C. B. Carter, *Transmission electron microscope: A textbook for materials science* (Springer Science and Business Media, LLC, New York, NY, 2009).
- [Win98] D. L. Windt, *Comput. Phys.* **12**, 360 (1998).
- [Wue59] R. F. Wuerker, H. Shelton and R. V. Langmuir, *J. Appl. Phys.* **30**, 342 (1959).
- [Xia09] H. Y. Xiao, F. Gao, X. T. Zu and W. J. Weber, *J. Appl. Phys.* **105**, 123527 (2009).
- [Yu14] I.-S. Yu, C.-P. Chang, C.-P. Yang, C.-T. Lin, Y.-R. Ma and C.-C. Chen, *Nanoscale Res. Lett.* **9**, 682 (2014).
- [Yas10] M. Yasaki, *The Rigaku Journal* **26**, V (2010).
- [Zeu96] M. Zeuner, J. Meichsner, H. Neumann, F. Scholze and F. Bigl, *J. Appl. Phys.* **80**, 611 (1996).
- [Zhe00] L. X. Zheng, M. H. Xie and S. Y. Tong, *Phys. Rev. B* **61**, 4890 (2000).
- [Zhu07] T. Zhu, D. Martin, R. Butté, J. Napierala and N. Grandjean, *J. Crystal Growth* **300**, 186 (2007).
- [Zie85] J. F. Ziegler, J. P. Biersack and U. Littmark, *The Stopping and Range of Ions in Solids* (Pergamon, New York, 1985).

Appendix

This appendix contains programming code. The code presented in A.1 and A.2 is written as workbench program for the program Simion in the language lua. A.3 contains code written in python. A.4 is a declaration of the author.

A.1 Simulation of stability diagram

```
1  simion.workbench_program()
2
3  array_ion={ }
4
5  adjustable _quad_axis_voltage = 30
6  adjustable frequency_hz = 3E6
7  adjustable _exit_pot = 20
8  adjustable _entry_pot = 40
9
10 local omega
11 local theta = 0
12 local count_ion = 0
13 local rfvolts = 245.25
14 local dcvolts = 196
15
16 function segment.flym()
17
18     sim_trajectory_image_control = 1
19     repeat
20     run()
21     until rfvolts > 1200
22
23 end
24
25 function segment.initialize_run()
26
27     for I = 1,1000 do
28         array_ion[i]=1
29     end
30
```

```
31     if ion_run <= 1 then
32         datei:write(count_ion, "\t")
33         print(dcvolts, rfvolts, count_ion)
34     end
35
36     count_ion = 0
37     dcvolts = dcvolts+4
38
39     if dcvolts > 200 then
40         rfvolts = rfvolts + 4.75
41         dcvolts = 0
42         datei:write("\n")
43         if rfvolts > 1200 then
44             datei:close()
45         end
46     end
47
48 end
49
50 function segment.fast_adjust()
51
52     omega = frequency_hz*(1E-6*2*3.14159)
53     local tempvolts = sin(ion_time_of_flight*omega + theta)*rfvolts +
54 dcvolts
55
56     adj_elect01 = _quad_axis_voltage + tempvolts
57     adj_elect02 = _quad_axis_voltage - tempvolts
58     adj_elect03 = tempvolts - dcvolts + _entry_pot
59     adj_elect04 = -tempvolts + dcvolts + _entry_pot
60     adj_elect05 = _entry_pot
61     adj_elect06 = -tempvolts + dcvolts + _exit_pot
62     adj_elect07 = tempvolts - dcvolts + _exit_pot
63     adj_elect08 = _exit_pot
64
65 end
66
67 function segment.other_actions()
68
69     if ion_pz_mm < 65 and array_ion[ion_number] == 1 then
```

```
70         count_ion = count_ion + 1
71         array_ion[ion_number] = 0
72     end
73
74 end
```

A.2 Determination of optimum voltages for exit electrodes in Simion

```
1  simion.workbench_program()
2
3  local test = 1
4  local best1 = 0
5  local best2 = 0
6  local best3 = 0
7  local best4 = 0
8  local voltage2
9  local voltage3
10 local voltage4
11
12 function segment.flym()
13
14     sim_trajectory_image_control = 1
15     repeat
16     run()
17     until ion_run > 10000
18
19 end
20
21 function segment.initialize_run()
22
23     if test > best1 then
24         best1 = test
25         best2 = voltage2
26         best3 = voltage3
27         best4 = voltage4
28     end
```



```
29
30     voltage2 = -200 + 400*rand()
31     voltage3 = -200 + 400*rand()
32     voltage4 = -200 + 400*rand()
33
34     print(ion_run/100, test, best1, best2, best3, best4)
35     test = 0
36
37 end
38
39 function segment.init_p_values()
40
41     adj_elect02 = voltage2
42     adj_elect03 = voltage3
43     adj_elect04 = voltage4
44
45 end
46
47 function segment.terminate()
48
49     if ion_pz_mm < 1 and ion_px_mm^2 + ion_py_mm^2 < 6.25 then
50         test = test+1
51     end
52
53 end
```

A.3 Determination of maximum ion current density as shown in Fig. 3.12 (b)

```
1  import math
2
3  q = 1.6e-19
4  epsilon0 = 8.85e-12
5  m_amu = 14
6  m_kg = m_amu*1.66e-27
7  i2 = 0
```

```
8
9 while i2 < 19:
10     Ekin_eV = 20 + 10*i2
11     Ekin_J = Ekin_eV*q
12     i = 0
13     j_opt = 0
14     r_opt = 0
15
16     while i < 1000:
17         I = 1e-7 + 1e-7*i    #currents in Ampere
18         K =
19 q*I*math.sqrt(m_kg)/(2**(5/2)*3.14159*epsilon0*Ekin_J**(3/2))
20         h = 0.001
21         z = 75    #travel distance of ion beam in millimeters
22         step_no = 0
23         r_0 = 8.75    #beam radii in millimeters
24         v = 0
25         r = r_0
26
27         while step_no < z/h:
28             v = v + h*K/r
29             r = r + h*v
30             step_no = step_no + 1
31
32         j = I/3.14159/r**2    #ion current densities in A*mm-2
33
34         if j > j_opt:
35             j_opt = j
36             r_opt = r
37
38         i = i+1
39
40     print(Ekin_eV, r_opt, j_opt)
41     i2 = i2 + 1
```

A.4 Selbstständigkeitserklärung

Hiermit versichere ich, dass die vorliegende Arbeit ohne unzulässige Hilfe und ohne Benutzung anderer als der angegebenen Hilfsmittel angefertigt und dass die aus fremden Quellen direkt oder indirekt übernommenen Gedanken in der Arbeit als solche kenntlich gemacht wurden.

Die Personen, von denen ich bei der Auswahl und Auswertung des Materials sowie bei der Herstellung des Manuskriptes Unterstützungsleistungen erhalten habe, wurden in der Danksagung aufgeführt.

Ich versichere außerdem, dass außer den genannten Personen niemand bei der geistigen Herstellung der vorliegenden Arbeit beteiligt war. Die Hilfe eines Promotionsberaters habe ich nicht in Anspruch genommen und niemand hat von mir oder in meinem Auftrag unmittelbar oder mittelbar geldwerte Leistungen für Arbeiten erhalten, die im Zusammenhang mit dem Inhalt der vorgelegten Dissertation stehen.

Ich versichere, dass die vorgelegte Arbeit oder Teile daraus weder im Inland noch im Ausland in gleicher oder in ähnlicher Form einer anderen Prüfungsbehörde zum Zwecke einer Promotion oder eines anderen Prüfungsverfahrens vorgelegt wurde.

Ich teile mit, dass keine früheren erfolglosen Promotionsversuche stattgefunden haben

Leipzig, 13.09.2018

Publications of the author

Peer-reviewed publications of the author

- 1) I. Hilmi, E. Thelander, P. Schumacher, J. W. Gerlach and B. Rauschenbach, *Epitaxial Ge₂Sb₂Te₅ films on Si(111) prepared by pulsed laser deposition*, Thin Solid Films **619**, 81 (2016).
- 2) P. Schumacher, S. G. Mayr and B. Rauschenbach, *Topography evolution of germanium thin films synthesized by pulsed laser deposition*, AIP Advances **7**, 045115 (2017)
- 3) I. Hilmi, A. Lotnyk, J. W. Gerlach, P. Schumacher and B. Rauschenbach, *Research Update: Van-der-Waals epitaxy of layered chalcogenide Sb₂Te₃ thin films grown by pulsed laser deposition*, APL Materials **5**, 050701 (2017).
- 4) J. W. Gerlach, P. Schumacher, M. Mensing, S. Rauschenbach, I. Cermak and B. Rauschenbach, *Ion mass and energy selective hyperthermal ion-beam assisted deposition setup*, Rev. Sci. Instrum. **88**, 063306 (2017).
- 5) I. Hilmi, A. Lotnyk, J. W. Gerlach, P. Schumacher and B. Rauschenbach, *Epitaxial formation of cubic and trigonal Ge-Sb-Te thin films with heterogeneous vacancy structure*, Materials and Design **115**, 138 (2017).
- 6) J. Lehnert, D. Spemann, S. Surjuse, M. Mensing, C. Grüner, P. With, P. Schumacher, A. Finzel, D. Hirsch and B. Rauschenbach, *Preparation and characterisation of carbon-free Cu(111) films on sapphire for graphene synthesis*, J. Phys.: Conf. Ser. **992**, 012024 (2018).
- 7) M. Behrens, A. Lotnyk, U. Roß, J. Griebel, P. Schumacher, J. W. Gerlach and B. Rauschenbach, *Impact of disorder on optical reflectivity contrast of epitaxial Ge₂Sb₂Te₅ thin films*, Cryst. Eng. Comm. **20**, 3688 (2018).
- 8) S. Liedtke, C. Grüner, A. Lotnyk, J. W. Gerlach, M. Mensing, P. Schumacher and B. Rauschenbach, *Crystallinity and texture of molybdenum thin films obliquely deposited at room temperature*, submitted to Crystal Growth & Design (2018).

Conference contributions of the author

- 1) P. Schumacher, J. W. Gerlach, S. Rauschenbach and B. Rauschenbach, *Implementation of a setup for ion energy and mass selective hyperthermal ion-beam assisted deposition of ultra-thin nitride films*, Poster presentation, 'DPG-Frühjahrstagung', Regensburg, 07.03.2016.

- 2) P. Schumacher, M. Mensing, J. W. Gerlach, S. Rauschenbach and B. Rauschenbach, *A custom quadrupole setup for ion energy and ion mass selective hyperthermal ion-beam assisted deposition of nitride nanofilms*, Talk, 'European Conference on Nanofilms', Bilbao, 20.10.2016.
- 3) P. Schumacher, M. Mensing, J. W. Gerlach, S. Rauschenbach and B. Rauschenbach, *Epitaxial nitride thin films by ion mass and ion energy selective ion-beam assisted deposition*, Talk, 'DPG-Frühjahrstagung', Dresden, 24.03.2017.
- 4) P. Schumacher, M. Mensing, J. W. Gerlach, S. Rauschenbach and B. Rauschenbach, *Ion-beam assisted deposition using ion mass and ion energy selective hyperthermal nitrogen ions*, Talk, 'International Conference on Surface Modification of Materials by Ion Beams' Lisbon, 13.07.2017.
- 5) P. Schumacher, M. Mensing, J. W. Gerlach, S. Rauschenbach and B. Rauschenbach, *Energy and mass selective ion beam assisted epitaxy for deposition of thin nitride films*, Talk, 'DPG-Frühjahrstagung', Berlin, 12.03.2018.

Curriculum Vitae of the author

Name: Philipp Schumacher
Date of birth: 15.08.1989
Place of birth: Münster (Westf.)
Nationality: German

School Education

1996 – 2000 *Mariengrundschule Münster-Hiltrup*
2000 – 2009 *Kardinal-von-Galen Gymnasium Münster-Hiltrup*

Community Service

07/2009 – 03/2010 *Arbeiter-Samariter-Bund Regionalverband Münster e.V.*

University Education

04/2010 – 03/2013 Student of Physics at *Universität zu Köln*
10/2012 – 03/2013 Bachelor Thesis: 'Polarisationseigenschaften von Photomischern in der Breitband-Terahertzspektroskopie' ('Properties of photomixers in broadband-terahertz spectroscopy with respect to polarization')
04/2013 – 03/2015 Student of Physics at *Universität Leipzig*
04/2014 – 03/2015 Master Thesis: 'Growth Morphology Evolution of Germanium Thin Films produced by Pulsed Laser Deposition' at *Leibniz-Institut für Oberflächenmodifizierung e.V.*
Since 04/2015 PhD student in Physics at *Leibniz-Institut für Oberflächenmodifizierung e.V.*

Danksagung

Als erstes möchte ich mich bei Prof. Dr. Dr. h.c. Bernd Rauschenbach bedanken. Er hat mir nicht nur die Möglichkeit gegeben an diesem Thema zu arbeiten, sondern auch viel Freiheit und Selbstständigkeit in der Vorgehensweise gelassen und selbstverständlich mit Ratschlägen und schneller Hilfe unterstützt, wenn es nötig war.

Auch Dr. Jürgen W. Gerlach gebührt ein ganz besonderer Dank. Mit seiner umfassenden Erfahrung in der Ionenstrahl-gestützten Abscheidung von GaN Schichten, in der Dünnschichtanalyse und in vielen anderen Themen war er immer eine große Hilfe. Zudem hat Herr Dr. Gerlach eine entscheidende Rolle in der Planung des Projektes "Energie und Massen-selektive Abscheidung" gespielt und damit wäre ohne seine Vorbereitung diese Arbeit nicht möglich gewesen. Außerdem möchte ich betonen, dass Herr Dr. Gerlach als Gruppenleiter stets eine offene Tür hatte und sich auch immer die Zeit genommen hat Ergebnisse, die nächsten Schritte oder sonstige Angelegenheiten zu besprechen. Dabei hat er immer einen ermutigenden Optimismus vermitteln können.

Als drittes Mitglied unserer Arbeitsgruppe "Energie und Massen-selektive Abscheidung" bedanke ich mich bei Michael Mensing. Ich glaube, dass es nicht selbstverständlich ist, dass man über eine vergleichsweise lange Zeit so kooperativ und kollegial im selben Labor arbeiten kann und gleichzeitig noch Spaß dabei hat. Außerdem hat er mit zahlreichen Ideen, tatkräftiger Unterstützung im Labor, vielen Röntgenbeugungsmessungen und auch mit Aufmunterungen zu dieser Arbeit beigetragen.

Prof. Dr. Stefan Rauschenbach danke ich für seinen Beitrag für die Planung des Quadrupolmassenfilters, dafür, dass er uns Software zur Ansteuerung des Quadrupols zur Verfügung gestellt hat, wodurch ich viel Zeit gespart habe, für seine Einschätzungen, Hilfe und auch für seine Gastfreundschaft.

Von der TEM-Arbeitsgruppe bedanke ich mich bei Dr. Andriy Lotnyk und bei Sören Herath für die Erstellung der TEM-Messungen. Zur Erzeugung von TEM-Messungen gehört auch das aufwendige Erstellen der TEM-Lamellen. In dem Zusammenhang bedanke ich mich bei Agnes Mill.

Vielen Dank auch an Dr. Ivo Cermak für die Konstruktion des Quadrupols.

Erstens für das Bereitstellen der Hohlanodenquelle und zweitens für die Arbeit, die für den Erhalt der guten Arbeitsbedingungen und die Führung des IOMs notwendig ist, vielen Dank an Prof. Dr. André Anders.

Inbesondere für die Hilfe bei der Wartung der Kaufman Ionenquelle, aber auch für die tatkräftige Hilfe, wenn es Probleme mit den Vakuumpumpen oder den Druckmesszellen gab, bedanke ich mich bei Thomas Pröhl.

Bezüglich der RBS Messungen, die für die Kalibrierung der Ga-Effusionszelle notwendig waren, bedanke ich mich bei Prof. Dr. Jan Meijer dafür, dass er den Beschleuniger LIPSION am Felix-Bloch-Institut für Festkörperphysik der Universität Leipzig zur Verfügung gestellt hat und bei Dr. Daniel Spemann dafür, dass er die Messungen durchgeführt hat.

Dietmar Hirsch gebührt Dank für einige durchgeführte XPS Messungen.

Eine nicht unwesentliche Rolle unter anderem bei der Inbetriebnahme des Quadrupols hat auch das Team der Werkstatt des IOMs gespielt. Deswegen bedanke ich mich bei Stefan Daum, Florian Hager, Ann-Grit Birnbaum und Birgit Voigt.

Christoph Grüner war immer bereit mit gelegentlich notwendigem Labormaterial auszuhelfen und hat bei dem Zusammenbauen von Strommessgeräten oder Analog-Digital-Schnittstellen unterstützt. Vielen Dank.

Für eine sehr gute Atmosphäre im Büro bedanke ich mich bei Uta Kapprell und bei Andriy Kulyk. Hervorheben möchte ich in dem Zusammenhang Isom Hilmi. Ich bedanke mich bei ihm für das freundschaftliche Miteinander über etwa 4 Jahre, das ermutigend war und auch fachlich in gegenseitigem Nutzen.

Für ihren Beitrag zu einem freundlichen und kollegialen Umfeld am IOM, bei dem man stets gerne zur Arbeit fährt und gegenseitige Hilfe selbstverständlich ist, bedanke ich mich bei allen Mitarbeitern am IOM; insbesondere aber bei Jan Lehnert und Mario Behrens.

Zum Schluss möchte ich mich bei meiner Familie, bei Ansgar, Simone und Benedikt Schumacher, für ihre Unterstützung bedanken.